MICROSTRUCTURE AND PROPERTIES OF PULVERISED FUEL SLAGS

by

STEPHEN JOHN GROVES

September 1986

A thesis submitted for the degree of Doctor of Philosophy of the University of London, and for the Diploma of Membership of the Imperial College

Department of Metallurgy and Materials Science
Imperial College of Science and Technology
London

CONTENTS

Page

Page

LIST OF TABLES

Page

LIST OF FIGURES

Page

LIST OF PLATES

ABSTRACT

A detailed microstructural study has been carried out on a wide variety of boiler deposits, taken from six coal-firing utilities. The deposits have been shown to have a wide range of compositions and microstructural features, reflecting both the position within the boiler and the mechanism of formation.

Deposits with chemical compositions close to the parent coal ash have been shown to be the product of the decomposition, sintering and recrystallisation of the whole fly-ash. The role of major microstructural factors - composition of slag, porosity, crystallinity - in determining the thermal shock characteristics of a deposit has been assessed by determining the relevant physical and mechanical properties of glassy and crystalline materials modelled on typical coal slags. This study has shown that highly porous deposits of low crystallinity are those which are likely to be most easily removed by the action of sootblowers.

The design of the burners in p.f. boilers has been shown to be of great importance in reducing the formation of deposits in this region.

Deposits with high levels of iron oxide (up to 90wt% Fe_2O_3) have been shown to be the result of the preferential deposition of pyrrhotite derived from the thermal decomposition of discrete pyrite particles. The thermal decomposition and oxidation of pyrite and pyrrhotite has been investigated as a function of temperature and oxygen partial pressure. Drop-tube simulation has shown that under the conditions prevailing close to p.f. burners, pyrrhotite is molten and hence capable of adhering to burner surfaces. Subsequent adherence of viscous silicate-based ash material is controlled by the surface temperature of the deposit.

A microstructural comparison of laboratory-prepared deposits with field samples strongly supports this mechanism. The model has been further extended to account for the initial formation of slags on tube-walls operating under "non-slagging" conditions.

ACKNOWLEDGEMENTS

The author would like to thank all the members of the Nuffield Research Group for their friendship and support over the last three years. In particular, Dr. J. Williamson must be thanked for his advice and encouragement throughout.

Mr. J. Wright and Mr. A.J. Tipple must be thanked for their technical assistance, Miss J. Bowring for carefully typing the text of this thesis, and Mr. H. Hamilton for proof-reading the text. The author is also grateful for the contributions made to this project by those at Babcock Power Limited, especially Dr. A. Sanyal, Dr. W.R. Livingston, Mr. J. Smart and Mr. D.C. Hough.

In addition, the studentship provided by the Science and Engineering Research Council and the financial assistance of Babcock Power Limited are gratefully acknowledged.

CHAPTER 1

Introduction - The practice of p.f. combustion for steam generation

Steam generation by coal combustion is a major source of electrical power throughout the world. Coal is burned most efficiently in pulverised form, in boilers rating 500MW or more. Figure 1 shows a diagramatic representation of a modern p.f. boiler. Such a system operates as a continuous process. Its function is to pulverise the coal supplied, accomplish efficient combustion in the furnace, and absorb the heat produced to raise superheated steam[1].

Coal pulverising equipment grinds the coal by impact, attrition, compression or a combination of two or more of these. During the milling process the coal is also dried. Classification devices ensure that typically 70% of the particles transported to the burner will be less than 75μm in diameter.

A small proportion of the air required for combustion (15-20%) is used to transport the coal to the burner. This is known as primary air ($\sim 100^{o}C$). The remainder of the combustion air - secondary air at $\sim 250^{o}C$ - is introduced at the burner. Turbulence within the flow is created by mechanical or aerodynamic means, in order to mix the primary and secondary streams, and maintain stability of the flame.

Within the flame, the carbonaceous matrix of the coal is partially volatilised and then oxidised, to give gaseous products, and leaving an inorganic residue known as ash. The ash is a product of the thermal decomposition and interreaction of the mineral matter incorporated into the coal during the original sedimentation process, and subsequent geological movement.

FIGURE 1 – Schematic representation of a modern p.f. boiler

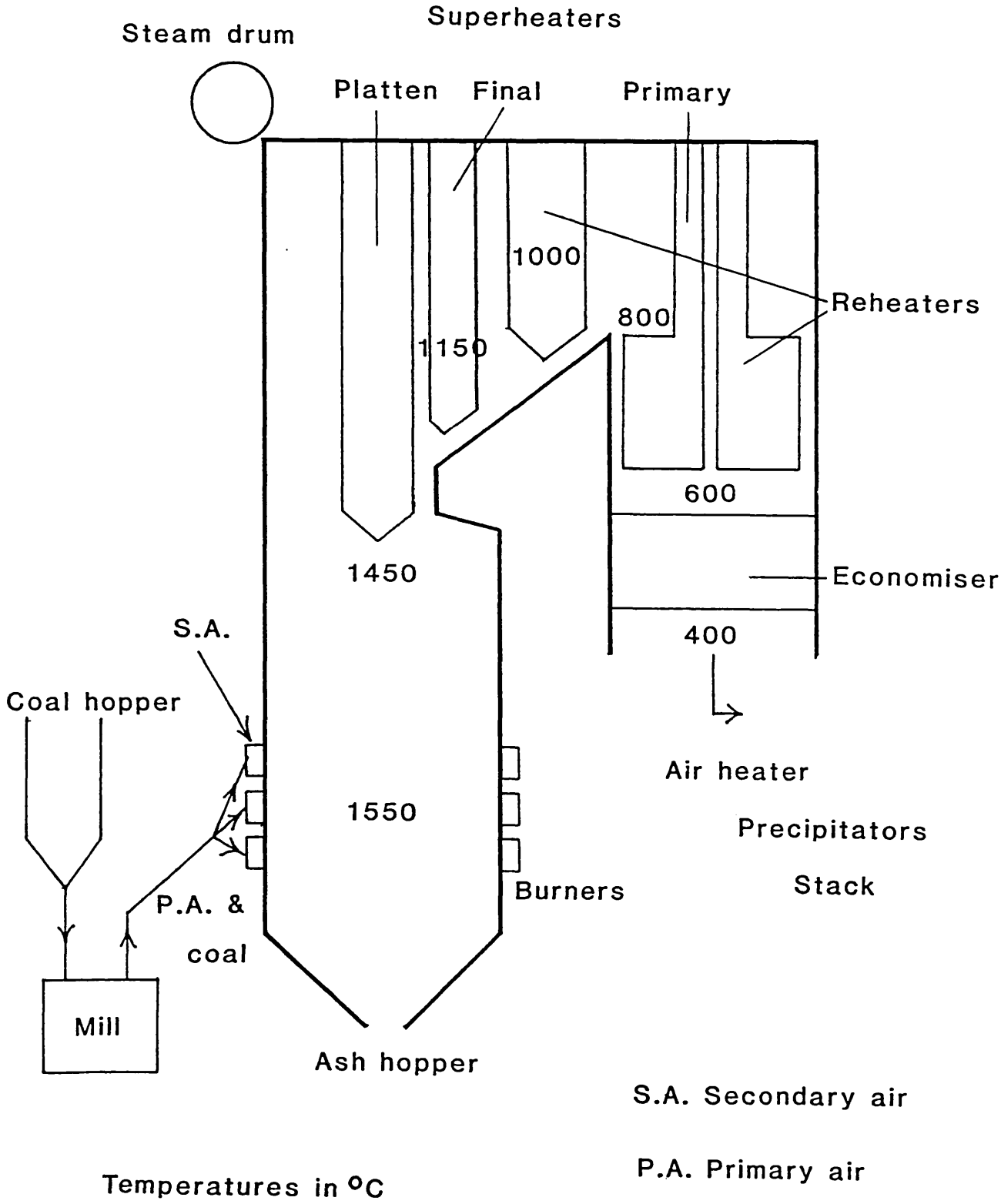

Heat from the combustion process is absorbed by radiation to the furnace walls and by convection and conduction to the cooler parts of the furnace. Combustion may raise the gas temperatures in the burner zone to $\sim 1550^{o}C$. Heat absorption lowers this to $\sim 400^{o}C$ at the economiser exit. Typical temperatures through the boiler are shown in Figure 1.

The water/steam path through a radiant, natural circulation boiler is complex. Feedwater enters through the economiser, and is piped to the steam drum at the top of the boiler. Downcomer pipes allow the water to flow naturally to the bottom of the boiler, and into the furnace tubes. Radiant heat absorption produces a steam/water mixture which is separated in the steam drum. Water is recycled to the bottom of the boiler, while steam is taken through the primary, platten and final superheaters, where it reaches a temperature of $\sim 570^{o}C$ at 165 bar, and hence to the turbine generators. Low pressure steam from the turbine is taken through the reheater banks, and then to the steam outlet.[2]

Together with the coal combustion characteristics, the coal ash is a major consideration in the design of a boiler.[3] A coal may contain as much as 40wt% ash - a typical British 500MW boiler burning 200 tonnes of coal per hour at full load may produce 30 tonnes of ash each hour.

Approximately 80% of the ash passes straight through the boiler, and is separated from the flue gases by banks of electrostatic precipitators, before the gases are released into the atmosphere.

The remaining 20% of the ash is deposited in the boiler, though only some of this will be retained on tube-walls, the rest falling into the bottom ash hopper. Deposition of solid matter within the radiant zone is known as slagging, and that in the convective zone as fouling. Slag deposits reduce the efficiency of the radiant absorption in the furnace, leading to increased gas temperatures further along the gas flow path, and hence problems in maintaining the correct water/steam cycle and increased fouling. In addition, large deposits can fall from walls, causing rupture of tubes on impact, and blockage of the ash hopper.

In extreme cases, pneumatic drills or explosive charges may be needed to clear slag during enforced boiler outage.

Control of deposition during operation of a boiler is of vital importance if efficiency and availability are to be maintained. Temperatures within the boiler may be controlled by the amount of excess combustion air used, and by the re-injection of cooled flue gases into the region above the burner zone (gas tempering). Gas temperatures must be maintained at levels at which ash will not adhere uncontrollably.

On-load removal of slag is achieved by sootblowers using either water, steam or air jets to induce fracture of deposits by thermal shock. The deposits are then dislodged from the wall under the combined action of their own weight, and the mechanical scouring of the jet. In the present study, the effect of slag composition, porosity and crystallinity on the physical and mechanical properties which determine thermal shock behaviour has been assessed. For this purpose, glassy and crystalline materials modelled on typical coal slags have been used.

Many techniques are available for the analysis of coal ash, and prediction of slagging behaviour. However, routine operational analysis of slag deposits is usually restricted to chemical composition determination. In the present study, a detailed microstructural examination has been carried out on a wide variety of deposits from six large utilities. Differences in composition and microstructure have been related to the position of deposit formation within the furnace, and hence to local temperature and atmosphere conditions.

These microstructural studies have shown the fundamental importance of the role of the iron-bearing mineral pyrite in the formation of iron-rich deposits and in the initiation of normal composition slags. The thermal decomposition and oxidation of the iron sulphides, pyrite and pyrrhotite, have been studied in detail. Throughout, particular attention has been paid to the way in which microstructural analysis of a slag can elucidate the mechanisms of formation of both normal and iron-rich deposits, and the role of boiler component design in these mechanisms.

CHAPTER 2

Literature Survey

2.1 Coal and coal minerals

Coal is the product of the action of moisture, heat and pressure on plant matter in the absence of air, over a period of millions of years.

Differences in the original plant matter and the extent of the initial decomposition determine the maceral content of the coal. The different maceral types - exinite, vitrinite and inertinite - have particular chemical and physical properties, and are recognisable petrographic units within the carbonaceous matrix.

The subsequent action of heat and pressure determine the coal's maturity, or rank. A young low-rank coal is termed a lignite; an old, high-rank coal an anthracite. A spectrum of coals exists between these two extremes. As the degree of coalification increases, the carbon content increases, with consequent decreases in oxygen and hydrogen contents.(4) The chemical and physical properties of the carbonaceous material in the coal are, in many respects, the most important considerations in boiler design.(5)

There are several sources of inorganic mineral matter in coal. Inherent mineral matter is that which generally arises from plant matter within the original coal swamp, and is hence intimately associated with the organic fraction. Adventitious mineral matter becomes associated with the coal during plant accumulation and subsequent geological processes.(6)

Coal mineralogy has been widely studied. Identification of minerals in bulk coal samples can be achieved using various optical and electron microscope techniques.(7) For further analytical purposes, it is desirable to separate the minerals from the carbonaceous material. Standard techniques for ashing involve roasting the coal in air at temperatures

up to 800°C.[8] The resulting ash is useful for chemical composition determination, for example by wet chemical methods or X-ray fluorescence, but is fundamentally different in mineral content when compared to the original coal ash.[9] This is due to decomposition and reaction during ashing. In order to separate the minerals in an almost totally unaltered state, a low temperature (~150°C) ashing process can be employed. In this procedure, a stream of oxygen is passed through an electromagnetic field produced by a radio-frequency generator. The oxygen plasma produced reacts with the carbonaceous matter of the coal, leaving a residue of virtually unaltered minerals.[10]

Mineralogical analysis can then take many forms. The two most commonly used techniques are X-ray diffraction analysis and infra-red absorption spectroscopy. These are powerful and versatile techniques, which can be used to identify the minerals present both qualitatively and quantitatively.[11] Theoretical mineral assemblages can be deduced from elemental analyses by normative analysis.[12]

Many mineral species have been reported as being associated with coals. The most frequently occurring types fall into four categories - clays, carbonates, sulphides and quartz.[12] Table 1 lists the commonly reported minerals in coal with their composition. Table 2 shows a number of quantitative mineralogical analyses of coals.[13]

Clays are the most frequently occurring inorganic constituents of coals. They are aluminosilicate layer minerals which can incorporate a wide range of cations, for example Ca^{2+}, Na^{+} and K^{+}. Kaolinite, micas and mixed-layer illite-montmorillonites are the most commonly reported.

The carbonate minerals in coal are generally calcite, dolomite, ankerite and siderite, although a wide range of composition may be shown, due to the extensive solid solution series which occur.

TABLE 1 - Commonly reported minerals in coal with typical compositions

Clays	
Kaolinite	$Al_8\ Si_8\ O_{20}\ (OH)_6$
Montmorillonite	$(Na,K)_x\ (Al_{4-x}\ Mg_x)\ Si_8\ O_{20}\ (OH)_4$
Mica	$(Na,K)_2\ Al_4\ (Si_6\ Al_2)\ O_{20}\ (OH)_4$
Carbonates	
Calcite	$CaCO_3$
Siderite	$FeCO_3$
Dolomite	$MgCO_3 . CaCO_3$
Ankerite	$Ca\ (Mg,\ Fe)\ (CO_3)_2$
Sulphides	
Pyrite	FeS_2 (cubic)
Marcasite	FeS_2
Sphalerite	ZnS
Galena	PbS
Quartz	SiO_2
Minor minerals	
Halite	NaCl
Gypsum	$CaSO_4.2H_2O$
Goethite	FeO.OH
Anatase	TiO_2 (tet.)
Magnetite	$Fe_3\ O_4$
Hematite	Fe_2O_3

TABLE 2 - Mineralogical analyses of six coal ashes determined by X-ray diffraction[13]

	Origin of coal					
	U.K.	U.K.	South Africa	South Africa	South Africa	Australia
Micas	31.6	32.5	4.1	4.9	9.0	11.9
Kaolinite	27.3	27.1	72.8	31.7	58.6	54.6
Quartz	29.3	17.6	10.2	1.2	<0.1	20.6
Dolomite	4.1	3.9	5.2	13.9	10.2	3.6
Calcite	1.8	2.1	4.9	47.1	15.0	4.7
Pyrite	5.8	16.8	2.9	1.2	7.2	4.7

Figures represent weight %, normalised to 100%.

Of the sulphide minerals, pyrite is by far the most common. However, marcasite, sphalerite and galena have been reported.

Quartz is almost always present in coal.[12]

2.2 The thermal behaviour of coal constituents

The objective of a steam-generating boiler is to absorb the latent heat of the carbonaceous matrix of the coal, primarily released through the reactions:

$$C(\text{graphite}) + \tfrac{1}{2}O_2\ (g) = CO(g) \qquad \Delta H = -106.4\text{kJ/mol}$$

$$CO(g) + \tfrac{1}{2}O_2\ (g) = CO_2(g) \qquad \Delta H = -286.1\text{kJ/mol}$$

while minimising losses from incomplete combustion and superfluous air. This requires temperatures high enough to ignite the coal, turbulence sufficient to mix the solid and gaseous reactants, and time sufficient for complete burn-out. Particles in a flame may be heated to temperatures greater than 1500°C, at rates of up to 1000°C/s.[1]

Such thermal conditions will fundamentally alter the nature of the coal mineral matter. The thermal behaviour of the individual minerals in coal has been extensively studied.[14]

Combined use of differential thermal analysis (D.T.A.) and thermo-gravi metric analysis (T.G.A.) can give detailed information concerning the decomposition of minerals. X-ray diffraction is a convenient technique for analysing the phases produced.[15]

In considering the decomposition of hydrated silicate minerals, it is convenient to classify them as either magnesium silicates, calcium silicates or aluminosilicates, rather than by any structural criterion. The former two categories tend to dehydroxylate at relatively high temperature and recrystallise almost immediately - for example, talc decomposes to give enstatite at 900°C.

However, the clay minerals found in coal are generally hydrated aluminosilicates. These minerals tend to form intermediates, which crystallise only after further heating.[16]

On heating kaolinite, there are endothermic changes at around 100°C and 550°C, corresponding to loss of absorbed water and structural water, respectively. The latter loss results in the formation of a poorly crystalline phase, metakaolin. Metakaolin transforms exothermically between 950°C and 1050°C, to give an aluminium-silicon spinel and amorphous silica. At still higher temperatures, mullite and cristobalite are formed, the process occurringmost rapidly at around 1300°C. Mullite is stable up to its melting point, 1810°C.[17]

Other hydrated aluminosilicate minerals found in coal are characterised by the incorporation of other cations in the structure. These shale minerals, therefore, show similar reactions to kaolinite, though the exact temperatures of reaction, sizes of D.T.A. peaks and the nature of the products depend very much on the individual mineral. Generally, the minerals are less refractory, due to the fluxing effect of the extra cations on the amorphous silicate phases produced, and are totally fluid at around 1400°C.[18]

Carbonate minerals generally decompose on heating to form the oxide, with the endothermic liberation of carbon dioxide. The temperature at which this reaction occurs will depend on the carbonate - for example, calcite shows an intense endotherm peaking around 900-950°C. If the oxide is stable, e.g. CaO, MgO, no further reaction occurs. However, if the oxide itself is reactive, e.g. FeO from siderite, the full sequence of reactions is more complex. The mixed carbonates also show complex behaviour, due to the number of different cations present, and hence the possibility of solid state reaction and recarbonation.[19]

The thermal behaviour of pyrite may be classified according to atmosphere conditions. In the absence of oxygen, it first forms pyrrhotite ($Fe_{1-x}S$) with loss of sulphur, and at higher temperature free iron. The non-stoichiometric nature of the sulphides, together with sulphur polymerisation, make these reactions difficult to investigate.
In the presence of air, the reactions are even more complex, since many oxides and sulphates may be formed, dependent on the oxygen potential of the atmosphere over the sample.[20,21]

The mineral quartz undergoes an $\alpha \rightarrow \beta$ phase transition at 573°C, but is generally inert up to its melting temperature, 1723°C. If the temperature is very high (> 1650°C), volatilisation of small amounts of silicon monoxide may occur, by the reduction of silica in the presence of carbon or hydrogen.[22]

Of the less common minerals found in coal, the alkali halide salts are perhaps the most important in terms of thermal decomposition. Reaction with hydrogen gives both free alkali metals, which are able to volatilise, and acidic halides.[23]. These products are of particular importance in boiler fouling and corrosion respectively.

2.3 The thermal behaviour of mineral mixtures

In considering the thermal behaviour of coal mineral matter, two approaches are of interest.

Mineral mixtures can be thermally analysed in much the same way as individual minerals. Direct heat-treatment of standard or low temperature ash can provide much information.

Such an approach, however, does not take into consideration the true thermal history of the ash produced by a p.f. flame: first, a sharp temperature rise to around 1500°C, followed by slower cooling as heat is absorbed by the boiler. The formation of fly-ash and the mechanisms involved are, therefore, of considerable importance.

2.3.1 Thermal behaviour of coal ash

Several studies have followed the changes which occur when coal ash is heated. Table 3 lists the crystalline phases commonly reported as being formed through mineral matter interaction at high temperature.

O'Gorman and Walker[24] heated selected U.S. ashes for 3 hours in air, in the temperature range 1100°C to 1400°C, and analysed the residues by X-ray diffraction. There was no evidence of solid state reaction below 1100°C. At 1100°C, quartz, hematite, mullite, corundum, anhydrite and anorthite were identified. At higher temperatures, anhydrite was not found, the amounts of quartz and hematite decreased, and the amounts of mullite and cristobalite increased. Interaction of the components was seen to proceed according to the system $CaO-Al_2O_3-SiO_2-Fe_2O_3$ with minor amounts of modifier addition.

Mitchell and Gluskoter[25] heated ten low temperature ash samples at intervals from 400°C to 1400°C for ½ hour periods in air. No trace of the shale minerals was found above 500°C. Metakaolin was present from 500°C to 800°C, above which mullite became a major ash component. Pyrite was oxidised to hematite above 500°C, with some transformation to magnetite above 1300°C. Bassanite, formed from the partial dehydration of gypsum during plasma ashing, persisted to 500°C. Anhydrite, formed from its decomposition, was stable to 900°C. Quartz was detected up to 1300°C. Reaction products such as anorthite, gehlenite and cristobalite were detected above 900°C.

Nankervis and Furlong[26] used the same technique to investigate lignite low temperature ash from 200-1200°C. High sodium ashes produced sodium nitrates and sulphates at low temperature, and sodium silicates at higher temperature. Quartz persisted to at least 1000°C. Magnetite was present above 800°C, gehlenite-akermanite above 900°C. Low sodium ashes gave bredigite at high temperatures.

TABLE 3 - Crystalline products commonly formed through mineral matter interaction at high temperature

Anorthite	$CaO \cdot Al_2O_3 \cdot 2SiO_2$
Mullite	$2SiO_2 \cdot 3Al_2O_3$
Gehlenite	$2CaO \cdot Al_2O_3 \cdot SiO_2$
Akermanite	$2CaO \cdot MgO \cdot 2SiO_2$
Wollastonite	$CaO \cdot SiO_2$
Cristobalite	SiO_2
Hematite	Fe_2O_3
Hercynite	$FeO \cdot Al_2O_3$
Magnetite	$FeO \cdot Fe_2O_3$
Fayalite	$2FeO \cdot SiO_2$
Anhydrite	$CaSO_4$

These studies clearly show that below ∿1000°C, changes will occur to mineral matter as predicted by thermal analysis. Solid state interactions occur only at higher temperatures, and tend to give the recrystallisation products predicted by the equilibrium phase diagrams of the major ash components. Such observations are of great importance, and will be examined further in the consideration of deposit formation and the prediction of slagging propensity.

2.3.2 Fly-ash formation

Ash particle formation is mainly a function of the final stages of coal particle burn-out. The initial heating of coal yields volatile hydrocarbons which are either present in the original carbonaceous matrix, or produced by pyrolysis. The residual char burns by heterogeneous oxidation of both internal and external surfaces. Burn-out of particles 100μm or so in diameter is controlled by chemical kinetics.[27] The morphology of the char is dependent on atmosphere: reducing conditions tend to give hollow cenospheres, while oxidising conditions yield porous vesicular chars.[28] As combustion proceeds the char develops a lacy structure which eventually disintegrates.

The microstructural analysis of fly-ash has shown that several distinct categories of particle are present. The ash consists of crystalline and glassy spheres (diameter 0.1-50μm), which may be sintered together; magnetite spheres (∿50μm); quartz particles (∿50μm); char particles (10-300μm); hollow cenospheres (100-200μm); and complex sphere-in-sphere plerospheres (100-200μm)[29]. Stinespring, Zulkoski and Mazza[30] used a bench-scale combustor with suction probes to investigate the mineral transformations in U.S. bituminous ashes, containing illite, kaolinite, pyrite and quartz, with minor amounts of calcite, feldspar and gypsum. At 1400°C in 3% excess oxygen, mullite, quartz, magnetite, lime and anhydrite were produced. The reactions were mainly thermodynamically controlled, though hematite : magnetite ratios increased with residence time.

In the flame, the mineral matter is subjected to very rapid heating rates, perhaps two orders of magnitude higher than those used in conventional thermal analysis techniques. Two consequences result : firstly, it is highly unlikely that the majority of mineral matter will decompose exactly as indicated by thermal analysis, and secondly, that further physical phenomena will come to influence fly-ash formation.[31]

The mineral matter transformations which occur in the flame will depend on the distribution of inorganics in the coal. Littlejohn[32] has shown that the process of coal grinding produces p.f. which may contain 40-70% of clean coal particles containing only inherent mineral matter, 20-40% of mixed containing both carbonaceous and mineral matter, and 10-40% of discrete mineral particles, chiefly quartz and pyrite.

Inherent mineral matter is likely to vaporise forming very small droplets, while the discrete mineral matter will decompose very much as predicted by thermal analysis, i.e. quartz remains chemically unchanged, while pyrite produces lower sulphides, oxides or sulphates according to atmosphere.

In the mixed particles, mineral inclusions will react as the combustion front approaches. Even though the heating time is small, Hubbard et al[33] have shown that the clays are completely transformed. Kaolinite is wholly destroyed without melting, to give mullite and cristobalite. Shales tend to form fused aluminosilicates which may recrystallise on cooling. The silicate minerals remain intact, but the carbonates tend to fragment extensively due to the high heating rate.[31] As the char recedes, the ash will coalesce to give either fused particles or sinter, dependent on the temperature.[34]

According to Raask,[35] iron-catalysed reaction at the silicate/carbon interface may result in the formation of iron carbide, which can diffuse into the silicate. Reaction with silica will produce carbon monoxide. The pressure of this gas may expand the silicate to form cenospheres with walls 2-5μm thick, which may account for 5wt% of the ash. The formation of plerospheres may occur if mineral matter is intimately dispersed in the coal. On injection into the flame, if particles can acquire a fused silicate envelope, the carbon residue will prevent coalescence of the entrapped ash. Formation of cenospheres and plerospheres is favoured by relatively low temperatures, and short residence times in the hot zone of the flame.

2.4 The formation of boiler deposits

The accumulation of ash on wall tubes and convective tube banks occurs by a variety of processes. Slagging in the radiant zone of the boiler involves the adherence of partially molten or softened ash, and the subsequent sintering and recrystallisation of the silicate-based material. Fouling in the convective zone occurs at somewhat lower temperature, and involves fly-ash bonded by alkalis which have condensed in the cooler boiler reaches, after volatilisation in the flame.[36]

2.4.1 Physical processes in slag deposit formation

In considering the nature and formation of slag deposits, it is convenient to assume that the fly-ash arriving at a tube-wall consists only of homogeneous, glassy spheres. Deposit build-up can then be treated as a combination of sintering and crystallisation.

The sintering of glassy spheres occurs by viscous flow, and according to Raask[37] can conveniently be described by an equation originally derived by Frenkel:

$$\text{Degree of sintering } \alpha \left[\frac{x}{r}\right]^2 = \frac{3\gamma t}{2\eta r}$$

where x = radius of neck formed between touching spheres.

r = radius of spheres

γ = surface tension

η = viscosity

and t = time

The surface tension of the silicates of interest does not vary much with composition or temperature - Raask considers a value of $0.3 Nm^{-1}$ to be reasonable. Thus, the two important variables are viscosity, which for silicate glasses is very sensitive to composition and temperature, and time.

Sintering of fly-ash has been studied by dilatometric methods, mainly in attempts to find a reliable method for predicting the temperature at which sintering of ash particles begins, and often in combination with electrical conductivity measurement.[38, 39] Results generally confirm the dependencies predicted by the Frenkel equation.

The kinetics of crystallisation of glasses has been widely studied. It is a two-stage process in which nucleation is followed by crystal growth.

Nucleation has been reviewed by Fine[40]. In general terms, when a glass crystallises there is a decrease in free energy due to the transformation of glass to crystal, but at the same time there is also an increase due to the formation of an interface. There is, therefore, a critical radius below which growth is unfavourable, as the increase in free energy due to the interface is dominant. 'Embryos' of less than critical radius disappear as quickly as they are formed. Only when random structure fluctuations give embryos of greater than critical radius do stable nuclei form. Growth then results in a free energy decrease, and so is a favourable process. Nucleation may take place in the bulk (homogeneous) or at a surface (heterogeneous).

Once a stable nucleus has been formed, crystal growth may occur. The theory of interface-controlled crystallisation is well-developed. Mechanistically, two types of growth are possible: lateral growth envisages movement of the whole interface in single molecular steps, while continuous growth allows for molecular attachment to any site.[41] The classical reaction-rate analysis of Turnbull and Cohen[42] leads to an equation of the form:

$$\text{Rate of growth} = a_o \nu \exp(-\Delta G'/RT).(1-\exp(\Delta G/RT))$$

$$= k \frac{\Delta T}{\eta}$$

where a_o = distance of the order of the interatomic distance

ν = thermal vibration frequency

ΔG = decrease in free energy on crystallisation

$\Delta G'$ = kinetic barrier

ΔT = undercooling

and η = viscosity

Figure 2 shows the form of this equation. Growth rates are easily measured experimentally - an extensive review of methods and results has been presented by Milne[43] for a range of glass-forming systems. Crystallisation of coal ashes has not been extensively investigated, as the compositions are not of commercial interest. However, Watt[44] found that crystallisation affects the viscosity of a molten slag, and hence its flow and sintering characteristics. Deguire and Risbud[45] found that glasses made from Illinois coal fly-ash could be recrystallised to a maximum of 23wt% by suitable heat-treatments. The phases crystallising were those predicted by the phase diagrams of the major ash oxide components.

FIGURE 2 – Theoretical growth rate curve for crystal growth in a pure melt [42]

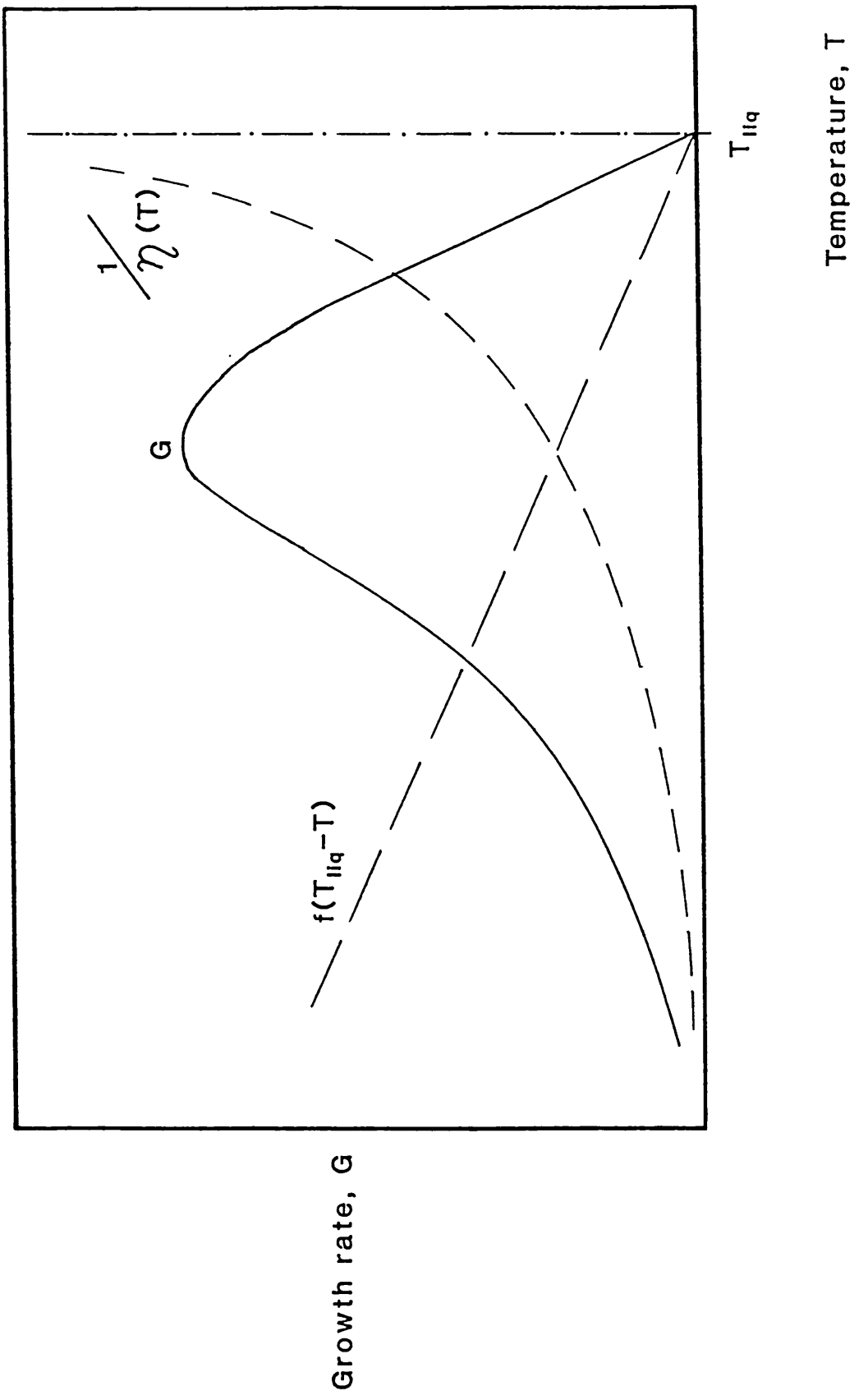

2.4.2 Examination of slag deposits

Until quite recently, little detailed study of slags had been reported. Boiler operators and designers worked only with the predictions of ash behaviour based empirically on elemental ash composition. Analysis of slags was not considered. Recently, however, a large amount of useful information concerning formation mechanisms has been obtained by microscopic examination of slags[46].

Hupa and Eriksson[47] identified several stages in slag formation, after microscopic and X-ray diffraction analysis of probe-collected samples. A thin initial deposit of hematite and anhydrite was noted, onto which glassy fly-ash particles had stuck and subsequently sintered. The authors considered that controlling the deposit surface temperature is the easiest way to reduce the extent of sintering of fly-ash, and prevent large, dense deposits forming.

Fessler et al[48] showed that although the overall composition of a deposit may be considered as constant, there will be local differences on a scale similar to the particle size of fly-ash - for example, pyritic residue and undissolved quartz. Livingston[49] has shown that the survival of such features is dependent on the temperature at which the slag is held, and the atmosphere present.

In a quantitative microstructural study, Jones et al[50] identified four distinct regions within a slag layer. As fly-ash is initially deposited onto a tube, it is quenched to a temperature (500-600°C) where crystal growth and sintering rates are effectively zero. The slag remains glassy and porous. As the deposit increases in thickness, the slag surface temperature increases as a result of the insulating effect of the deposit itself. So there is an intermediate region of increasing crystallinity and decreasing porosity. Still further towards the fire-side, there is a highly crystalline region, where porosity is at its lowest. The outer layer of the deposit consists of loosely sintered fly-ash, just beginning to be incorporated into the bulk. It was noted that

the morphology of the iron spinel produced during recrystallisation varied across the deposit, i.e. with temperature. Such observations are common in the study of magma crystallisation.[51]

Livingston et al[52] have used microstructural analysis to confirm the mechanism of the action of the additive copper oxychloride (C.O.C.) in reducing slagging. It was found that copper volatilised in the flame,[53] condensed on open slag surfaces and acted as a nucleating agent for iron spinels. Thus, in effect, pore surfaces were solid, and viscous flow sintering halted, or at least severely hindered. Slags formed were found to be more porous and friable.

2.4.3 Fouling deposit formation

Fouling is, by definition, a lower temperature process than slagging. Early microscopic work by Crossley[54] and Crumley et al[55] identified deposits as fly-ash particles bonded in an alkali-rich matrix.

In a detailed study, Rindt et al[56] identified three layers in fouling deposits. A thin inner layer very rich in sodium sulphate formed on the tubes initially. Inertial impaction of particles covered in sodium or calcium sulphate resulted in an inner-sintered layer on top of this. The outer-sintered layer formed the bulk of the deposits, consisting of complex sodium and calcium sulphates between crystalline silicate regions containing mainly melilite phases.

It is clear that sintering, especially when assisted by alkalis and eutectic mixtures, and crystallisation are important in fouling deposit formation, as well as in slagging. However, the enrichment of sodium and calcium indicates that volatilisation and subsequent condensation and sulphation of these elements is responsible for the initial adherence of fly-ash. In particular, the amount of sodium in a coal ash has been related to the likelihood of fouling - lignitic and other low-rank coals in particular give rise to this problem.[57]

2.5 Predictions of slagging behaviour

It is desirable from a commercial cost viewpoint to construct a boiler as small as possible. However, for a given calorific input, reducing size increases gas, and hence ash, temperatures. The boiler designer must, therefore, have detailed information about the likely slagging characteristics of the intended fuels. There are many techniques by which the so-called slagging propensity of an ash may be established.

2.5.1 Ash fusibility tests

The standard ash fusibility test[58] involves the optical examination of a pressed cone of ash, heated at constant rate in both oxidising and reducing conditions. The temperatures at which standard amounts of deformation are observed are taken as ash flow parameters - initial deformation temperature (I.D.T.), hemispherical temperature (HT) and flow temperature (FT) - which are extensively used by boiler designers. For example, the furnace exit gas temperature is usually designed to be above the I.D.T..

It has long been established that ash fusion characteristics can be related to the four component system of SiO_2, Al_2O_3, FeO and basic oxides.[59] Many studies have attempted to provide empirical relationships between ash fusibility and chemical composition, however with limited success.[60, 61, 62]

Ash fusion tests are widely used, but generally considered to be inadequate as a description of ash behaviour. Tests are largely subjective with large variations allowed between operators. In addition, the time-temperature history of the ash is unrealistic. The I.D.T. is not the temperature at which the first liquid appears: Huffmann and co-workers found that softening temperatures followed phase diagram liquidus curves, and that cones quenched from the I.D.T. contained evidence of substantial liquid formation.[63, 64]

Even with such shortcomings, the fusion tests will continue to be used within the power industry, until more accurate and reliable methods are available.

2.5.2 Viscosity-based indices

Slag viscosity is an important property since it governs flow, sintering and crystallisation behaviour. Viscosity indices take two forms - the base : acid ratio and its derivatives, and actual viscosity data.

2.5.2.1 Base : acid ratio

A qualitative indication of viscosity is given by the ratio of total base oxide content ($CaO + Fe_2O_3 + K_2O + Na_2O + MgO$) to the acid oxide content ($SiO_2 + Al_2O_3 + TiO_2$). This is founded on the principle that the first set of oxides are network modifiers and so act to decrease viscosity, while the second set are network formers. High values of base : acid indicate low viscosity.[65]

Table 4 shows the most commonly used slagging and fouling parameters. For bituminous ashes ($CaO + MgO < Fe_2O_3$) these parameters are based wholly on base : acid ratios, calculated from the oxides present in the ash. For lignitic ashes ($CaO + MgO > Fe_2O_3$) ash fusibility data is used.[66]

2.5.2.2 Viscosity indices

The viscosity-temperature relationship for ashes can be directly measured in a number of ways,[67] but such viscometry is complicated, costly and time-consuming. Much interest has, therefore, been shown in relating ash chemical composition to viscosity using empirical relationships. For example, Nicholls and Reid[68] and Watt and Fereday[69] have produced mathematical methods, valid for limited but well-defined compositional ranges, while Urbain et al[70] derived a more general formula

TABLE 4 - Slagging and fouling parameters[66]

Parameter	Method of Calculation	Applied limits
Bituminous ashes		
R_s	(Base : acid) x% sulphur	> 2.6 severe < 0.6 low
R_f	(Base : acid) x% Na_2O	> 1 severe < .2 low
R_f'	(Base : acid) x% water soluble Na_2O	> 0.7 severe < 0.1 low
Lignitic ashes		
R_s	$\frac{HT + 4IDT}{5}$	< 1150°C severe > 1340°C low
R_f	% Na_2O	> 6 severe < 2 low
Viscosity indices		
T_{250}	Temperature at 250 Poise	< 1200°C severe > 1275°C low
R_{vs}	$\frac{T_{250}\ (ox) - T_{10000}(red)}{97.5\ fs}$	≥ 2 severe < 0.5 low

(fs = factor dependent on $T_{2000}(ox) - T_{2000}$ (red)

N.B. s - slagging f - fouling

by considering fundamental aspects of bonding in aluminosilicate melts. Table 5 gives details of these three methods.

In order to compare coals, a simple viscosity index may be chosen, such as the temperature for a viscosity of 250 Poise, though the more complicated RVS has found widespread use (see Table 4).

Further parameters based on viscosity have been considered, in particular the temperature at which the onset of crystallisation affects flow. However, no suggested limits or values for the so-called T_V have been quoted in the literature.[44, 71] Sanyal et al[72] have incorporated the effects of crystallisation into the Watt-Fereday method.

2.5.3 Ash resistivity

The temperature at which a continuous liquid phase is formed in an ash compact can be indicated by electrical resistivity measurements. Cumming and Sanyal[73] have shown that in the solid state, ash resistivity is high, and varies according to the relationship:

$$\log(\text{resistivity}) \propto {}^{1}/_{\text{Temperature}}$$

At a critical temperature, T_R, the resistivity suddenly falls, the above relationship no longer holding. T_R is found to be invariably lower than the standard I.D.T. It is perhaps for this reason that T_R is unlikely to become accepted as a design parameter.

2.5.4 Sintering-strength-based indices

Sintering-strength tests measuring the force necessary to crush standard cylindrical pellets of sintered fly-ash, or laboratory ash, have been used to compare the fouling tendencies of coals.[74] Use of such tests is not common, but is of on-going research interest.[75]

TABLE 5 - Methods of calculating slag viscosity from chemical composition

i) Nicholls and Reid [68] -

$$\eta^{-0.1614} = (0.000814\ t + 0.01447) - B$$

where B = constant dependent on silica ratio

ii) Watt and Fereday [69] -

$$\log \eta = \frac{10^7\ M}{(t - 150)^2} + C$$

where $M = 0.00835\ SiO_2 + 0.00601\ Al_2O_3 - 0.109$

$$C = 0.0415\ SiO_2 + 0.0192\ Al_2O_3 - 0.0276\ Fe_2O_3 + 0.0160\ CaO - 3.92$$

$(SiO_2 + Al_2O_3 + Fe_2O_3 + CaO + MgO = 100\ wt\%)$

iii) Urbain et al [70]

$$\eta = AT\ \exp\ (10^3\ B/T)$$

with - $\ln A = 0.2693B + 11.6725$

where B = empirically determined constant.

η = viscosity in Poise

t = temperature in ^oC

T = temperature in K

2.5.5 Phase diagram predictions

For a limited data set, it is possible to correlate ash fusion properties to chemical composition by purely mathematical means. A more general approach is the use of 3-and 4-component phase diagrams.

Sanyal and Williamson[76] assessed the thermal behaviour of two lignitic ashes, which acted similarly in standard fusibility tests but very differently when fired. Hot stage microscopy[77] was used to show that the ashes crystallised to give very different products on cooling from the molten state. The ternary phase diagram $CaO-Al_2O_3-SiO_2$ was applied to the ash compositions normalised to these three components. The diagram showed that the non-slagging ash crystallised to give an increasingly viscous residual liquid phase, which would hinder sintering reactions. On the other hand, the highly slagging ash gave decreased liquid viscosity and would, therefore, be expected to give dense, troublesome deposits.

Kalmanovitch et al[78] have extended this concept, and found that the quaternary $CaO-Al_2O_3-SiO_2-FeO$ adequately describes ash crystallisation behaviour. Minor modifiers excluded by the normalisation process may in practise decrease the ash liquidus temperature from that predicted, but in general do not affect the crystallisation path. The method is now used by Babcock Power Limited in routine ash assessment.

2.6 The role of pyrite segregation in slagging

When considering the slagging propensity of a coal it is usual to treat the ash as a whole. The assumption that fly-ash may be considered as homogeneous is useful in elucidating the basic principles of slag formation, and the important variables involved.

Two particularly important aspects of ash performance require that a somewhat more rigorous approach be applied, specifically regarding the physical and chemical properties of pyrite.[21]

Firstly, tightening of environmental legislation has meant that the washing of coal must be considered as a primary method for removing pyrite from coal before it is fired. Separation depends on the fact that the specific gravity of pyrite (5.1) is much higher than that of the rest of the coal and mineral matter, and requires a detailed knowledge of the physical distribution of pyrite within the coal.

Secondly, several workers[79, 80] have reported the formation of iron-enriched deposits, containing up to 85wt% Fe_2O_3, from ashes containing normal iron oxide levels of 10-15wt%. Such enrichment must imply that mineral segregation occurs within the boiler.

2.6.1 Coal washing

The work of Littlejohn[32] has shown that most coals are likely to contain discrete pyrite particles after pulverisation. Borio and Narciso[80] carried out detailed analysis of the distribution of mineral matter by gravity separation of p.f.. The composition of the ash of each fraction was found to vary markedly with density. The high density fractions were enriched in pyrite, and it was suggested that the amount of iron in the heavier fractions might be used as a slagging index. It was also found that low density fractions were enriched in alkalis, and might similarly be used to indicate fouling potential .

Bryers and Taylor[81] used the combined effect of both size and gravity fractionation to study standard ash fusibility. Both highly basic and highly acidic fractions were found to be relatively refractory. Intermediate fractions containing 30-40% total base oxides produced very much lower softening temperatures, due to the fluxing effect of the base oxides on the acid oxides. Thus, coal washing may produce a fuel with a reduced ash content which is more likely to cause slagging problems than the original.

2.6.2 The formation of iron-rich deposits

Reactions of pyrite are dependent on both temperature and atmosphere. It is readily oxidised to hematite or magnetite, and may be reduced to pyrrhotite and further to iron. In a coal flame, the thermal history of a pyrite particle - temperature, residence time, atmosphere - will depend on the path through the flame. By studying the decomposition of pyrite particles in simulated boiler conditions, Halstead and Raask[82] have shown that significant amounts of sulphur may be retained in pyrite residues, even for those particles which have been through the hottest part of the flame.

The iron-sulphur phase diagram[83] indicates that the melting points of such particles will be low relative to even moderate flame temperatures. Borio and Narciso[80] conjectured that this meant that iron-rich spheres are likely to form as pyrite residues. The low aerodynamic drag coefficients of such particles would enable them to penetrate the main gas stream, and hence enrich wall deposits in iron.

Abbott and Austin[84] have studied the deposition of mineral matter from coal through the adhesion of fused ash to steel substrates. High density fraction ash, rich in pyrite, formed fusible and sticky drops. Synthetic mineral mixtures were also tested, and showed that the worst tendency for slag formation occurred with mixtures of pyrite and quartz or clay. In order to simulate actual boiler conditions more closely, the work was extended to coal combustion in drop-tube and down-fired furnaces[85]. Two types of ash particle were distinguished - iron-rich drops and aluminosilicate spheres. Under the experimental conditions, only the iron-rich drops gave significant adhesion to the metal substrates. Indiscriminate build-up of a deposit followed on top of this iron-rich initiator, leading eventually to a sintered outer layer, due to the rise in surface temperature caused by the insulating nature of the deposit.

2.7 Physical and mechanical properties of deposits

On-load removal of wall slag can be achieved by a rapid reduction of boiler load (thermal shedding). The temperature changes produced are sufficient to fracture deposits, but there are obvious economic drawbacks. Commonly, boiler design will incorporate 'sootblowers'. These are lances which penetrate the tube walls, and deliver a jet of either steam, water or compressed air onto the adjacent boiler surfaces. The thermal shock so applied fractures the slag, and the combined action of gravity and the scouring of the jet remove it from the wall. This action may typically be taken once a shift, i.e. every eight hours. If it is ineffective, continued build-up of deposits may require extended boiler outage for slag removal. It is clear, therefore, that the mechanical and physical properties of a deposit will be important in determining the effectiveness of sootblowing.

2.7.1 Thermal shock

Crack propagation in both glass and ceramic materials may occur on rapid changes of surface temperature. Since no stress-relieving mechanism is available, thermal gradients within a body will produce thermo-elastic stresses which may lead to surface flaw enlargement or catastrophic failure. The ability of a glass or ceramic body to withstand thermal shock may be expressed in terms of the pertinent physical properties of the body, and accompanying environmental factors.[86] Figure 3 shows the typical behaviour of glass on quenching in water, and the associated thermal stress parameters.[87] In order to account for the behaviour, two different theoretical approaches need to be considered.[88, 89]

FIGURE 3 - Thermal shock behaviour of a glass specimen

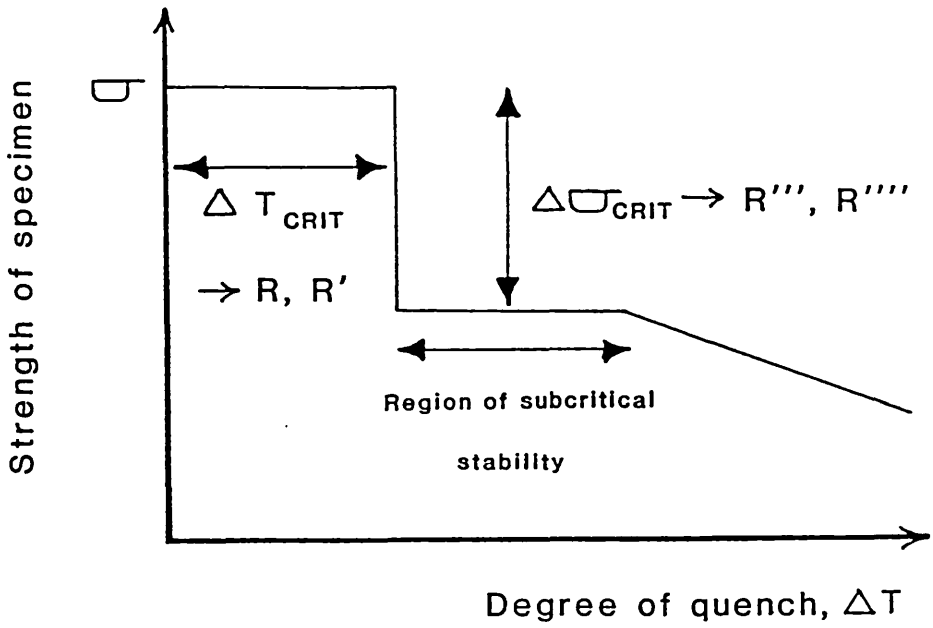

σ = "undamaged" fracture stress

E = Young's modulus

k = Thermal conductivity

α = Thermal expansivity

ν = Poisson's ratio

γ = Fracture surface energy

Thermal stress ranking parameters

$$R = \frac{\sigma(1-\nu)}{\alpha E}$$

$$R' = \frac{\sigma(1-\nu)k}{\alpha E}$$

$$R''' = \frac{E}{\sigma^2(1-\nu)}$$

$$R'''' = \frac{E\gamma}{\sigma^2(1-\nu)}$$

The severity of thermal shock that a material can withstand without incurring damage can be derived by assuming that damage occurs only when the maximum thermal stress reaches the fracture stress of the material. The parameters R and R' are taken as measures of material resistance to fracture initiation, and generally increase with increased thermal conductivity and fracture stress, but decrease with increased Poisson's ratio, Young's modulus and expansivity.(90)

The degree of damage can be estimated by considering the conditions for crack propagation. Any thermal shock provides a driving force for propagation in the form of stored elastic energy. The crack propagates until the stored elastic energy released equals the increase in surface energy on producing two new crack surfaces. The kinetic energy of the cracks continues propagation, until further surface is exposed to take up this energy. The crack is then sub-critical to the initial shock and an increase in shock severity is required to give further propagation. The body will retain a degree of strength.(91) The parameters R''' and R'''' are taken as measures of strength loss, and generally increase with increased Young's modulus and fracture surface energy, and decrease with increased fracture strength and Poisson's ratio.(90)

There have been no reported studies of the thermal shock behaviour of boiler slags.

2.7.2 Relevant physical and mechanical properties of materials

2.7.2.1 P.f. slags

Of the properties which determine thermal shock behaviour, only the thermal conductance of deposits has been studied in any detail. Such studies were undertaken to provide realistic values for designers to use in heat-balance equations, when assessing the effect of wall slagging on gas temperatures and thermal efficiency.

Boow, Goard and Mulcahy[92, 93] carried out extensive studies on the influence of ash physical characteristics on thermal conductivity. The conductance of deposits was found to depend on the degree of fusion, or sintering, and hence on temperature and composition - fused deposits had conductance values 3-4 times greater than unsintered ash. Particle size also affected conductance, large particles having higher conductance. These results have generally been confirmed by subsequent studies of other workers.[94, 95]

Study of the mechanical properties of slags has been restricted to sinter-strength measurements, designed primarily to indicate the temperature at which an ash may become troublesome.[74, 96] Strength is usually developed some 100-200^{o}C above the onset of sintering, and increases to a maximum ($\sim$700 MPa) before falling slightly at higher treatment temperatures.

All authors have emphasised the importance of atmosphere in determining sinter-related properties, due to the sensitivity of the ferrous : ferric ratio to oxygen partial pressure.

2.7.2.2 Glass and glass-ceramic materials

Although little work has been carried out on the properties of p.f. deposits, the study of commercially important silicate materials has been widely reported, and the general principles may be applied to boiler deposits. The three important variables in effecting microstructure - composition, porosity and crystallinity - can be mathematically related to the properties of a material.

The chemical composition of a glass will affect many of its structure sensitive properties in an additive way. In effect, the material is treated as a simple mixture of components, each of which contributes individually according to the amount present. This leads to equations of the type:

$$\text{Property} = C + \sum_{i} K_i \, (\% \text{ oxide})_i$$

where C and K_i are empirically or semi-empirically derived constants. Such equations may be accurate within ±1%.[97, 98, 99]

The effect of porosity on the properties of materials is profound. The basic principles are reviewed by Kingery et al.[100]

The mechanical strength of porous materials is experimentally found to decrease exponentially with porosity:

$$\sigma = \sigma_o \exp(-nP)$$

where n is in the range 4 - 7 and P is the volume fraction porosity.[101]

The elastic modulus of a composite can be given by analytically derived additive expressions, usually as upper and lower bounds. The simplest of these are derived by considering the composite as parallel layers of two materials. If the strain in each layer is the same,

$$E_{COMP} = V_1 E_1 + V_2 E_2 \qquad \text{Voight model, Upper bound}$$

and if the stress is the same,

$$\frac{1}{E_{COMP}} = \frac{V_2}{E_2} - \frac{V_1}{E_1} \qquad \text{Reuss model, Lower bound}$$

Considerable refinement is possible. For example, in the case of spherical closed porosity behaviour may be adequately represented by:

$$E = E_o\ (1 - 1.9P + 0.9P^2) \qquad (102)$$

Similarly, the thermal conductivity of composites may be treated in terms of 'slab' composites, in this case parallel and perpendicular to the thermal gradient:

$$K_{COMP} = V_1\ K_1 + V_2\ K_2 \qquad \text{Upper bound}$$

$$\frac{1}{K_{COMP}} = \frac{V_1}{K_1} + \frac{V_2}{K_2} \qquad \text{Lower bound}$$

Refinement may be provided by the Maxwell-Eucken model of dispersed spheres in a continuous matrix:

$$K_{COMP} = Kc \cdot \frac{1 + 2Vd\ (1-n/2n + 1)}{1 - Vd\ (1-n/n + 1)}$$

where,

Vd = Volume fraction of dispersed phase

Kc = Conductivity of continuous phase

Kd = Conductivity of dispersed phase

and n = Kc/Kd

The equation may be fitted to 'dispersed bad conductor' and 'dispersed good conductor', again giving two boundary limits.

A pore phase does not affect the thermal expansion of a material except in coarse-grained, highly porous materials of anisotropic expansivity, where constraint of one grain on the next may be reduced.

Glass-ceramic materials are very similar to p.f. slags in that their formation involves crystallisation of a glass, albeit in a controlled manner, giving crystals in a residual glass matrix. McMillan[103] has extensively reviewed the properties of these materials. The glass and crystalline phases generally have properties of the same magnitude, and effects are less pronounced than with porosity.

Mechanical strength is dependent on the amount of crystalline phase present, and the properties of that phase. Crystallites may act as crack inhibitors, causing deflection and blunting of a crack, and so increase the work of fracture. Alternatively, the combination of glass and crystallites of different thermal expansion may lead to micro-stress systems which reduce mechanical strength. The modulus of elasticity, expansion coefficient and thermal conductivity of polyphase materials are additive functions of the phases present, and are generally increased slightly by the inclusion of crystals in the glass matrix.[100, 104, 105]

Poisson's ratio relates transverse strain to longitudinal strain in tension or compression. For a perfectly isotropic elastic material its value is 0.25. The majority of glasses and ceramics have values lying between 0.20 and 0.25, with some exceptions, e.g. vitreous silica 0.16, and sintered silicon nitride 0.27. For slag-like materials, Poisson's ratio can be taken as 0.25, independent of microstructure.[89, 100]

CHAPTER 3

Experimental

3.1 Properties of glasses and partially crystalline materials

Synthetic glasses have been used to model the behaviour of slag materials, since laboratory control of microstructure can be easily achieved by suitable heat-treatment schedules. However, the techniques used to determine physical and mechanical properties have been chosen so as to be applicable to real slags.

3.1.1 Measurement of crystallisation rates

Even though crystallisation fundamentally affects the nature of a slag, little work has been reported concerning the rate at which crystals grow in glass of slag composition .

In this study, three ash compositions were chosen to represent a wide range of typical coals. Those compositions are shown in Table 6 and represent two lignitic ashes, differing only in iron oxide content, and one bituminous ash. In addition, further model compositions were chosen to examine the effect of small amounts of MgO, K_2O, Na_2O and FeO on crystallisation behaviour. The base compositions used were high and low lime content lignitic ashes, normalised to $SiO_2 + Al_2O_3 + CaO = 100wt\%$. These compositions are shown in Table 7.

For each composition, a similar method was followed. The glass was prepared by first mixing crushed quartz, and 'Analar' alumina and calcium carbonate in the appropriate proportions. Modifier additions were made as carbonates, oxides or oxalates, whichever proved most convenient. All the starting materials were thoroughly dried before the batch was weighed out. The mixture of starting materials, sufficient to yield 100g of glass, was then fused in a platinum crucible in a muffle furnace at 1500-1600°C. Melting was carried out in air, and continued for 24

TABLE 6 - Ash compositions used in crystallisation rate determinations

	Composition		
	1	2	3
	lignitic	lignitic	bituminous
SiO_2	46.95	43.37	54.50
Al_2O_3	29.19	29.19	26.40
CaO	12.64	12.64	1.50
Fe_2O_3	4.36	8.72	9.40
K_2O	1.09	1.09	4.20
Na_2O	0.65	0.65	1.20
MgO	3.49	3.49	1.60
TiO_2	1.63	1.63	1.10

N.B. Fe_2O_3 content of composition 2 is double that of composition 1, at the expense of SiO_2.

TABLE 7 - Model glass compositions used in crystallisation rate determinations

Glass	SiO_2	Al_2O_3	CaO	Fe_2O_3	K_2O	Na_2O	MgO
Low Lime - LL	49.00	31.50	19.50	-	-	-	-
LL/N	48.33	31.11	19.25	-	-	1.31	-
LL/K2	48.02	30.87	19.11	-	2.00	-	-
LL/M5	46.55	29.93	18.53	-	-	-	5.00
LL/F5	46.28	29.76	18.42	5.55	-	-	-
High Lime - HL	37.00	25.00	38.00	-	-	-	-
HL/N	36.54	24.65	37.51	-	-	1.31	-
HL/K2	36.26	24.50	37.24	-	2.00	-	-
HL/M5	35.15	23.75	36.10	-	-	-	5.00
HL/F5	34.95	23.61	35.89	5.55	-	-	-

hours. Iron-containing glasses were melted for 60 hours in order to establish ferrous : ferric equilibrium.[106] Homogeneity was ensured by quenching, crushing and remelting the glass twice during the melt period. After melting, the glass was cast onto a brass plate and annealed overnight from 750°C, to allow subsequent cutting into 5mm cubes using a circular diamond saw.

To follow crystallisation, three or more samples were held for varying times at selected temperatures ranging from 850°C to 1450°C. An optical microscope was used to examine polished sections from each sample. The iron-containing glasses were examined in reflected light, with polished sections etched in 1% HF/HCl to enhance the relief between the glass and crystalline phases. The remainder of the glasses were examined as thin sections in transmitted light.

Crystal growth was seen to occur mainly by surface nucleation, i.e. growth in an uninhibited manner. The crystal layer thickness on the outside of each section was measured using a calibrated eyepiece graticule. Thus, crystal layer thickness was found as a function of time for each temperature, the maximum slope of each growth curve being taken as a growth rate characteristic of that temperature.

From these results the maximum growth rate was plotted as a function of temperature for each glass. Peak growth rates were then compared, and the Urbain formula[70] used to establish the link between peak rate and viscosity, and hence chemical composition.

The crystalline phases present in each glass were determined by X-Ray Diffraction (X.R.D.) analysis using a Philips powder diffractometer with Cu (K_α) radiation.

In addition, several iron-containing glasses were examined by Electron Probe Micro-Analysis (E.P.M.A.) using a JEOL JSM-35 scanning electron microscope. In this technique, the secondary emission of X-rays from a polished surface bombarded by an electron beam is used to determine the chemical composition of that surface. The intensities of characteristic X-ray energies from the surface are compared to a set of elemental standards. A computer programme applies corrections for atomic weight (Z), absorption (A) and fluorescence (F), together known as ZAF corrections, in order to give the true chemical composition of the surface. The technique may be used to analyse large areas of the surface, or to analyse small 'spots', approximately 5μm in diameter and extending the same distance below the surface.

3.1.2 Measurement of thermal conductivity

Thermal conductivity was measured using a modified Lee's disc method. Figure 4 shows the experimental arrangement. A known current was passed through the heater disc until the thermocouples in each copper disc indicated that thermal equilibrium had been reached. The thermal conductivity of the sample was calculated by considering the steady state heat flow through the discs.[107] Sample temperature was typically 150°C at equilibrium.

The high and low lime base glass compositions (HL and LL) were used for this study. Dense glassy samples were prepared by grinding flat parallel surfaces onto a cast and annealed glass 'pool'. A diamond tool was then used to core a suitable section.

Crystalline materials were prepared by heating glassy samples at 1100°C. Heat-treatment was carried out with the samples held in alumina cement moulds, so that they retained the correct shape for conductivity determination with a minimum of grinding.

FIGURE 4 – The determination of thermal conductivity

h = Rate of heat loss per unit area

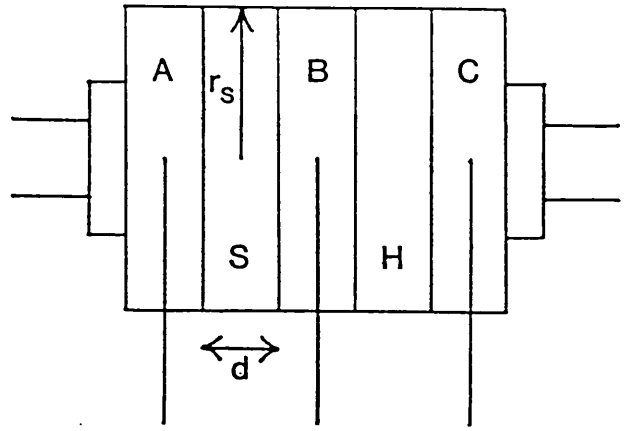

Thermocouples T_A T_B T_C

A, B, C	Copper discs
H	Heater disc (Voltage V, Current I)
S	Sample

a_i = Exposed area of disc

Assume linear thermal gradients

a) For steady state,

Heat input = Heat losses

$$VI = h \sum a_i T_i \longrightarrow \text{Value of } h$$

b) For sample disc in steady state,

(Mean of input and output) – Loss through surface = 0

$$\tfrac{1}{2} h \left[a_S (T_A + T_B)/2 + 2a_A T_A \right] - k \pi r_S^2 (T_B - T_A)/2 = 0$$

Hence k can be calculated

Porous glassy HL samples were prepared by sintering cone-crushed glass at 900°C. 'Plasticene' moulds coated in silver foil were packed with glass powder, and a 5wt% solution of bedocryl in acetone added. On evaporation of the acetone, the bedocryl acted as a binder, being driven off during heat-treatment. Manual grinding of the sintered bodies using fine SiC paper gave suitable samples. In order to produce sinters of different porosity, the coarseness of original powder ($\frac{1}{4}$" to $\frac{1}{32}$") and time of sintering ($\frac{1}{2}$ to 1 hour) were varied.

3.1.3 Measurement of mechanical properties

A simple compression test was used to investigate the dependence of strength and elastic modulus on microstructure. Cylindrical samples of diameter 10mm and height 15mm were loaded in compression between hardened metal plattens on an INSTRON test machine. The bottom platten was held stationary and connected to a load-cell calibrated to a maximum load of 50KN. The top platten was moved down at a constant rate of 0.1 mm/min, until failure occurred. The strength of each sample was taken as the stress at failure, calculated from the maximum load and the original cross-sectional area. An elastic modulus was found from the slope of the stress-strain curve at zero strain.

The high lime base composition, HL was used in this study. Dense glassy cylinders were prepared by casting glass from 1500°C into graphite-lubricated brass moulds of the appropriate dimensions. Immediately after casting, the samples were placed in a muffle furnace at 825°C and annealed overnight. On cooling, excess glass was removed with a circular diamond saw, and the cylinder ends ground flat and square.

Porous glassy cylinders were prepared by heating 200g batches of glass powder mixed with 5-10g of dextrin ($C_6 H_{10} O_5$) to act as a gas bubble former. Fireclay crucibles were used. By varying the temperature of treatment from 1450°C to 1480°C and time from 25-35 minutes, it was

possible to produce porosities ranging from 0 to 25%. After annealing, a horizontal section ∿30mm thick was cut from each crucible, and 10mm diameter cores cut into these sections with a diamond tool. It was found that the cores remained intact if 5mm of glass was left uncored at the bottom of the sections. Cylinders were subsequently released using a diamond saw to cut horizontally across the bottom of each core. The ends of the cylinders were cut square using a precision Buehler 'Isomet' low speed diamond saw, and finished on fine SiC paper.

Some cracking of the glass occurred due to the difference in thermal expansion between the crucibles and the glass. It is estimated that only 60% of the attempted cores successfully produced compression specimens, the remainder shattering or cracking at some stage of fabrication.

Dense partially crystalline samples were prepared in a similar manner, but without the dextrin addition, using melting temperatures of 1380°C to 1400°C for periods of 1 hour.

3.1.4 Measurement of thermal expansivity

Determination of thermal expansion coefficients was carried out using a silica dilatometer. The dimensional changes of a rectangular sample ∿ 10 x 5 x 5 mm were measured by a silica thrust rod pressed lightly against the end of the sample. Movement of the thrust rod was converted to an electrical output using a transducer (linear variable differential transformer). Change in sample length was thus recorded as a function of temperature, a correction being made to account for the expansion of the silica holder. Sample temperature was increased at a rate of 20°C/min.

Expansion coefficients were calculated as the rate of length increase per unit temperature rise over the range room temperature to 700°C. Glass transition temperatures, Tg, and dilatometric softening

temperatures, Mg, were estimated from the appropriate changes in slope. Tg corresponds to a viscosity of $10^{13.6}$ Poise, Mg to $10^{12.5}$ Poise.[108]

The samples used were those previously prepared for other property determinations. Dense glasses came from the crystallisation rate studies, porous glasses from the mechanical properties specimens, and crystalline samples from the thermal conductivity specimens.

3.2 The decomposition of iron sulphides

The role of iron sulphides in deposit formation is of fundamental importance. This study has considered the effect of atmosphere and thermal history on the decomposition of pyrite (FeS_2) and pyrrhotite ($Fe_{1-x}S$).

3.2.1 Iron Sulphides used in this study

A commercially available sample of Peruvian pyrite was found to be almost pure FeS_2. E.P.M.A. indicated that silicon and magnesium were the major impurities, and both were present in amounts <0.5wt% of stoichiometric oxide. In terms of iron and sulphur, the average sample analysis was 52.7wt% S and 47.3wt% Fe. The X.R.D. pattern closely matched the standard for pyrite,[109] with no detectable additional phases.

It was not possible to obtain a pure mineral sample of pyrrhotite. Therefore, pyrrhotite was prepared by decomposing pyrite in an argon atmosphere by holding for 30 minutes at 700°C. The sample was analysed by E.P.M.A. and gave 38.5wt% S and 61.5wt% Fe. X.R.D. analysis gave a close match with the pyrrhotite standard.[110]

While variations in the diffraction patterns for pyrrhotites with different Fe:S ratios have been reported, the laboratory-prepared material and the standard showed a close match with both 'd' spacings and Fe:S ratio.

3.2.2 Decomposition of pyrite

The decomposition of pyrite in air, 2% oxygen in nitrogen, and a pure nitrogen atmosphere was studied.

The pyrite sample was first finely ground in a TEMA mill, and then 2.0g samples were pressed at $75MNm^{-2}$ to give 12.7mm diameter pellets. The pellets were placed in a vertical tube furnace with a flowing gas atmosphere, and heated for 15 minutes at temperatures ranging from $300^{o}C$ to $1100^{o}C$.

Decomposition products were determined by X.R.D. analysis using a Philips powder diffractometer. Qualitative estimates of the relative proportions of the phases present were made by comparison of the strongest diffraction lines from each of the phases present in the heat-treated samples.

3.2.3 Decomposition of pyrite and pyrrhotite in a drop-tube furnace

The drop-tube furnace used is shown in Figure 5. It consisted of two furnaces, one on top of the other. The top furnace contained a single SiC spiral element, with a maximum operating temperature of $1500^{o}C$. The lower furnace had a 'Fecralloy' wound element, with a maximum temperature of $1200^{o}C$. These units simulated the flame and the tube-walls respectively.

Finely ground mineral samples of $\sim$5g were introduced into the top of the furnace via a vibratory feeder (0.3g/min). The temperature of the top furnace was varied from $850^{o}C$ to $1350^{o}C$, that of the bottom furnace between $700^{o}C$ and $800^{o}C$. An atmosphere of 2% oxygen in nitrogen was used.

FIGURE 5 - Drop-tube furnace

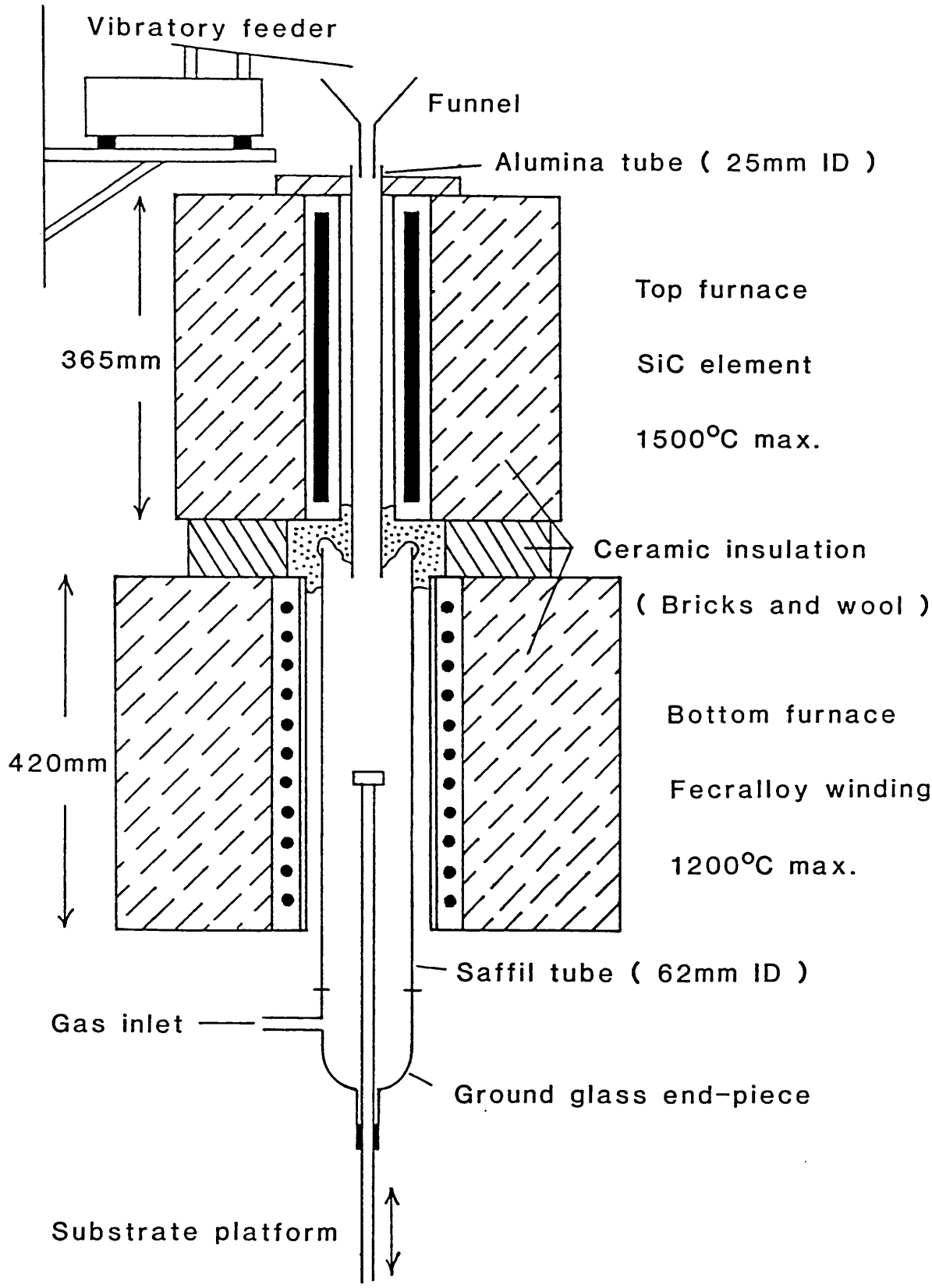

Decomposition products were collected on mild steel substrates which had been pre-oxidised to give an Fe_2O_3 surface layer similar to that found on the surface of tubes in operating boilers.[111] The substrates were held in the lower furnace at an angle of 60^o to the vertical, so that only molten or partially molten products would be expected to adhere to the metal surface.

The deposits were analysed by X.R.D. and internal microstructures examined by scanning electron microscopy of fracture surfaces, and optical microscopy of polished surfaces.

3.3 Microstructural examination of boiler deposits

A wide variety of deposits from six utilities have been examined. Where possible, the exact points of collection were identified, as these are essential in estimating likely deposit temperature and the local atmosphere.

The first stage of slag examination was purely visual. General structure was described, and orientation with respect to tubeside and fireside achieved if possible. This information was then used in deciding which sections to examine, and the number of samples to take on each section. Subsequent microstructural analysis involved three techniques.

X.R.D. analysis of powdered samples identified the crystalline phases present, and gave some indication of the relative amounts.

Optical microscopy of polished sections in reflected light elucidated phase distribution and morphology. Sections were prepared by mounting 1cm cubes in a cold-setting polyester resin, and polishing on progressively finer SiC papers and, finally, diamond laps.

Scanning electron microscopy was used in two modes. Firstly, observation of fracture faces and natural surfaces gave an overall impression of the deposit microstructure, ranging from lightly sintered and glassy to highly sintered and highly crystalline. Secondly, E.P.M.A. of polished sections was used to determine chemical compositions, giving both bulk analyses (average of 5–10 individual determinations) and variations across a sample.

The six utilities from which the deposits were collected are described in the appendix. In the case of Station 6 samples, selective heat-treatments were used to investigate the unique two-tone reflectivity of the iron-rich phases present. The experimental work undertaken will be described in section 4.3.6.2, as it logically follows on from the microstructural examination of the deposits.

CHAPTER 4

Results

4.1 Properties of glasses and partially Crystalline Materials

4.1.1 Crystallisation rates of model glasses

The heat-treatment method described in section 3.1.1 proved very successful in determining the crystallisation rates of glasses as a function of temperature.

Crystal layer thickness generally varied sigmoidally as a function of time at any temperature, due to nucleation effects at relatively short times, and depletion effects at long times, i.e. long range diffusion controlled growth. The maximum slope was taken as the maximum growth rate characteristic of each temperature.

The variation of rate with temperature agreed well with the classical approach of Turnbull & Cohen[42]. The crystalline phases detected by XRD analysis were those predicted by the equilibrium phase diagram.

Figure 6 shows the crystallisation behaviour of the two whole lignitic ash compositions. Composition 1 crystallised to give anorthite as the primary phase, and had a maximum growth rate of 12.4 $\mu m\ S^{-1}$ at a temperature of 1285°C, corresponding to a calculated viscosity of the glass of 1170 Poise. Composition 2 also crystallised to give anorthite, and had a maximum rate of 20.1 $\mu m\ S^{-1}$ at 1275°C, with a corresponding viscosity of 900 Poise.

Figure 7 shows the results for Composition 3. In this case, the growing phase was mullite and growth was internally nucleated. The longest needle on each section examined was taken as the characteristic length for each time. The maximum growth rate was 0.014 $\mu m\ S^{-1}$ at a temperature of 1380°C with a corresponding viscosity of 3450 Poise.

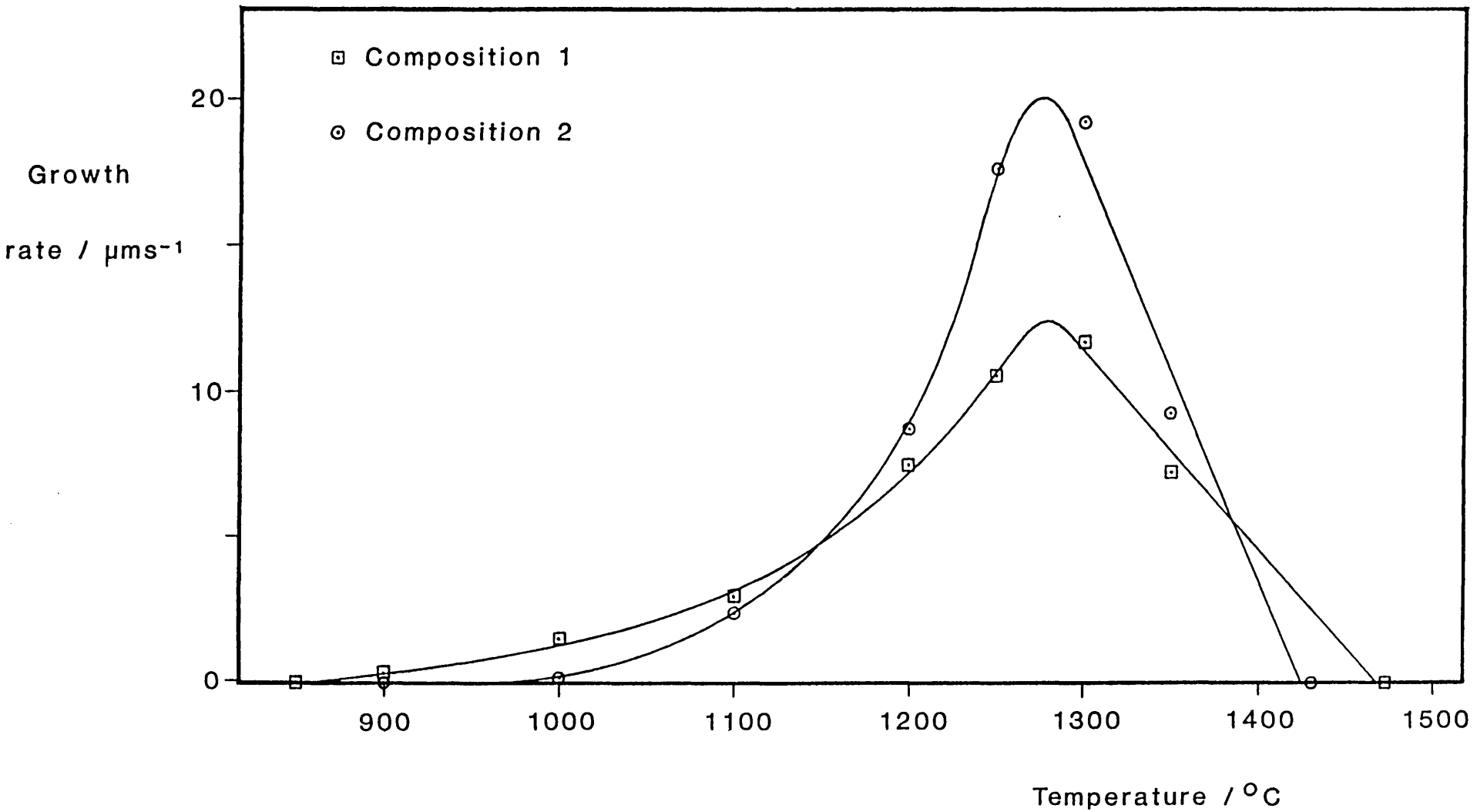

FIGURE 6 - Crystal growth rates of compositions 1 and 2

FIGURE 7 – Crystal growth rates of composition 3

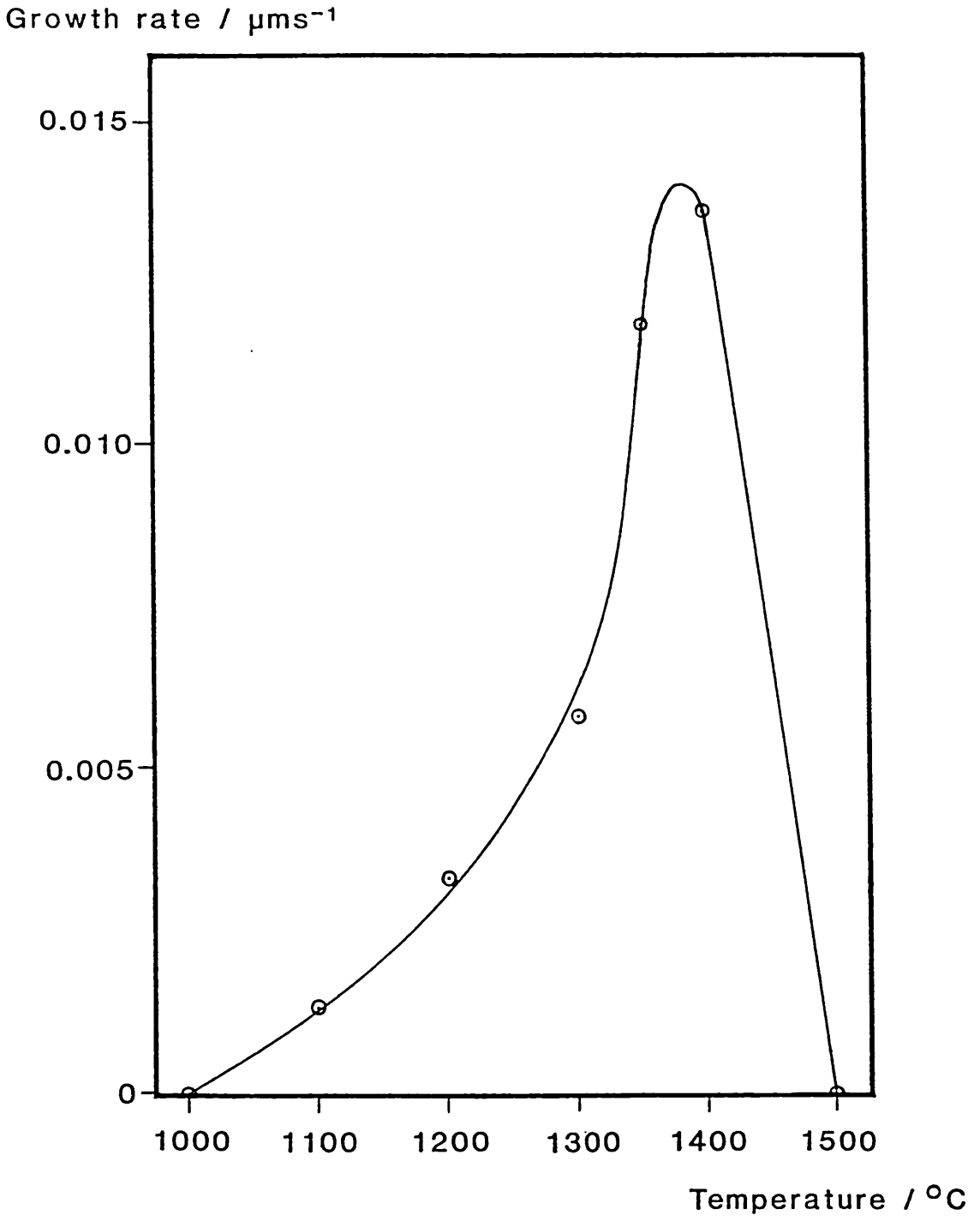

Maximum rate = 0.014 μms^{-1}

Temperature of maximum rate = 1380°C

Figure 8 shows the crystallisation rates of the high lime glass (HL) and the effect of additions of MgO, Fe_2O_3, Na_2O and K_2O on its behaviour. Gehlenite was the primary crystalline phase, though in the case of the iron-containing glass a large degree of iron solid solution ($\sim$ 10 wt % Fe_2O_3) was detected in a melilite phase, using both XRD analysis and EPMA. Minor amounts of anorthite and wollastonite were detected below 1100°C. Figure 9 shows a similar set of curves for the low lime glass (LL). In those, anorthite was the primary phase, with minor amounts of wollastonite detected below 1100°C.

Table 8 shows a summary of the crystal growth rate results. The maximum rate and the temperature at which this rate occurred are shown for each glass, together with the liquidus temperatures predicted from equilibrium phase diagrams and the calculated viscosity of each glass at the temperature of maximum rate.

Plates 1, 2 and 3 are typical optical micrographs illustrating surface nucleated growth of anorthite (fully crossed polars) and gehlenite (half crossed polars), and spherulitic internal nucleation of gehlenite (fully crossed polars) respectively. In all cases, except Composition 3, internal nucleation occurred only at temperatures above 1100°C, and at treatment times which were long in comparison to those needed to attain the maximum rate. It was felt, therefore, that surface growth was only minimally affected by the occurrence of internally nucleated growth.

FIGURE 8 – Crystal growth rates of the high lime glasses

(Melilite)

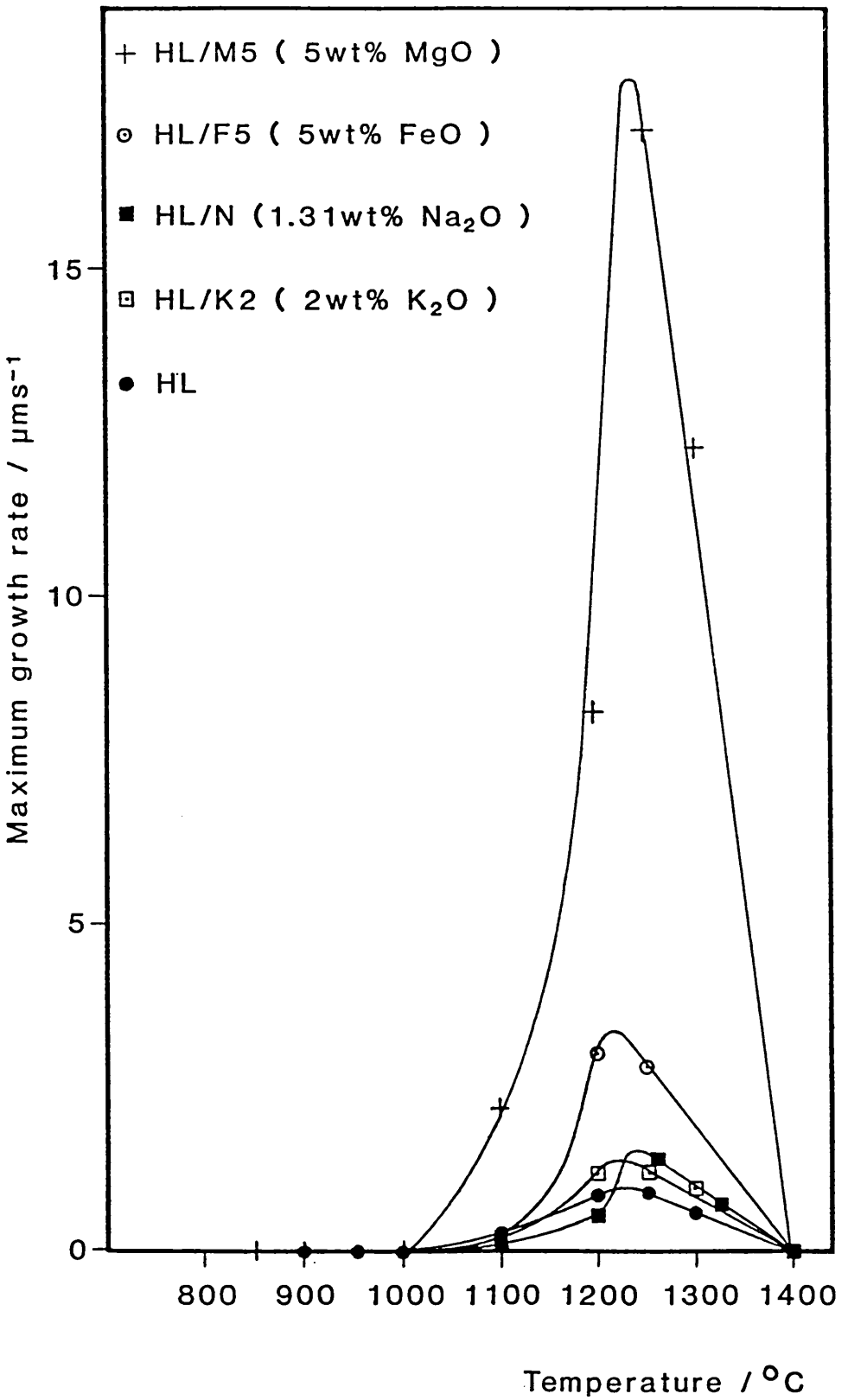

FIGURE 9 - Crystal growth rates of the low lime glasses

(Anorthite)

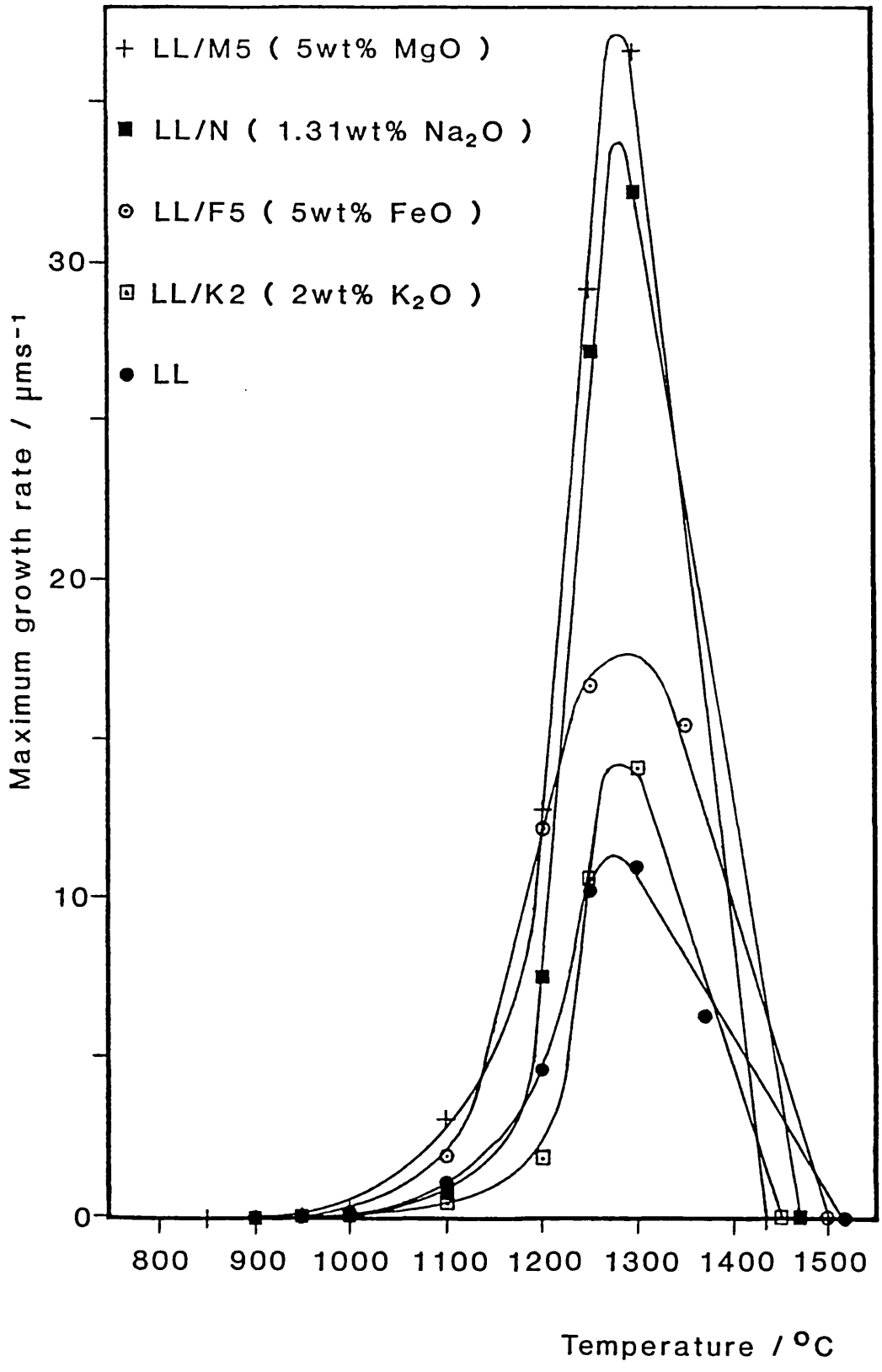

TABLE 8 - Summary of the results of the crystallisation studies on model ash compositions

	Primary crystallisation product	Maximum growth rate $\mu m\ s^{-1}$	Temperature of max. rate Tmax/^{o}C	Viscosity at Tmax Poise	Liquidus temperature ^{o}C
HL	geh	0.85	1225	190	1400
HL/K2	geh	1.19	1220	180	1400
HL/N	geh	1.39	1235	170	1400
HL/F5	mel	3.39	1220	210	1400
HL/M5	geh	18.20	1240	105	1400
LL	an	11.3	1270	1905	1520
LL/K2	an	14.2	1280	1480	1470
LL/F5	an	17.8	1290	1230	1500
LL/N	an	33.9	1280	1480	1470
LL/M5	an	37.1	1280	890	1420
Comp 1	an	12.4	1285	1170	1470
Comp 2	an	20.1	1275	900	1430
Comp 3	mull	0.014	1385	3450	1500

Key to crystallisation products -

geh - gehlenite
mel - melilite
an - anorthite
mull - mullite

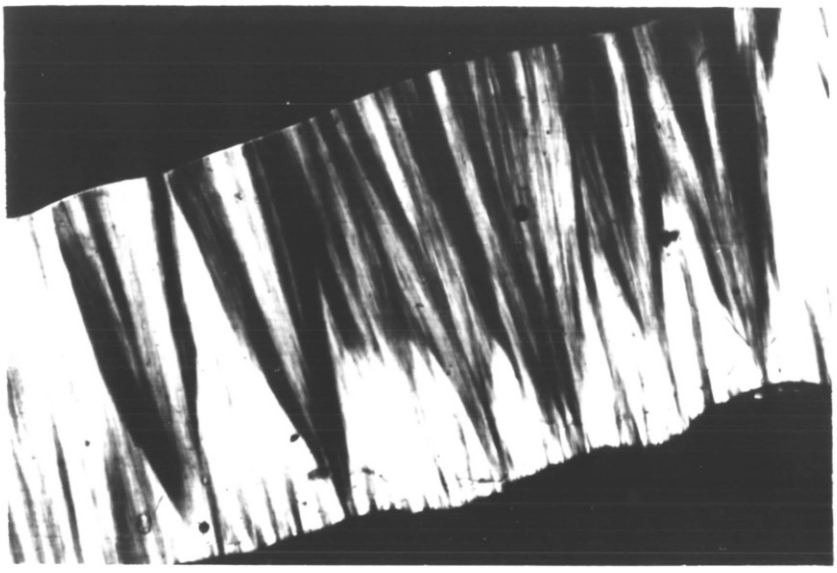

PLATE 1 - Surface growth of anorthite (x 75)

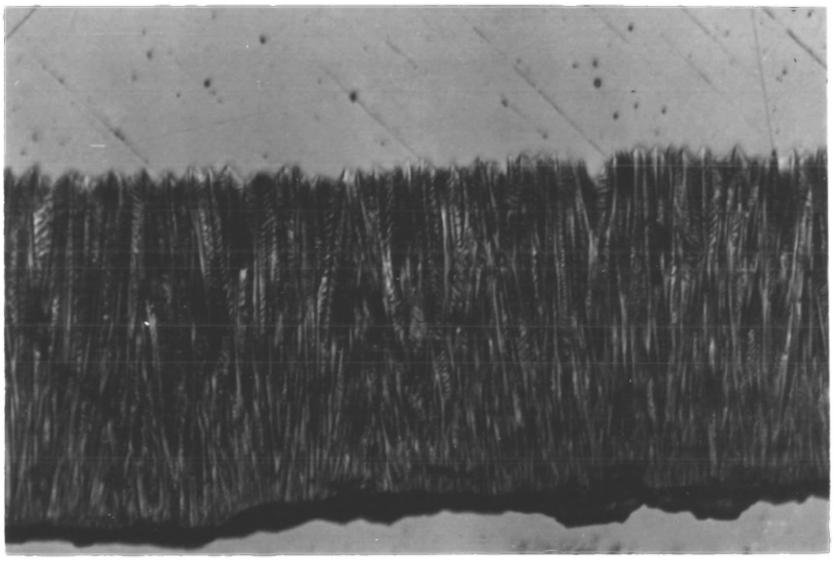

PLATE 2 - Surface growth of gehlenite (x 75)

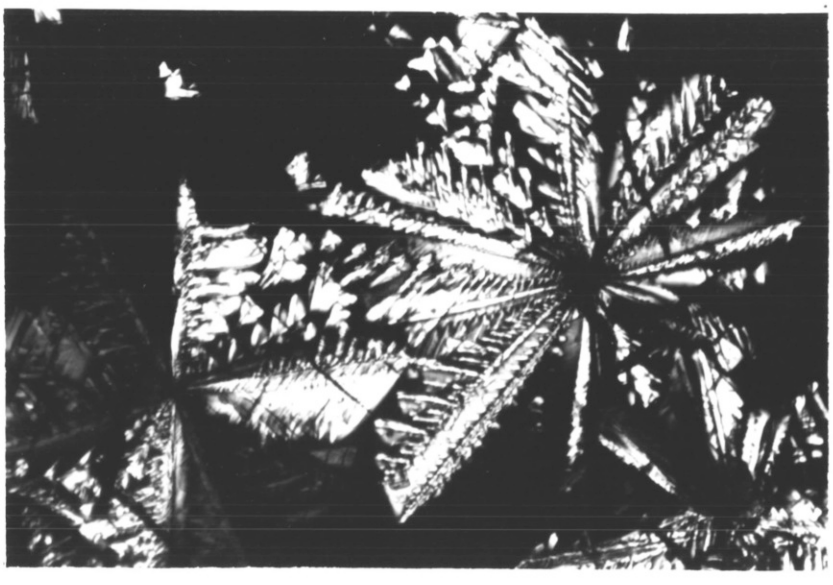

PLATE 3 - Internal growth of gehlenite (x 75)

4.1.2 Thermal Conductivity

Measurements were carried out with samples in the temperature range 140-160°C. The thermal conductivity of the model glass composition LL was 1.34-1.50 $Wm^{-1}K^{-1}$ over this range, while that of composition HL was 1.19 - 1.32 $Wm^{-1}K^{-1}$.

On crystallisation, LL samples containing solely anorthite had conductivities in the range 1.10 - 1.17 $Wm^{-1}K^{-1}$, much lower than the corresponding glass. Crystallised HL samples, containing gehlenite with minor amounts of anorthite, had conductivities between 1.20 and 1.45 $Wm^{-1}K^{-1}$, somewhat similar to the parent glass.

Porosity was found to have a profound effect on thermal conductivity. Figure 10 shows the measured conductivities of porous HL samples at 150 ± 5°C. Also included in this figure are the theoretical composite conductivities at 150°C calculated from the slab and dispersed sphere models described in section 2.7.2.2.. In these calculations the conductivity of dense HL glass was taken as 1.23 $Wm^{-1}K^{-1}$ and that of air as 0.034 $Wm^{-1}K^{-1}$. (112)

4.1.3 Mechanical properties

The mechanical properties of dense HL glass were determined by testing 17 samples. The maximum compressive strength observed was 510 MNm^{-2}. Values less than this were most likely caused by macrofaults formed during casting of the specimens, and/or misallignment of the platten surfaces. The elastic modulus at zero strain was calculated to be 2.67 GN m^{-2}.

The effect of crystallisation on mechanical properties of the high lime composition (HL) was investigated using two sets each of 15 samples with differing degrees of crystallinity. The degree of crystallinity was determined by lineal analysis of polished thin sections in transmitted light. One set of samples was found to be ∿9 vol % crystalline with an average intercept length of 8μm, while the other set was ∿38 vol %

FIGURE 10 – Thermal conductivity of porous HL glass

(150±5°C)

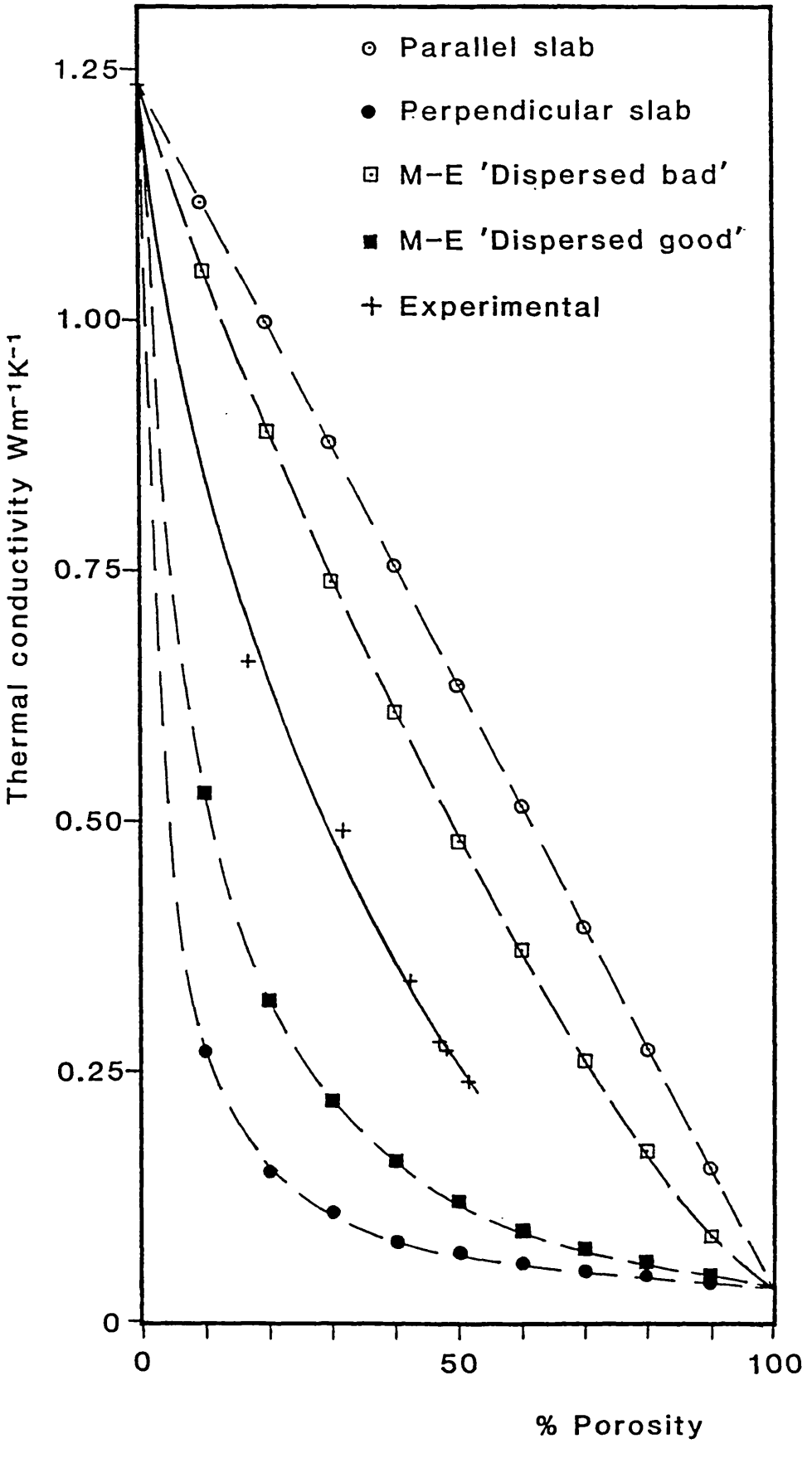

crystalline with an average intercept of 24μm. Sample porosity ranged from 7 to 17%. Crystallites were tabular and had nucleated both internally and at pore surfaces. Figures 11 and 12 show the compressive strength and elastic moduli data for these samples. Approximately one third of the samples tested were imperfect, fracturing at loads less than 750kg, and hence were neglected.

The mechanical properties of porous HL glass were determined by testing 35 samples, of which 8 were imperfect and splintered at the beginning of testing. Thus, 27 data points were obtained. Pore diameters ranged from 0.1 to 1mm.

Figure 13 shows the fracture stress values for the HL glass as a function of porosity, porosities ranging from 0 to 21.4%. Following the work of Ryshkewitch[101] Figure 14 shows this data replotted to test the relationship:

$$\sigma = \sigma_o \exp(-nP)$$

For this material, the data points lie between n = 2 and n = 4. Figure 15 shows the elastic moduli of the porous samples at zero strain. The effect of porosity predicted by Mackenzie[102] is also shown on this figure.

Tests were also carried out on a set of standard Pyrex glass samples. For this purpose 9mm diameter rod was precision cut into 15mm lengths. The maximum compressive strength observed was 715 MNm^{-2}. The elastic modulus at zero strain was found to be 2.45 GNm^{-2}.

4.1.4 Thermal expansion

Figure 16 shows a thermal expansion curve typical of the glasses used in this study. The changes in slope correspond to the glass transition temperature, Tg, and the dilatometric softening temperature, Mg. Expansion coefficients were calculated from the straight line portion of the graph between 100°C and 700°C, and are accurate to ± 0.05 $x10^{-6}\ {}^{o}C^{-1}$.

FIGURE 11 – Compressive strengths of partially crystalline porous HL samples

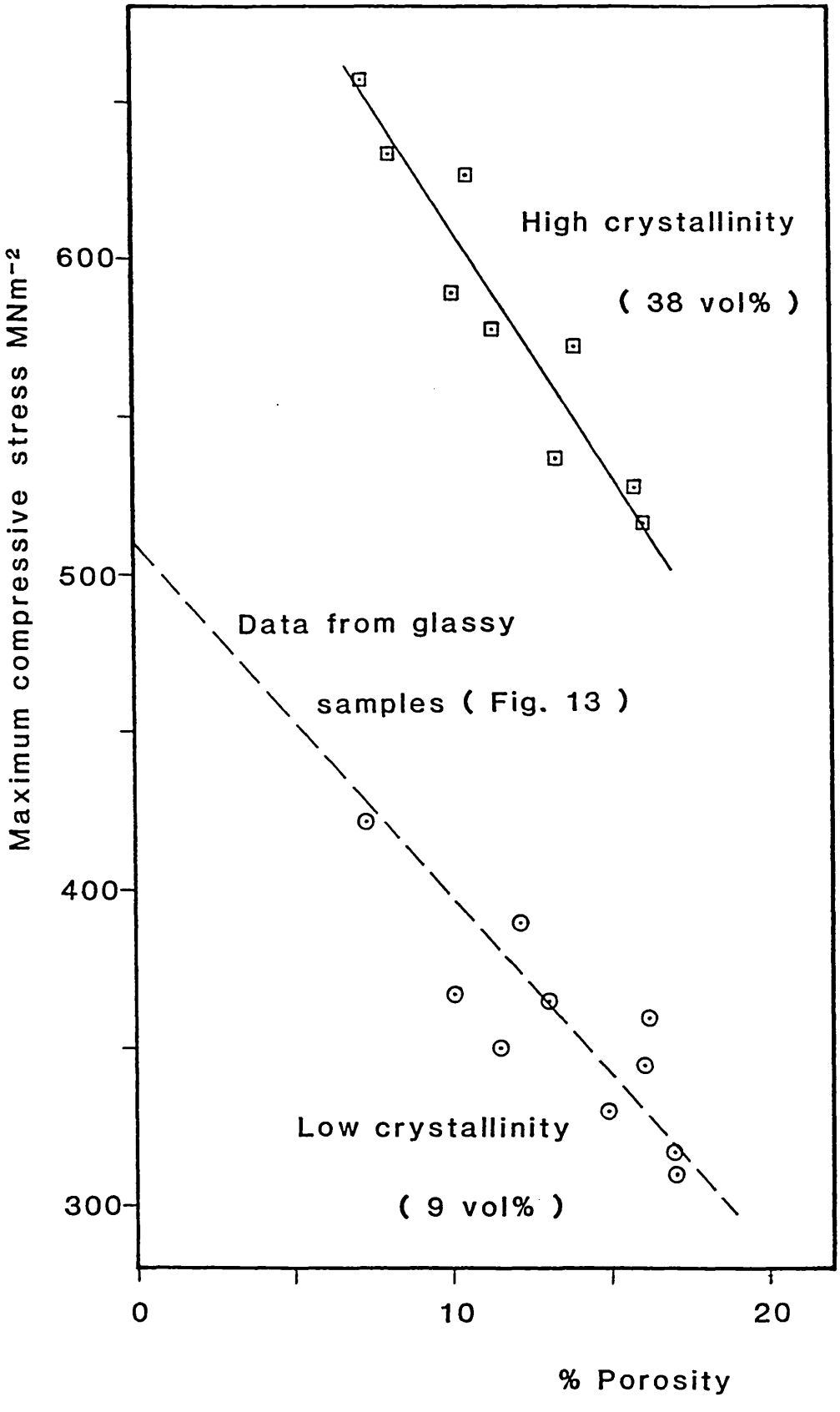

FIGURE 12 – Elastic moduli of partially crystalline porous HL samples

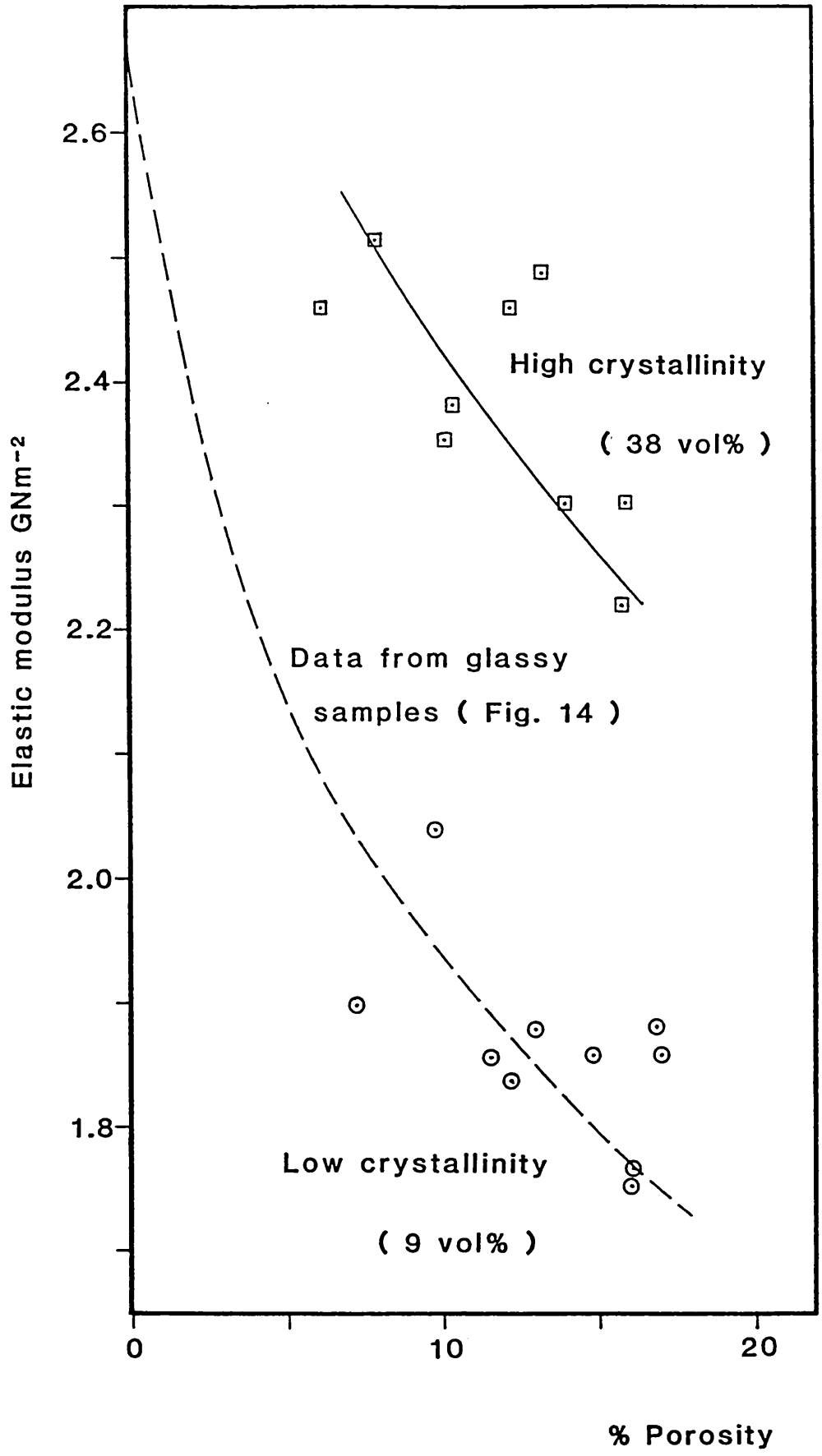

FIGURE 13 - Compressive strength of porous HL glass

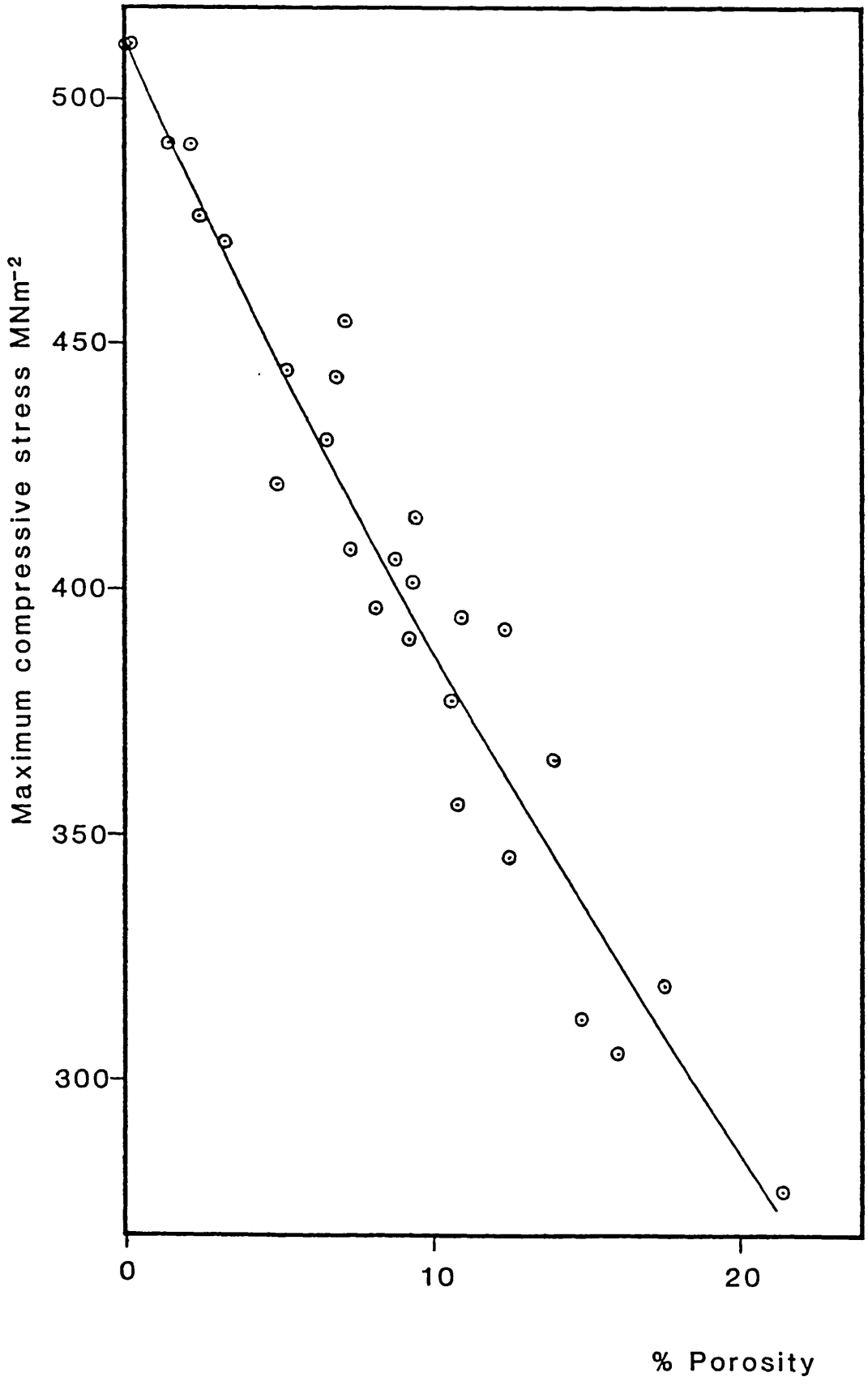

FIGURE 14 - Logarithmic plot of compressive strengths of porous HL glass [101]

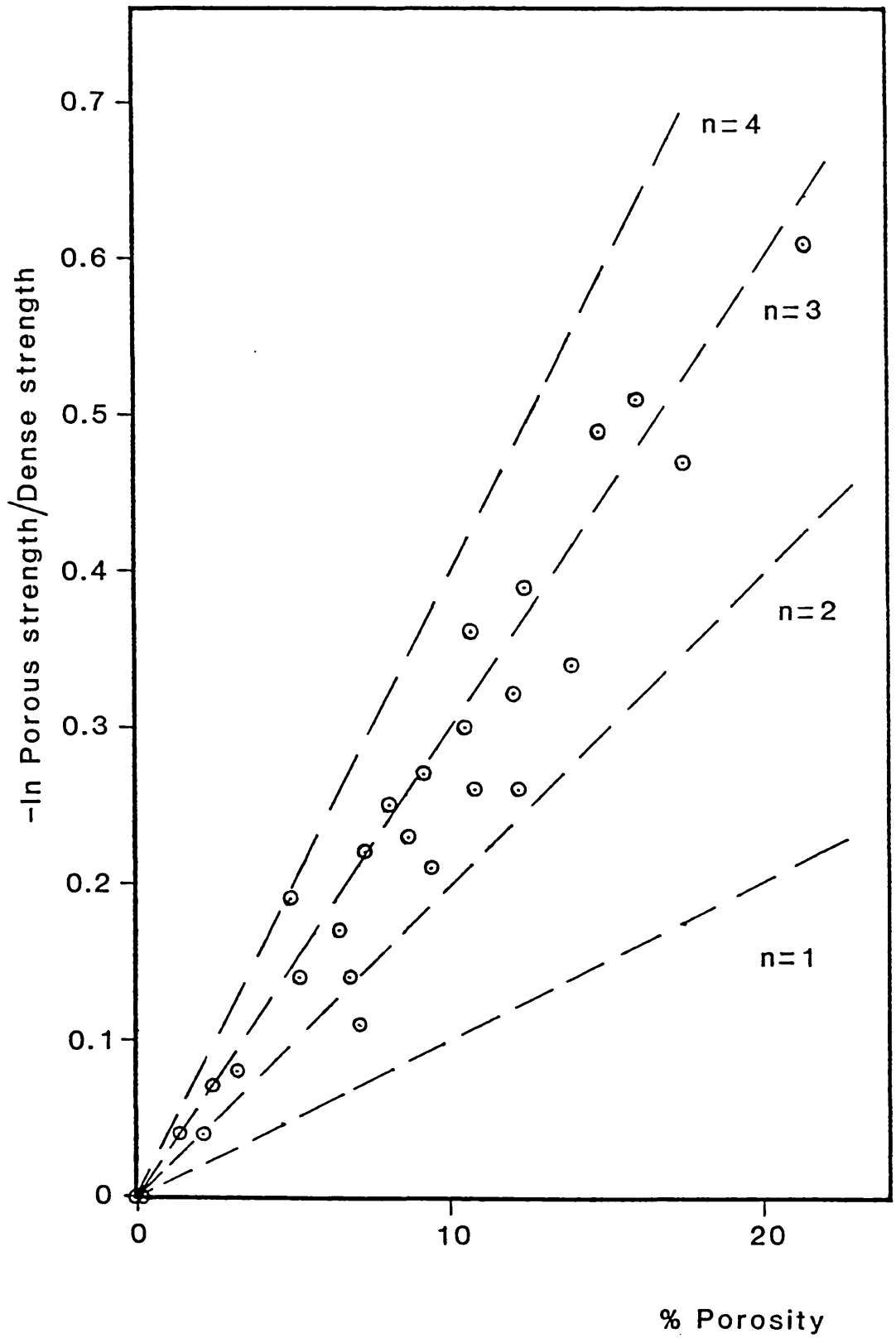

FIGURE 15 - Elastic moduli of porous HL glass

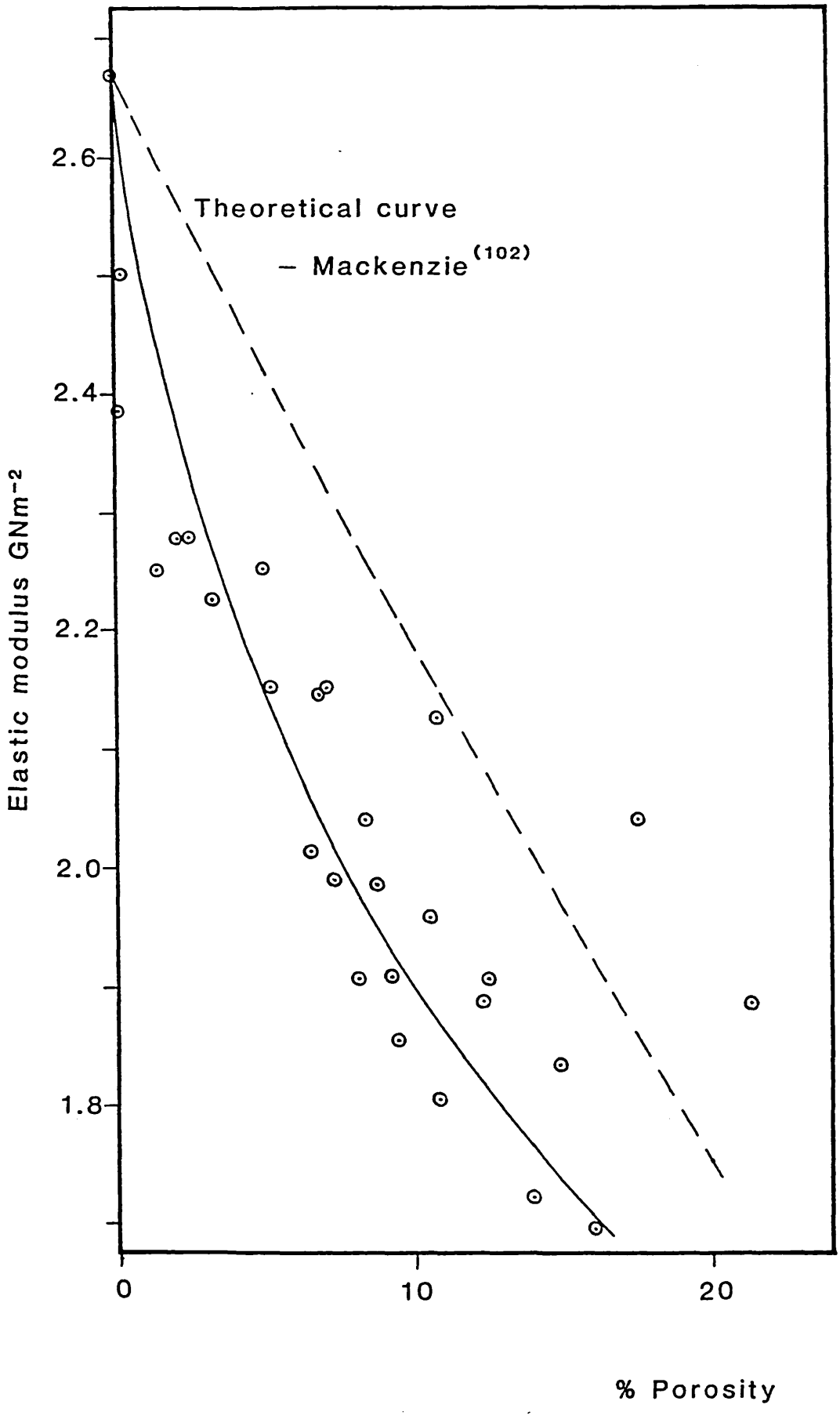

FIGURE 16 – The thermal expansion curve of LL glass

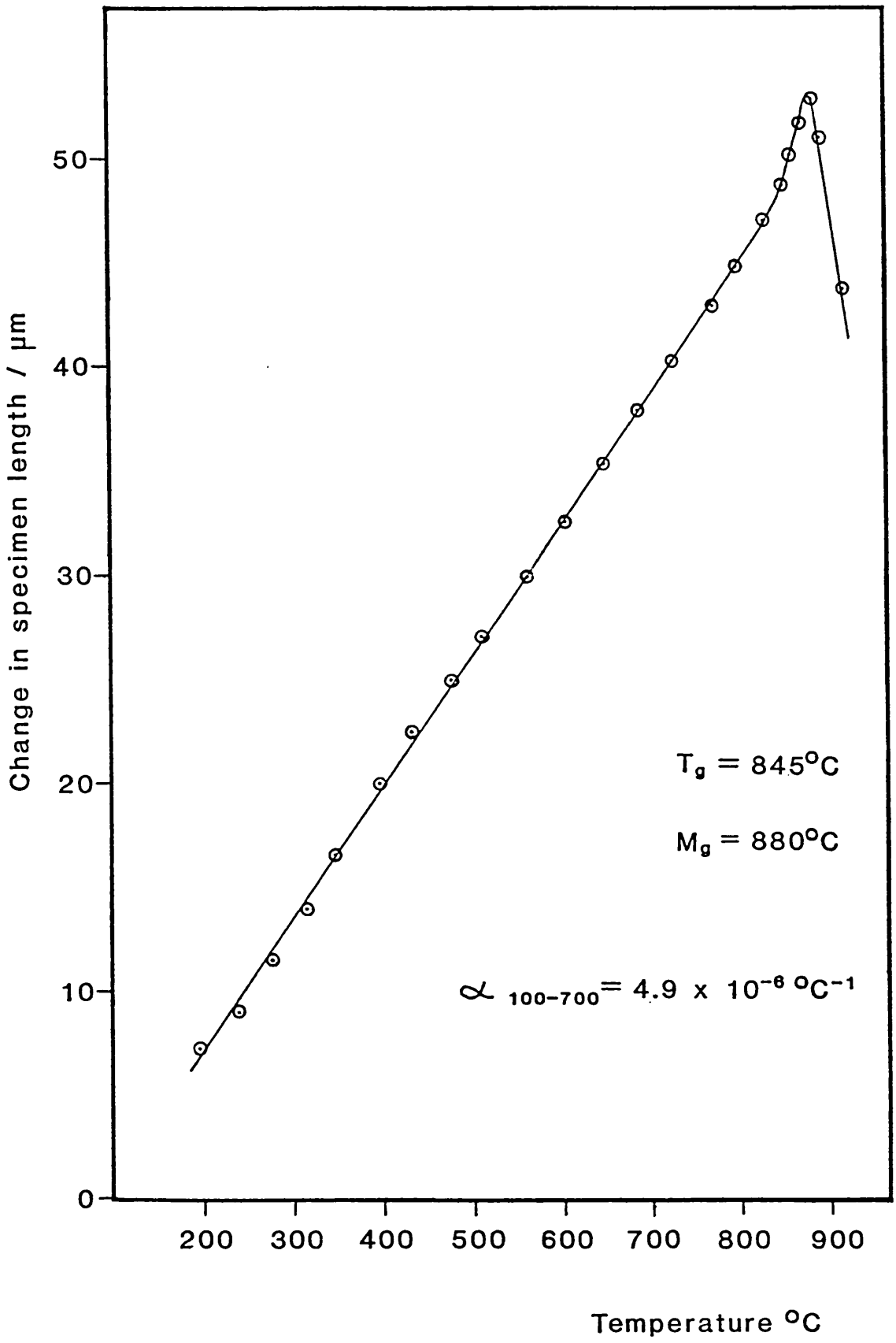

Table 9 summarises the thermal expansion behaviour of the 13 glasses used in the crystallisation rate studies. The table includes the linear expansivities, the molar acid:base ratios calculated from the composition of each glass, and Tg and Mg for each glass.

Crystalline samples from the HL composition were found to have an expansivity of 8.30 x 10^{-6} $^{o}C^{-1}$ over the range 100-700^{o}C. Glass transition and softening points were observed, and must be attributed to the relatively small amounts of residual glass in the samples. The expansion of crystallised LL composition increased approximately linearly up to the experimental limit (1000^{o}C). Thermal expansivity over the range 100-700^{o}C was found to be 6.40 x 10^{-6} $^{o}C^{-1}$.

Table 10 shows the expansivity, Tg and Mg for the five porous HL glass samples. Porosity had no effect on the thermal expansion behaviour over the temperature range investigated.

4.2 The thermal decomposition of iron sulphides

4.2.1 Decomposition of pyrite in a tube furnace

XRD powder analysis of heat-treated pyrite pellets showed that pyrrhotite, hematite and magnetite are the products of decomposition and subsequent oxidation of pyrite. Atmosphere was found to have a large effect on the proportions of these products formed.

Figures 17, 18 and 19 show the relative proportions of pyrite, pyrrhotite, magnetite and hematite in air, 2% oxygen in nitrogen, and nitrogen respectively, over the temperature range 300-1100^{o}C.

In an air atmosphere, the pyrite pellets started to lose sulphur at 400^{o}C, with the formation of pyrrhotite and hematite. The last traces of pyrite were detected at 800^{o}C. As the holding temperature was increased from 400^{o}C, the amount of hematite and pyrrhotite initially increased, with the proportion of hematite showing a maximum in the range 800 - 900^{o}C. At 1000^{o}C a minimum in the amount of hematite

TABLE 9 - Thermal expansion behaviour of model glasses

Molar acid : base		Expansivity α 100-700°C x 10^{-6} °C^{-1}	Tg °C	Mg °C
7.46	Comp 3	4.25	720	785
3.24	LL	4.75	845	880
3.13	11/F5	4.79	715	775
3.13	Comp 1	4.68	735	790
3.05	LL/N	4.82	820	855
3.05	LL/K2	4.79	820	865
2.92	Comp 2	4.98	700	745
2.36	LL/M5	5.07	785	825
1.28	HL/F5	7.51	705	760
1.28	HL	7.44	805	830
1.23	HL/N	7.48	790	825
1.23	HL/K2	7.56	775	825
1.07	HL/M5	7.63	775	800

Note

Tg corresponds to a viscosity of $10^{13.6}$ Poise.

Mg corresponds to a viscosity of $10^{12.5}$ Poise.

TABLE 10 - Thermal expansion properties of porous HL glass

% Porosity	$\alpha_{100-700^{\circ}C}$ $\times 10^{-6}\ ^{\circ}C^{-1}$	Tg/°C	Mg/°C
0	7.44	805	830
4.6	7.46	810	840
6.4	7.49	810	840
8.1	7.42	805	840
14.5	7.44	810	840
27.6	7.46	810	845

FIGURE 17 – The decomposition products of pyrite pellets in an air atmosphere

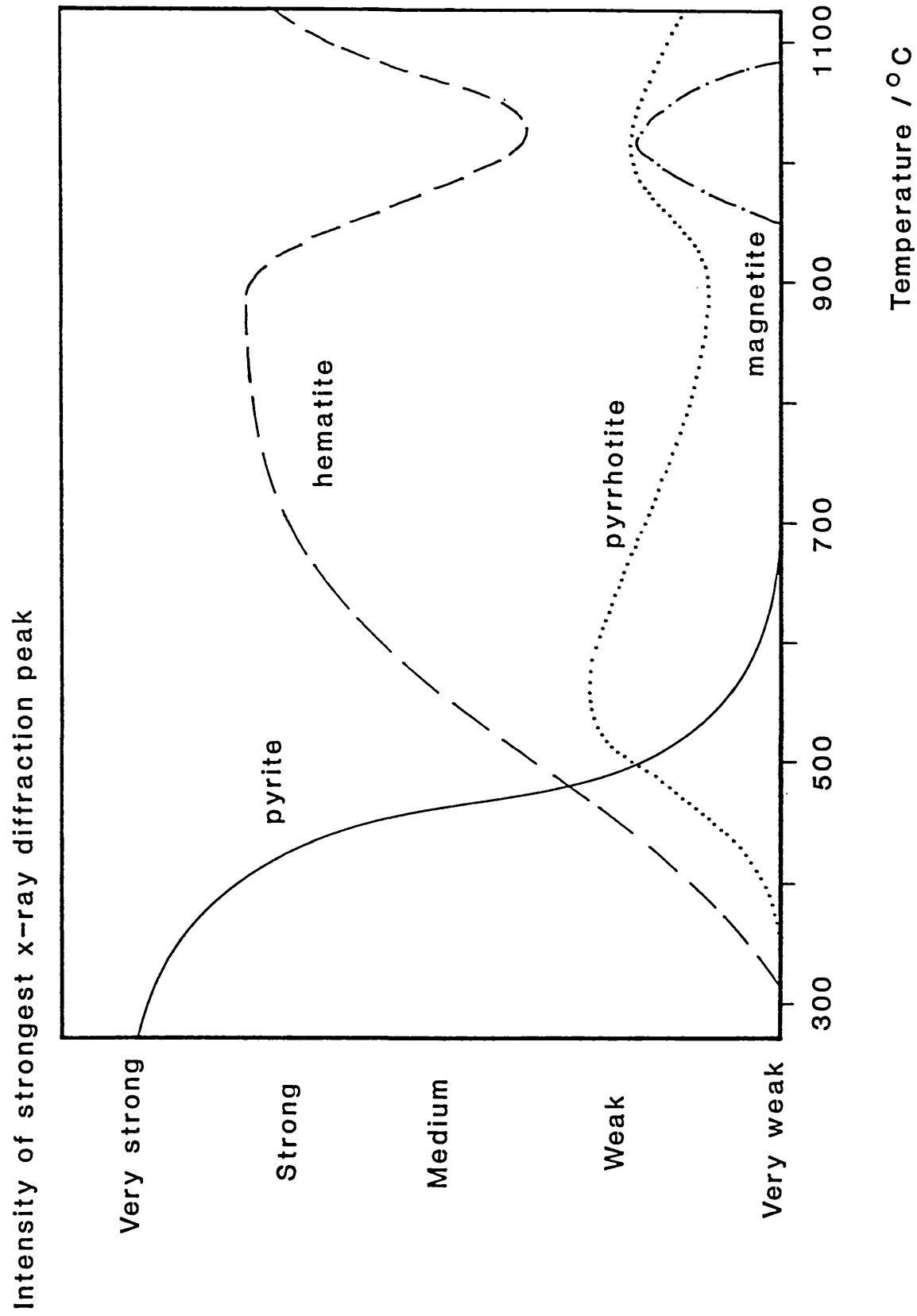

FIGURE 18 - The decomposition products of pyrite pellets in an atmosphere of 2% oxygen in nitrogen

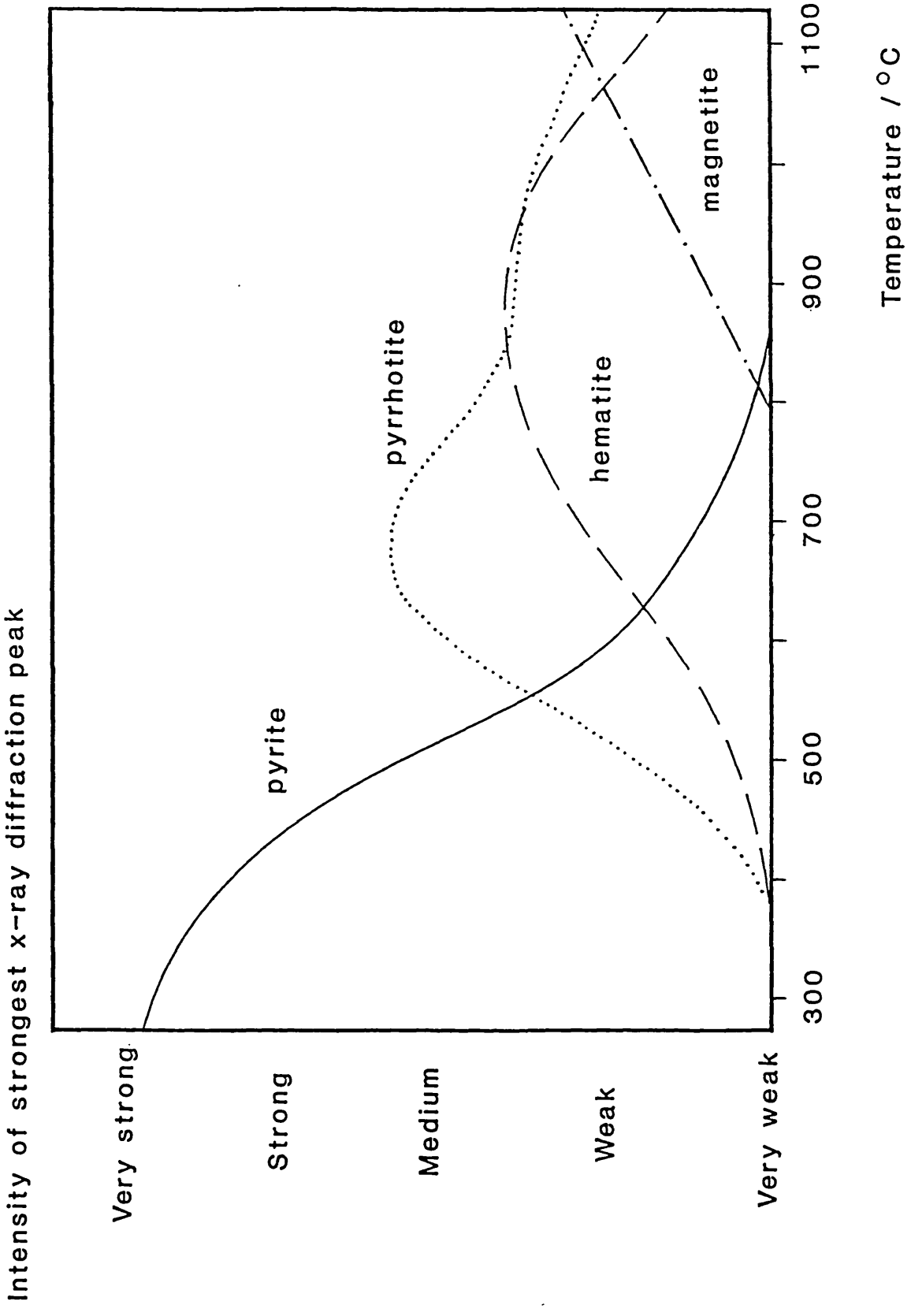

FIGURE 19 – The decomposition products of pyrite pellets in a nitrogen atmosphere

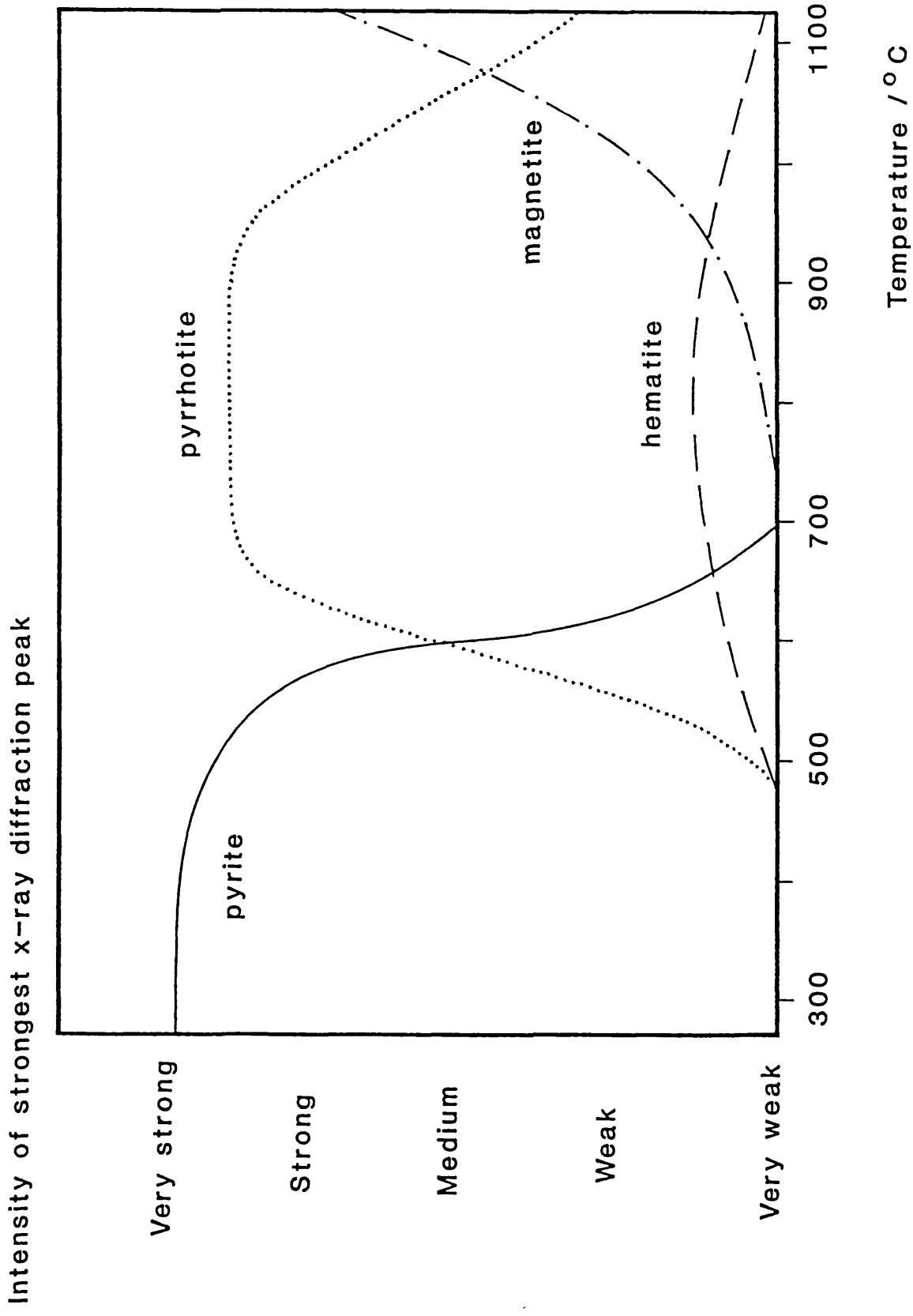

corresponded with a maximum in the amount of magnetite detected. At 1100°C only hematite and pyrrhotite were detected.

When the pyrite was heated in an atmosphere of 2% oxygen in nitrogen, the samples lost sulphur from 350°C upwards, with relatively more pyrrhotite being formed than in an air atmosphere. The final traces of pyrite were detected at 900°C. Much less hematite was formed than in an air atmosphere, the maximum being formed in the range 800-900°C. Above 900°C the amount of hematite formed decreased steadily with increasing temperature, while the amount of magnetite increased. At 1100°C magnetite was the major phase with only traces of pyrrhotite and hematite remaining.

The trends which occurred in the change from an air to 2% oxygen atmosphere continued with the change from 2% O_2 to nitrogen. In an atmosphere completely free of oxygen, no iron oxides would be expected to form. However, the residual traces of oxygen in commercial O_2-free N_2 no doubt account for the formation of hematite and magnetite observed.

Pyrite was stable up to 450°C. By 700°C it had completely decomposed to form pyrrhotite, with the formation of a small amount of hematite. The pyrrhotite was stable over a wide temperature range. Magnetite was only formed above 800°C, becoming the major phase at 1100°C.

In all atmospheres, the pellets retained their original shape up to 1000°C, although considerable swelling and cracking occurred. Above 1000°C a significant proportion of liquid phase formed, and caused the material to flow readily over the ceramic substrate.

4.2.2 Decomposition of pyrite and pyrrhotite in a drop-tube furnace

Drop-tube experiments were carried out with both pyrite and pyrrhotite in an atmosphere of 2% oxygen in nitrogen, conditions chosen to closely resemble boiler furnace conditions. Temperatures in the top furnace were varied from 950°C to 1350°C, and the metal substrate from 700-800°C. Table 11 summarises the effect of varying the temperature of the top furnace on the nature of the deposits formed.

With the top furnace at 950°C the deposits consisted of angular particles with no sign of melting having taken place. The decomposition products were mainly hematite, with traces of magnetite. Very little material was retained on the metal substrate, and this showed no tendency to adhere.

When either pyrite or pyrrhotite was passed through the top furnace at between 1000°C and 1100°C, spheres were formed which adhered well to the metal surface. As the deposit layer increased in thickness, the mechanical strength decreased. XRD analysis showed that the major phase present was hematite, but with a noticeable increase in the amount of magnetite compared with runs at 950°C. Plate 4 shows a typical point of impact, where a newly arrived pyrite-derived sphere had adhered and subsequently oxidised. Plates 5 and 6 show individual spherical particles derived from pyrite and pyrrhotite respectively. Both have cellular oxide surfaces. Plates 7 and 8 show sections through a typical deposit, and further demonstrate that the deposits were formed from partially molten droplets which adhered to and spread over the substrate on impact. Under these conditions, lignitic fly-ash showed no tendency to adhere to the substrate.

TABLE 11 - Summary of drop-tube furnace experiments with pyrite and pyrrhotite

Temperature of top furnace	Crystalline phases detected		Nature of deposit
°C	Major	Minor	
950	Hematite	Magnetite	Angular particles which did not adhere to metal
> 1000 < 1100	Hematite	Magnetite	Impacted spheres, adhered well to metal. Deposit of good mechanical strength.
> 1100 < 1350	Magnetite	Hematite	Spheres formed thin deposit, with little tendency to adhere. No mechanical strength.

Steel substrate held at 700 - 800°C in bottom furnace.

Atmosphere was 2% O_2 in N_2.

PLATE 4 - Pyrite residue with top furnace at 1050°C.

PLATE 5 - Pyrite residue with top furnace at 1000°C.

PLATE 6 - Pyrrhotite residue with top furnace at 1050°C.

(White bars = 100μm)

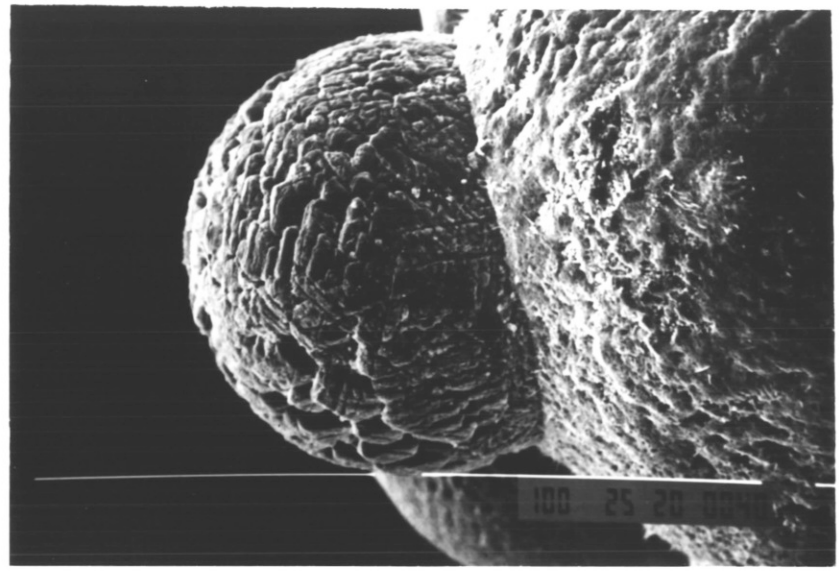

PLATE 4

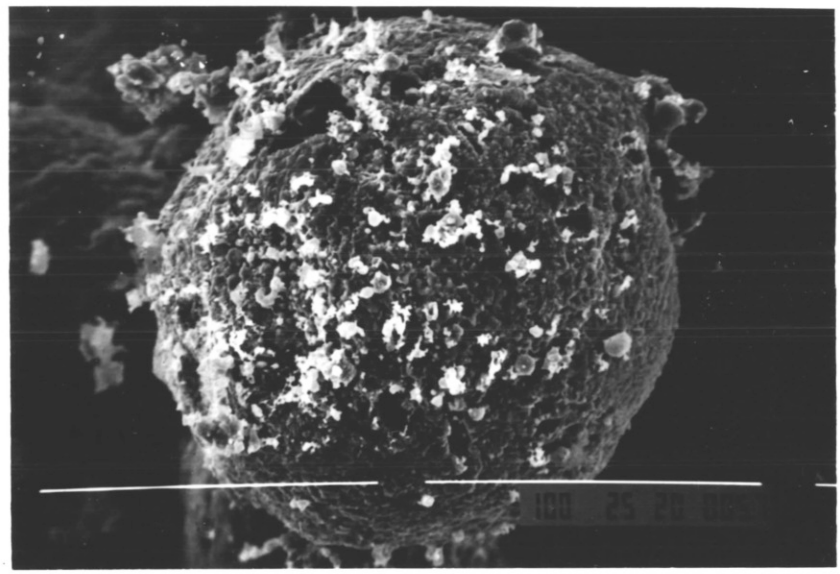

PLATE 5

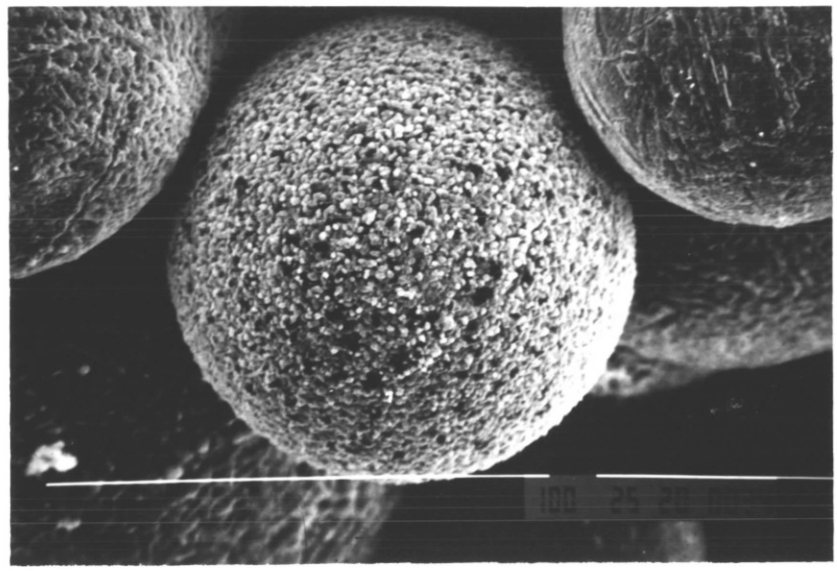

PLATE 6

PLATES 7 AND 8 - Pyrite residues with top furnace at 1050°C : Ill-defined porous hematite (bright).

(x200)

PLATE 9 - Pyrite residue with top furnace at 1150°C : Spherical particle with well-developed surface network of dendritic magnetite.

(White bar = 100μm)

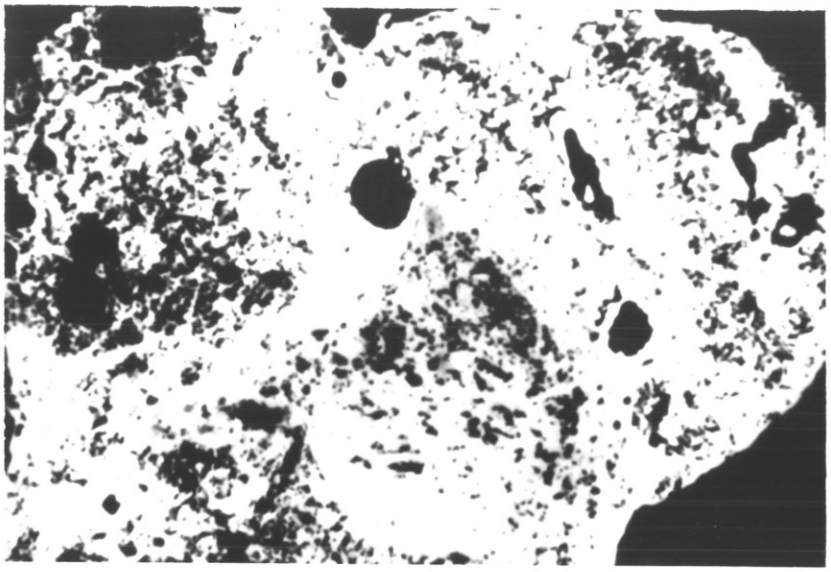

PLATE 7

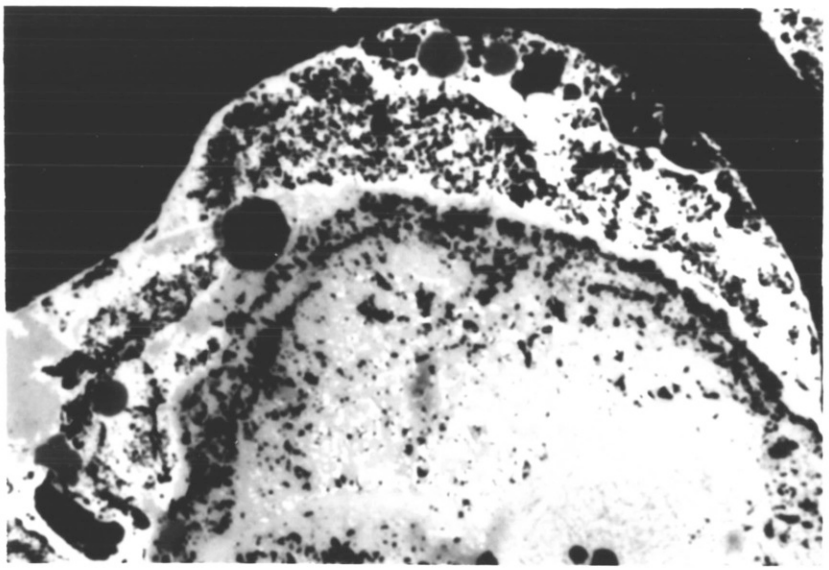

PLATE 8

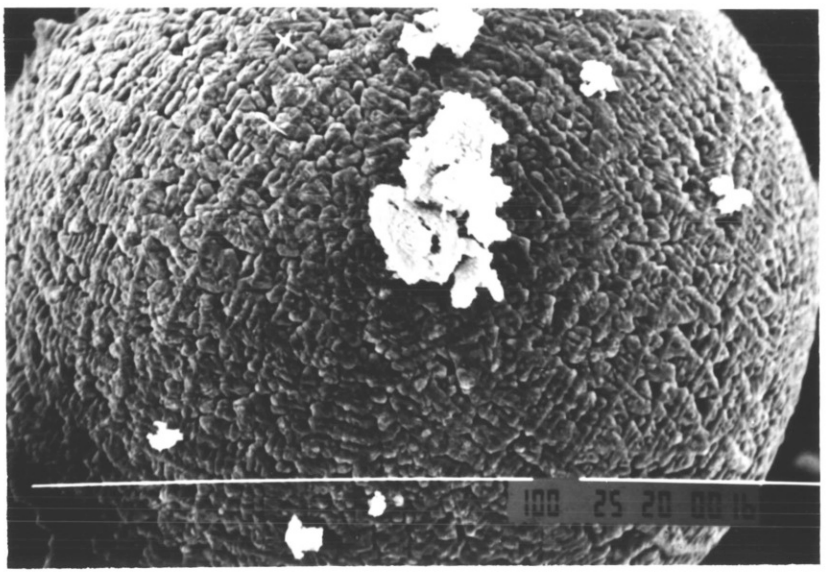

PLATE 9

When the top furnace temperature was increased to 1100°C or above spherical particles were again formed, indicating fusion, but no adherence to the substrate was observed. Magnetite was the major crystalline phase present, with small amounts of hematite. Plate 9 shows a typical particle with a well-developed network of dendritic magnetite crystals covering the surface.

4.3 The microstructural examination of boiler deposits

4.3.1 Station 1 (South Africa)

Two sets of deposits from Station 1 were examined. Both contained samples collected from around the burners of the boilers. Figure 20 shows the burner configuration and the location and extent of typical slag build-up.

The first set of deposits was collected from selected burners in boilers 5 and 6 in late February 1984. Visual inspection of the deposits showed a very wide range of structure. Plates 10, 11 and 12 are photographs of three samples which show clearly the variation in colour, and degree of sintering and vitrification. Table 12 describes the eight samples chosen for detailed examination.

Quantitative mineralogical and chemical analyses were carried out by Dr R.W. Grimshaw and co-workers at Leeds University. Their results are presented in Tables 13 and 14 respectively. The major and minor crystalline phase detected by XRD powder analysis are shown in Table 15.

These analyses clearly divide the deposits into two groups. Samples 1-6 had chemical compositions very similar to the composition of the coal ash being fired just before collection, and mineral species which would be predicted from the fusion and recrystallisation of that coal ash. Samples 7 and 8, however, contained up to 70% Fe_2O_3 mostly in the form of hematite.

FIGURE 20 - Location and extent of deposits at Station 1

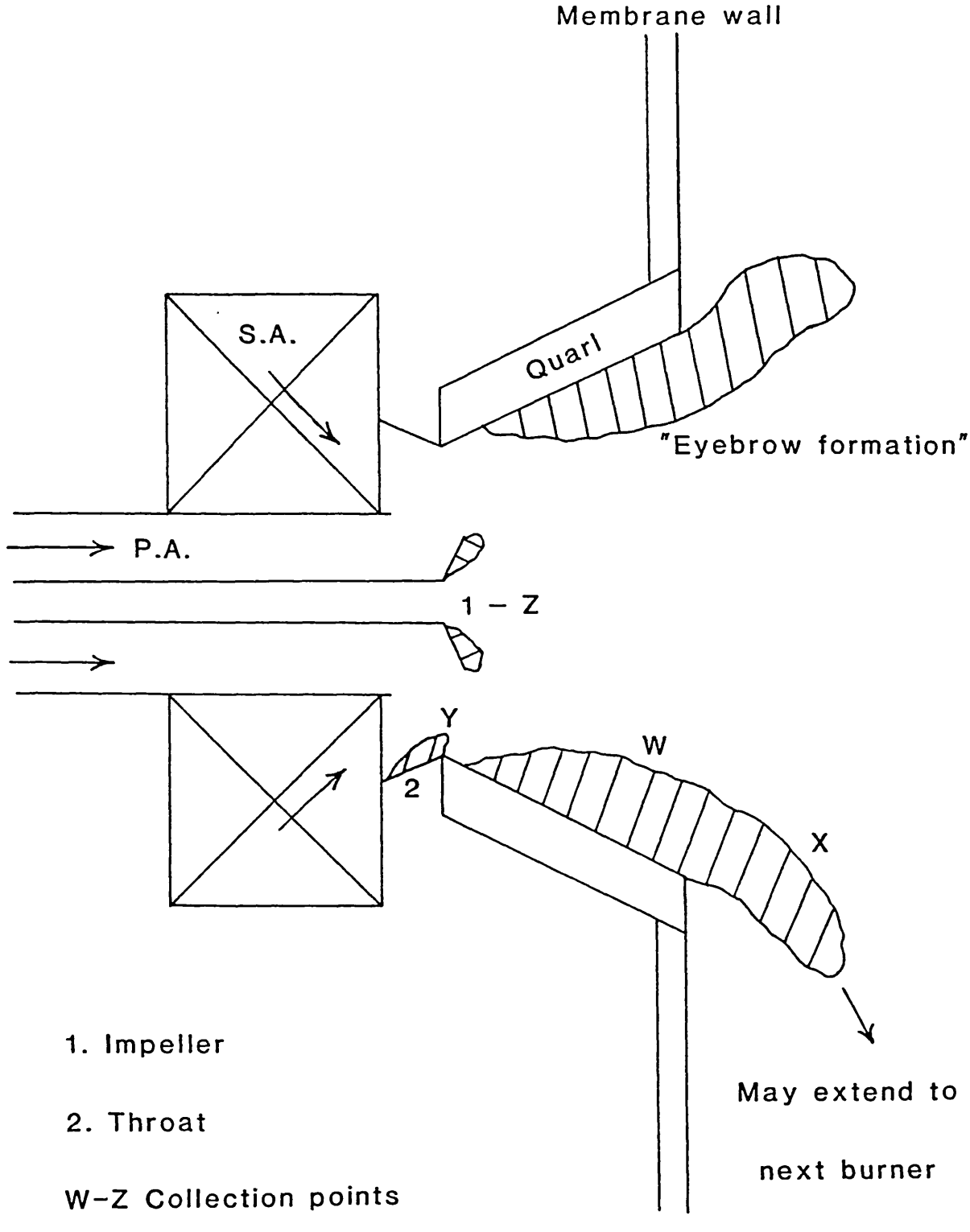

PLATE 10 - Deposit 1 from Station 1 : Coral-like deposit from cool quarl surface. (∿ 10cm x 10cm x 5cm)

PLATE 11 - Deposit 4 from Station 1 : Small burner 'eyebrow'. (∿ 10cm x 5cm x 25cm)

PLATE 12 - Deposit 8 from Station 1 : Impeller deposit fire-side. (∿ 10cm x 5cm x 3cm)

PLATE 10

PLATE 11

PLATE 12

TABLE 12 - Description and origin of deposits from Station 1

Deposit	Description		Collection point (See Fig. 20)
1	Massive coral	a) Fire-side b) Wall-side	W
2	Sintered deposit	a) Fire-side b) Black sinter c) Brown sinter	W
3	Black porous deposit	a) Sintered b) Fused	W
4	Small 'eyebrow'	a) Reverse b) Centre c) Fire-side	X
5	Black deposit	a) Fire-side b) Reverse	W → X
6	Sinter	a) Red-brown b) Black	W → X
7	Hard black powdery	a) Throat-side b) Fire-side	Y
8	Hard black powdery	a) Fire-side b) Impeller-side	Z

TABLE 13 - Mineralogical analyses of deposits from Station 1

(Determinations carried out at Leeds University)

All values in wt%.

Deposit	1	2	3	4	5	6	7	8
Quartz	3.0	-	6.0	7.0	10.0	7.0	2.0	2.0
Cristobalite	-	Tr	Tr	-	-	Tr	-	-
Mullite	8.0	5.0	8.0	8.0	Tr	11.0	Tr	Tr
Anorthite	34.0	22.0	34.0	38.0	48.0	10.0	0.0	6.0
Hematite	3.0	5.0	5.0	2.0	7.0	4.0	40.0	55.0
Anhydrite	-	-	-	-	-	-	7.0	-
Total Crystalline	48.0	32.0	53.0	55.0	65.0	32.0	44.0	63.0
Glass - amorphous	51.1	68.4	47.9	44.6	35.4	68.9	51.2	37.4

TABLE 14 - Chemical analyses of deposits and coal ash from Station 1

Deposit determinations carried out at Leeds University. Coal ash analyses supplied by Babcock Power Ltd. All values in wt%.

Deposit	1	2	3	4	5	6	7	8	BS coal ashes (a)	BS coal ashes (b)
SiO_2	47.8	53.0	48.8	52.0	53.1	53.0	11.4	10.7	43.1	36.6
Al_2O_3	26.2	24.3	27.7	25.4	24.3	26.1	8.1	9.7	26.8	24.7
Fe_2O_3	4.7	5.3	5.7	3.9	7.1	4.2	67.5	71.3	4.0	9.1
FeO	1.5	0.6	1.3	2.5	0.7	1.8	0.2	0.6	-	-
CaO	12.1	9.9	10.7	10.0	9.7	9.3	4.2	3.5	11.6	12.0
MgO	3.2	3.7	2.5	2.3	2.1	2.4	1.9	1.7	3.2	3.1
TiO_2	1.3	1.2	1.4	1.1	1.3	1.2	1.4	1.4	1.5	1.4
Na_2O	0.5	0.5	0.5	0.5	0.3	0.5	0.3	0.2	0.6	0.65
K_2O	0.9	0.1	0.9	1.1	0.9	1.2	0.3	0.3	1.0	0.55
P_2O_5	0.8	0.8	1.0	0.6	0.7	0.9	0.5	0.4	1.4	1.8
SO_3	0.2	0.2	0.4	0.1	0.1	0.4	4.5	0.7	6.8	10.1

TABLE 15 - XRD powder analyses of deposits from Station 1

Deposit	Major phases	Minor phases
1a	An	Hem
1b	An	Hem
2a	An	Q, Mull, Her
2b	An	Hem, Q, Mull, C
2c	An	Q, Mull, Hem
3a	An	Q, Mull, Hem
3b	An	Q, Mull
4a	An	Q, Mull, Her, C
4b	An	Q, Mull, Her, C
4c	An	Q, C, Hem
5a	An	Q, C, Hem, Her
5b	An,Q	C, Hem, Her
6a	An	Q, Hem
6b	An	Q, C, Hem, Her
7a	Hem	Anh, Q
7b	Hem	Anh, Q, An
8a	Hem	Q
8b	Hem	Anh, Q

Key - An Anorthite, Anh Anhydrite, C Cristobalite
Hem Hematite, Mull Mullite
Q Quartz, Her Hercynite

Samples 1, 2 and 3 showed similar microstructural features with coral-like structures (Plates 13 and 14), which were more consolidated in places (Plate 15) presumably as a result of higher temperature or longer sintering times. The microstructure consisted of well-developed anorthite laths in a glassy matrix in which fine iron-rich crystals grew in places (Plates 16 and 17). The presence of fly-ash spheres on the outer surfaces of the deposits (Plate 18) implies that these deposits grew by the normal mechanism of fly-ash capture and sintering. The fact that the deposits remained very porous must be attributed to local temperature and atmosphere conditions.

Samples 4, 5 and 6 also showed similar microstructures, being dense and mostly highly crystalline. The surfaces of the deposits were coated in fly-ash which sintered in the normal way (Plate 19). Crystallisation occurred to give mainly anorthite, with lesser amounts of mullite, cristobalite and hercynite. Residual quartz was present where time, temperature and atmosphere conditions did not allow complete dissolution. Fracture surfaces were generally highly crystalline (Plate 20) with porosity varying according to position, i.e. temperature. However, in some cases, where the slag had obviously been molten in situ, a thin vitreous layer was observed on the outer or fire-side surface (Plate 21). The 'streamers' seen on the photograph of sample 4 (Plate 11) are typical. In many cases, aerodynamic shaping of the deposits due to the high local gas speeds produced streamered or vaned structures.

The iron-rich deposits, 7 and 8, showed a totally different microstructure. The throat deposit, sample 7, was uniform across the whole body. The structure consisted of large iron-rich particles which had a cellular surface skin and which were fairly porous, together with some fly-ash spheres and debris (Plate 22). Optical microscopy similarly showed porous highly reflecting (iron-rich) regions which appeared to have derived from the impact and consequent deformation and adherence of molten iron-rich spheres (Plate 23). The impeller deposit, sample 8,

PLATE 13 - Deposit 2 from Station 1 : Coral-like microstructure.

(White bar = 100μm)

PLATE 14 - Deposit 3 from Station 1 : More consolidated coral-like microstructure.

(White bar = 1000μm)

PLATE 15 - Deposit 3 from Station 1 : More consolidated coral-like microstructure. Smooth surfaces indicate rapid incorporation of fly-ash particles.

(White bar = 100μm)

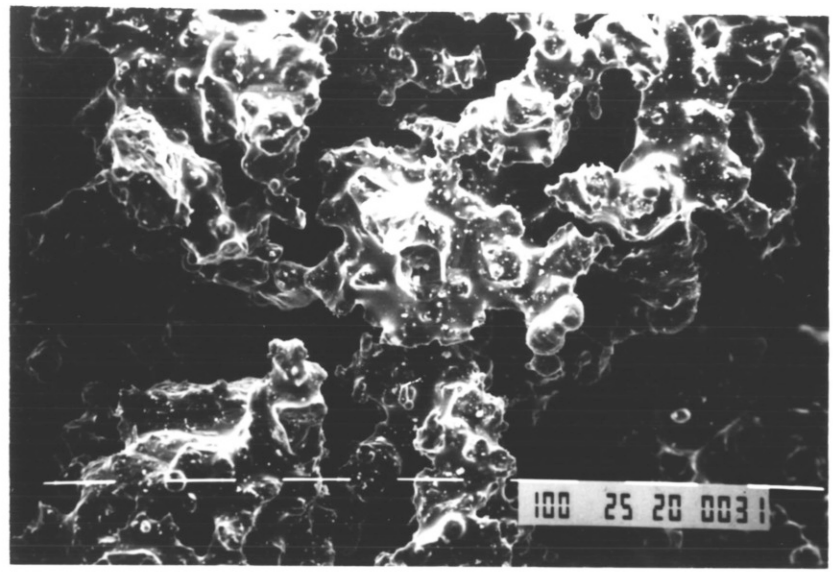

PLATE 13

PLATE 14

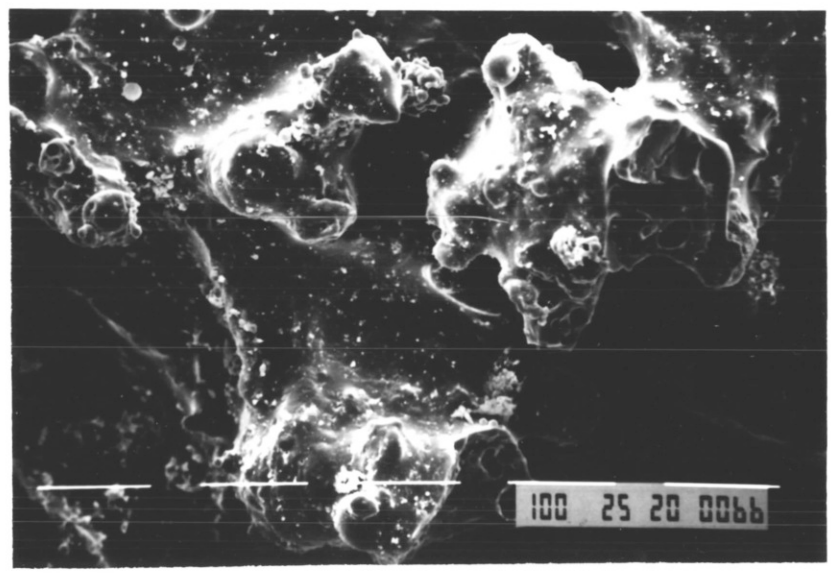

PLATE 15

PLATE 16 - Deposit 1 from Station 1 : Anorthite laths (dark grey) in matrix of glass and fine iron-rich crystals (bright).

(x125)

PLATE 17 - Deposit 1 from Station 1 : Highly crystalline fracture surface with anorthite laths visible.

(White bar = 100μm)

PLATE 18 - Deposit 2 from Station 1 : Newly deposited fly-ash spheres on fire-side surface.

(White bar = 100μm)

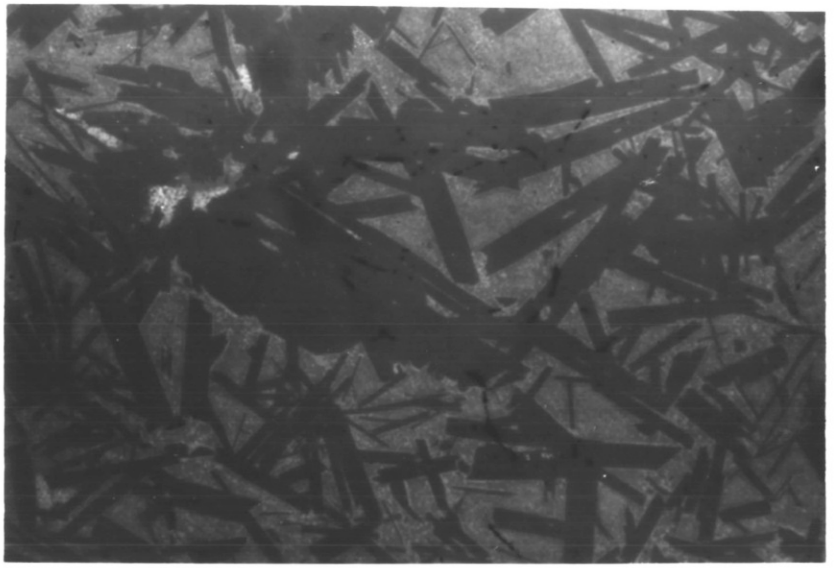

PLATE 16

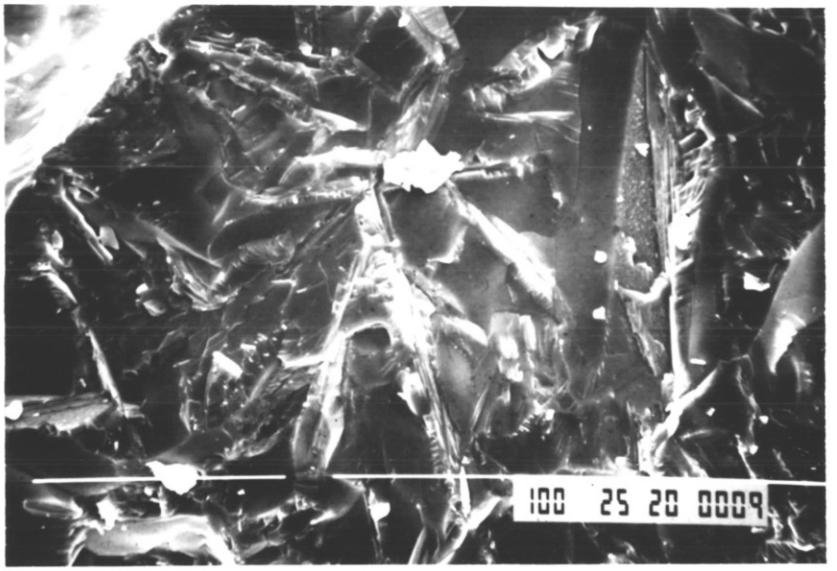

PLATE 17

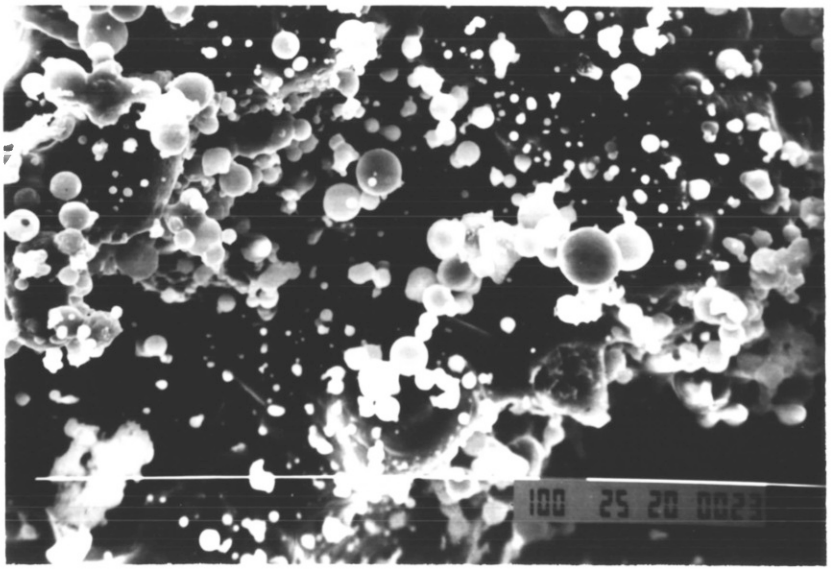

PLATE 18

PLATE 19 - Deposit 6 from Station 1 : Fly-ash spheres in the process of sintering. Neck growth is well advanced.

(White bar = 100μm)

PLATE 20 - Deposit 4 from Station 1 : Highly crystalline fracture and pore surfaces.

(White bar = 1000μm)

PLATE 21 - Deposit 4 from Station 1 : Glassy fracture and pore surfaces at the extreme fire-side.

(White bar = 100μm)

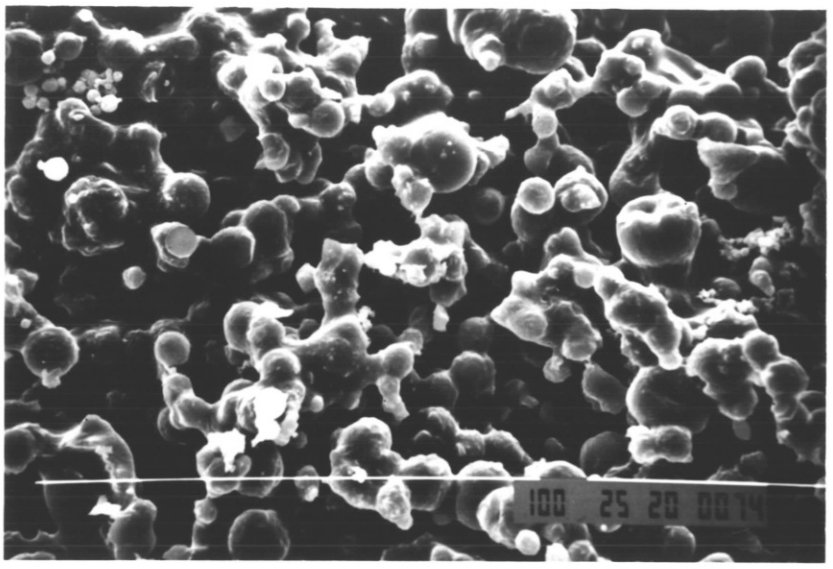

PLATE 19

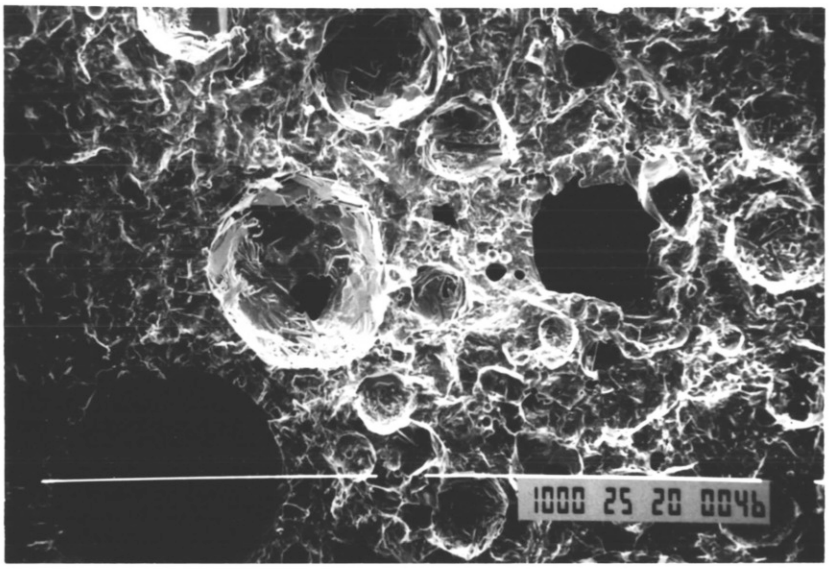

PLATE 20

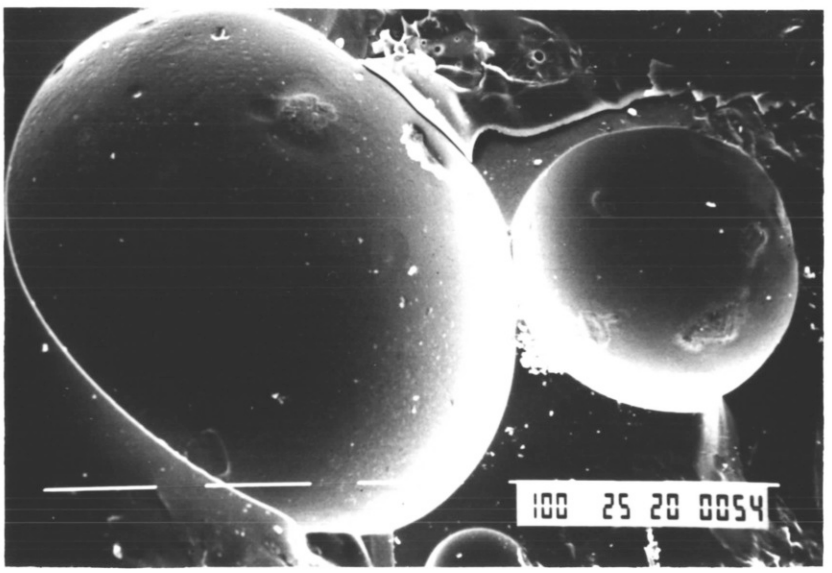

PLATE 21

PLATE 22 - Deposit 7 from Station 1 : Large iron-rich regions (top right and bottom left) with fly-ash particles in between.

(White bar = 10μm)

PLATE 23 - Deposit 7 from Station 1 : Ill-defined porous hematite (bright).

(x250)

PLATE 24 - Deposit 8 from Station 1 : Fire-side of deposit containing well-defined hematite (bright, tabular) in a matrix of glassy aluminosilicate and iron-rich dendrites (bright).

(x250)

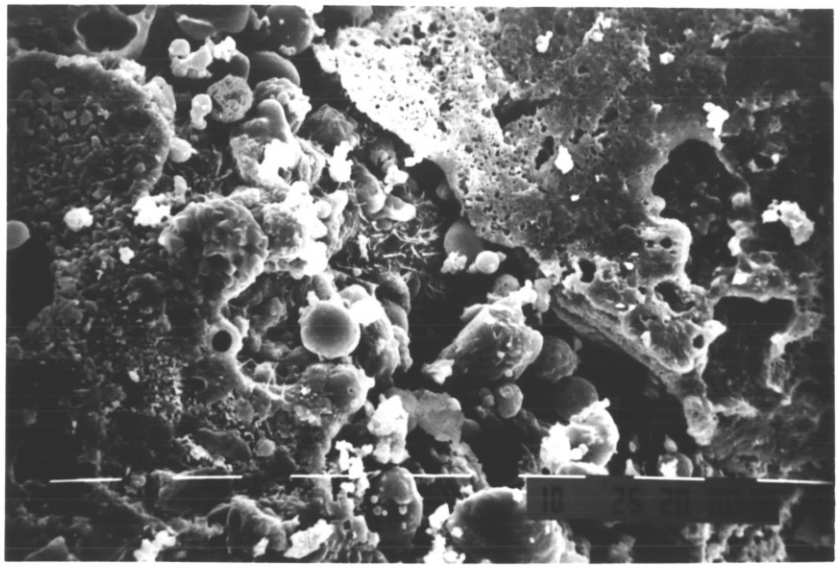

PLATE 22

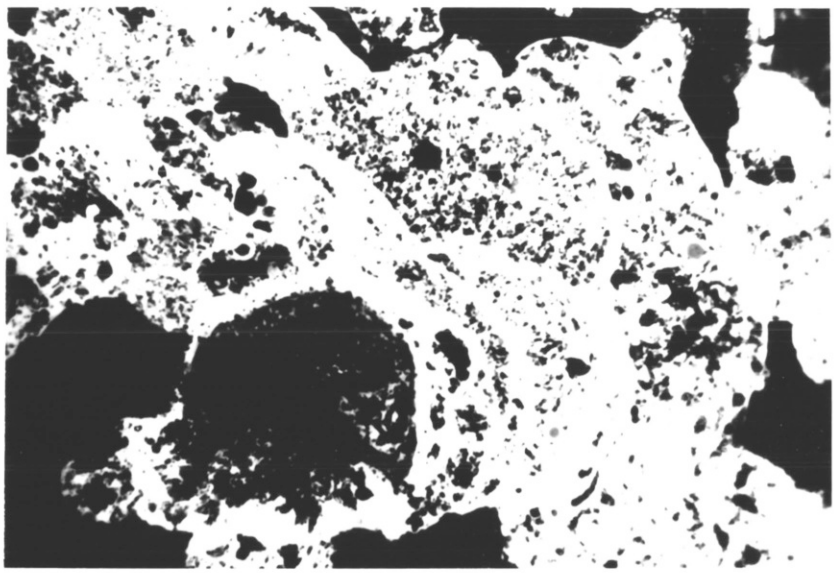

PLATE 23

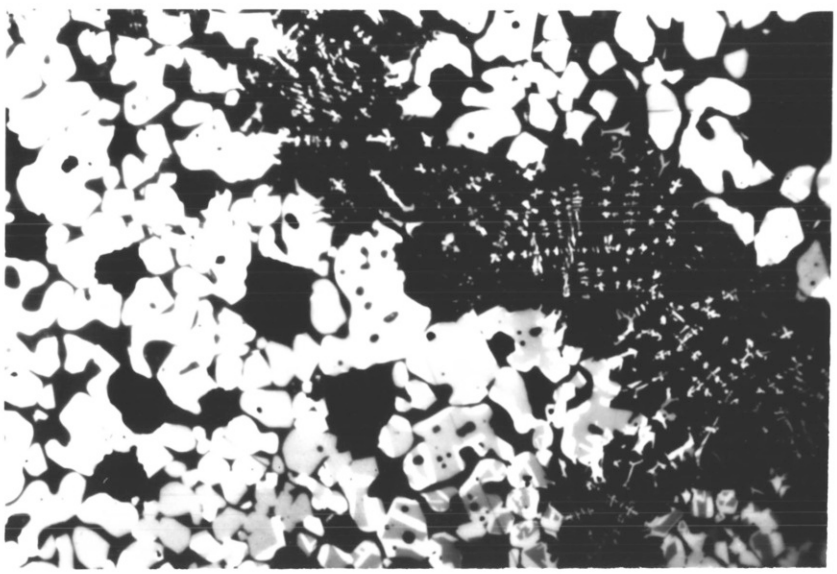

PLATE 24

shown in Plate 12, had a similar structure adjacent to the impeller surface. However, towards the fire-side surface there was a large amount of well-defined hematite. The high degree of definition suggests that the hematite crystals grew from a melt. The crystals were separated by a glassy phase, in which iron-rich dendrites grew in places (Plate 24).

EPMA was carried out on a section of the impeller deposit. Area analyses were made at 1mm intervals on an imaginary line perpendicular to the impeller surface. In this way, changes in chemical composition through the deposit were determined. The results are presented as Table 16. It is apparent that the outside surface (fireside) of the deposit contained more SiO_2 and Al_2O_3 than the inside (impeller surface), and consequently was lower in Fe_2O_3 content. The distribution of sulphur was not uniform. Spot analyses in the region 5-6mm from the outer surface showed that the sulphur was concentrated within the porous regions of the deformed, iron-rich spheres. Reporting sulphur as SO_3, EPMA reported up to 16wt% SO_3 in these regions. The bright, dense skins were found to contain <1wt% SO_3.

The second set of deposits was collected in late 1984 as a complete survey of every quarl in boiler 5. However, little attention was given as regards the exact location of each sample, and the extent of slagging, so these deposits are only of limited value.

Material taken from the quarl surfaces had chemical compositions similar to the corresponding coal ash. Microstructures observed were very similar to those of samples 1 to 6 from the first set of deposits.

The most interesting deposits came from the oil burner swirlers from a row of burners thought to have been idle during the boiler campaign. The oil burners are located in the central core of the p.f. burner, and are primarily used during boiler start-up. The swirlers provide turbulence for mixing the oil and combustion air.

TABLE 16 - EPMA of Station 1 impeller deposit

Area analyses of ∿1mm intervals from fire-side to impeller surface - all values in wt%.

	Fire-side											Impeller-side	
	0	1	2	3	4	5	6	7	8	9	10	11	12
	distance in mm												
SiO_2	12.86	17.32	8.92	9.28	4.21	3.87	3.51	7.40	6.01	6.61	7.63	6.77	3.65
Al_2O_3	8.04	6.64	4.77	5.45	2.59	1.85	2.28	3.74	3.28	4.89	4.79	4.68	2.45
Fe_2O_3	72.70	68.36	81.72	78.23	89.31	79.20	90.38	85.62	86.34	84.02	80.38	85.42	87.28
CaO	4.20	5.90	3.91	4.89	2.60	6.29	2.12	2.01	2.22	1.86	3.03	1.65	2.60
MgO	0.92	-	0.68	1.04	0.53	1.81	1.08	-	0.52	0.84	0.25	-	0.91
TiO_2	0.61	0.83	-	0.44	-	-	-	-	0.22	-	0.52	-	-
Na_2O	-	-	-	-	-	-	-	-	-	-	-	-	-
K_2O	-	0.34	-	0.18	-	-	-	-	-	0.15	0.22	0.24	0.15
P_2O_5	0.46	0.62	-	-	0.55	-	-	-	0.33	0.42	0.47	-	-
SO_3	-	-	-	-	0.21	6.98	0.63	1.24	1.07	1.21	2.71	1.23	2.87

The swirler deposits were found to be oil-sodden, with loss on ignition (24 hours at 800°C) being 70wt%. The non-carbonaceous residue was found to be of coal ash composition. This implies that the iron-rich throat and impeller deposits examined previously came from burners which were actually in use.

4.3.2 Station 2 (United Kingdom)

The deposits were collected from boiler 4 in August 1985, from the burner and quarl surfaces, and the tube-walls immediately adjacent to these. As with the Station 1 deposits, a wide range of structure was observed.

Several pieces of bottom hopper slag were analysed by EPMA. Together with the B.S. ash analysis of the fired coal, these analyses provide a reference composition for comparison of deposit compositions. Table 17 shows the chemical compositions of the ash and deposits.

The largest deposit came from the tube-wall, the tube impressions being clearly visible. This wall slag had a chemical composition similar to that of the coal ash and hopper slag. The major crystalline phase detected by XRD was mullite, with minor amounts of hercynite, hematite and quartz. The bulk of the deposit had a very crystalline, well-sintered microstructure (Plate 25), which became more porous towards the fire-side (Plate 26). The fire-side of the deposit consisted of a porous structure with less well-developed crystalline features and un-dissolved quartz (Plate 27). On the extreme fire-side, newly deposited fly-ash spheres were observed in the early stages of sintering (Plate 28).

The morphology of the hercynite spinel crystals was interesting. In the bulk, spectacular dendrites dominated, but towards the fire-side the morphology became much coarser, and even tabular in places (Plates 29 and 30). This is clearly a result of the increase in temperature of the

TABLE 17 - Chemical composition of deposits and coal ash from Station 2

	Coal ash *	Hopper ash	Wall slag	Quarl deposit	Iron-rich wall deposit	Air Swirler deposit
SiO_2	50.91	53.46	55.08	50.33	15.06	5.74
Al_2O_3	25.52	24.60	23.98	23.30	9.01	3.06
Fe_2O_3	12.92	11.94	11.64	15.46	63.40	60.56
CaO	1.90	2.11	1.63	2.92	2.27	1.10
MgO	1.14	1.83	1.50	2.32	1.64	0.75
TiO_2	0.89	0.92	0.95	0.85	0.29	0.07
Na_2O	1.17	1.15	1.00	1.53	1.35	0.76
K_2O	3.40	3.63	4.07	3.15	0.88	0.34
P_2O_5	0.31	0.27	0.09	0.15	0.17	0.16
SO_3	1.84	0.07	0.08	0.03	15.06	27.46

* Analysis supplied by Babcock Power Ltd.

PLATE 25 - Tube-wall deposit from Station 2 :
Mullite needles (mid-grey) and hercynite dendrites (bright) in a glassy matrix (dark grey).

(x250)

PLATE 26 - Tube-wall deposit from Station 2 :
Highly crystalline fracture and pore surfaces on fire-side of deposit.

(White bar = 100μm)

PLATE 27 - Tube-wall deposit from Station 2 :
Fire-side of deposit consisting of fine mullite needles (light grey) and hercynite (bright) with pores (black) and undissolved quartz (mid-grey, centre top).

(x125)

PLATE 25

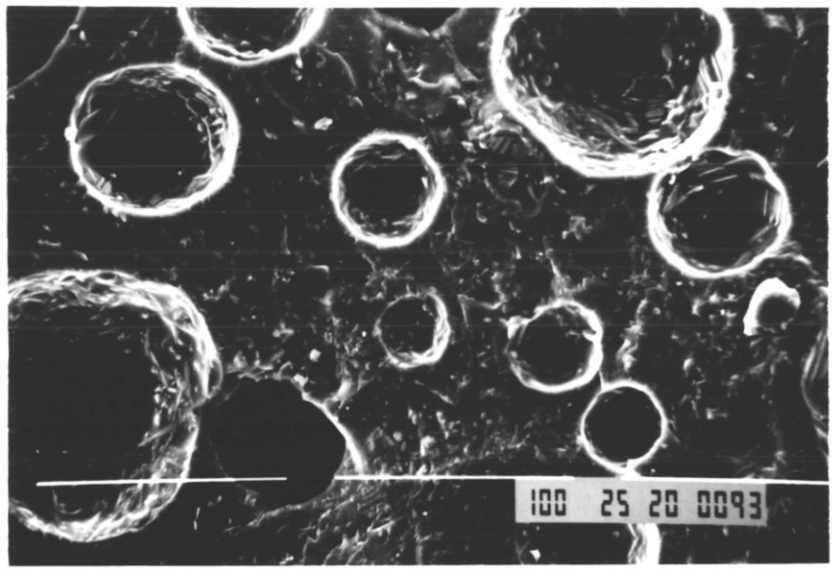

PLATE 26

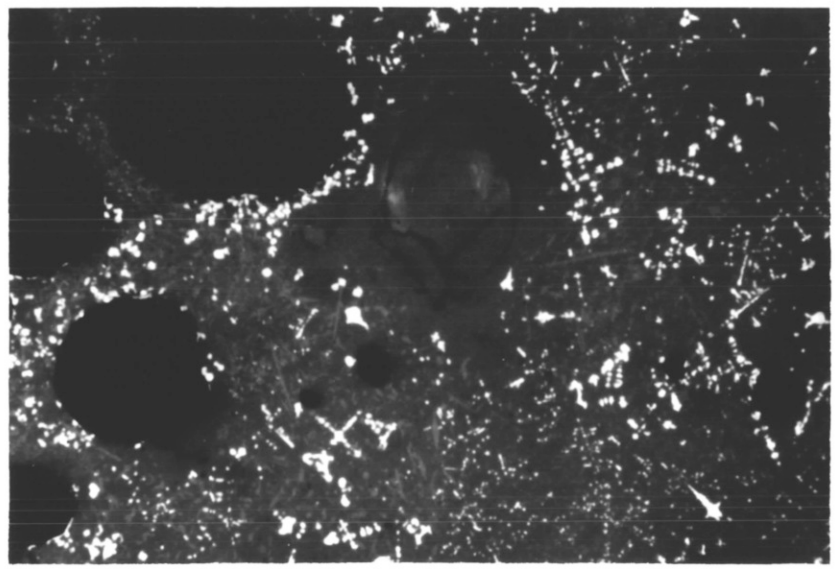

PLATE 27

PLATE 28 - Tube-wall deposit from Station 2 : Fly-ash spheres on the extreme fire-side, in the early stages of sintering.

(White bar = 10μm)

PLATE 29 - Tube-wall deposit from Station 2 : Fine mullite needles (light grey) and coarse dendritic hercynite (bright) in a glassy matrix (dark grey). Sample is porous (black).

(x250)

PLATE 30 - Tube-wall deposit from Station 2 : Fine mullite needles (light grey) and coarse tabular hercynite (bright) in a glassy matrix (dark grey). Sample is porous (black).

(x250)

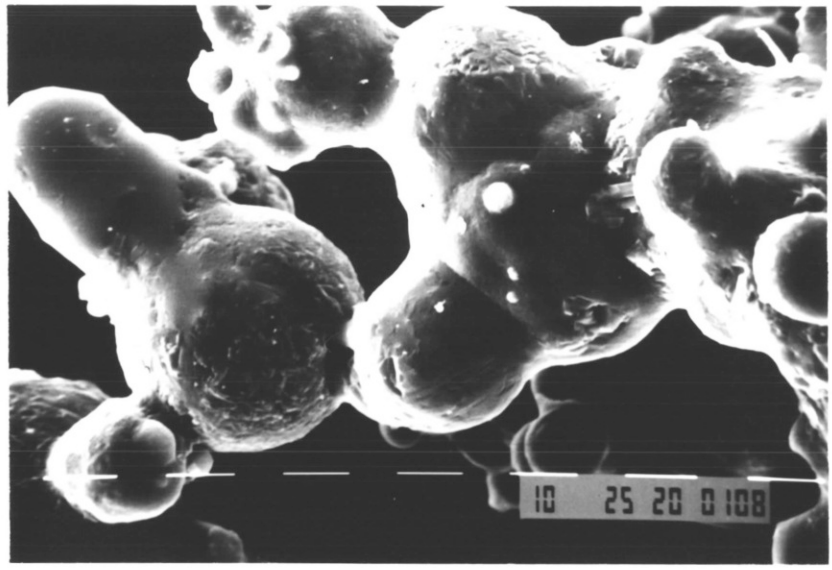

PLATE 28

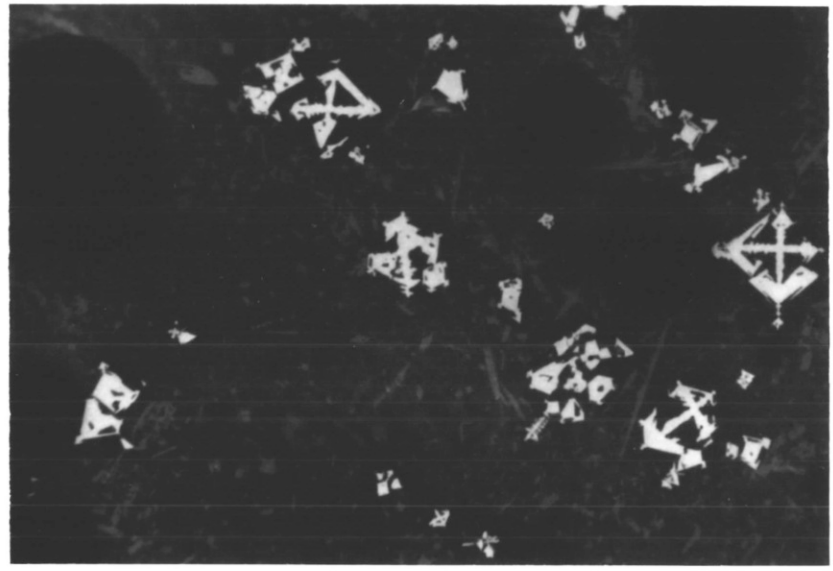

PLATE 29

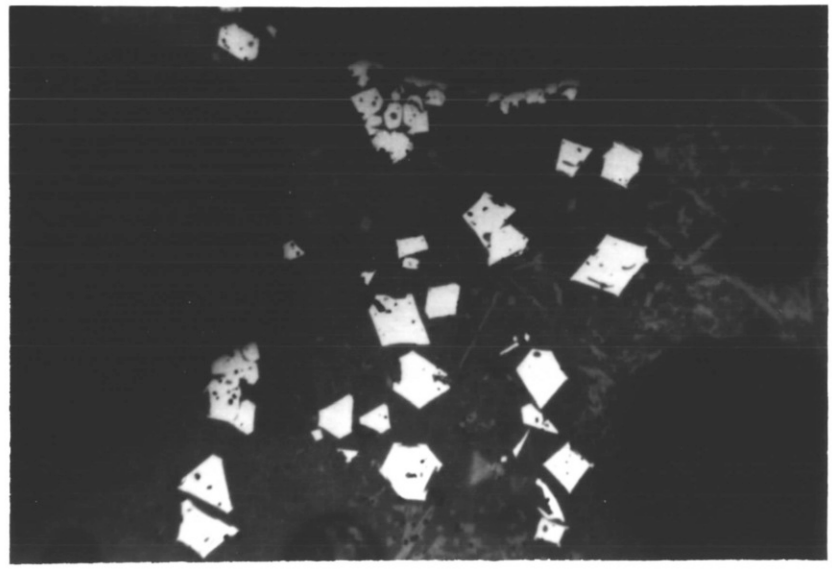

PLATE 30

slag surface as the deposit grew out into the furnace volume. According to Kirkpatrick, high temperature, i.e. lower undercooling, favours coarser growth morphology.[51]

Five samples of quart deposit were examined. As at Station 1 finned and vaned structures were common due to the high local gas speeds. Chemical compositions were similar to the coal ash (see Table 17). The major crystalline phase was mullite, with minor amounts of hercynite, hematite, quartz, anorthite and magnetite. Samples generally showed very crystalline microstructures with round pores, and undissolved quartz and pyrite residue (Plate 31). In places, mullite growth was seen to occur from a central nucleus and to fan out from this nucleus (Plate 32). The surfaces of many of the deposits were glassy (Plate 33), indicating high holding temperatures and fairly rapid cooling on burner shut-down.

Several small deposits were collected from the wall above the burner belt. These were found to have very high Fe_2O_3 contents (see Table 17), and microstructures indicating formation through the deposition of molten, iron-rich spheres (Plate 34). The major crystalline phase detected was hematite, with minor amounts of quartz, mullite, magnetite, anhydrite and anorthite. Spot analyses of the centres of iron-rich spheres showed high sulphur contents, reporting as between 20 and 45 wt% SO_3. The bulk sulphur level was $\sim$ 15 wt% SO_3.

Deposits were found on the core-air swirlers used with the oil burner located at the centre of the impeller. The six deposits examined showed very high levels of iron and sulphur (see Table 17). The major crystalline phase detected was pyrrhotite, with varying amounts of hematite, magnetite, and quartz. Two distinct iron-rich microstructures were observed. Close to the swirler surface porosity within individual spheres was high (Plate 35), but close to the outside of the deposits spheres remained dense (Plate 36). Spot analysis by EPMA found sulphur levels reporting as up to 42 wt% SO_3 in the dense spheres, with somewhat

PLATE 31 - Quarl deposit from Station 2 : Slag consisting of mullite needles and fine hercynite dendrites in glassy matrix, with round pores (black), and undissolved pyritic residue (bright, round) and quartz (dark grey, centre and top).

(x100)

PLATE 32 - Quarl deposit from Station 2 : Mullite needles (mid-grey) growing out from a central nucleus. Background consists of hercynite (bright) in a glassy matrix (dark grey).

(x200)

PLATE 33 - Quarl deposit from Station 2 : Glassy fracture and pore surfaces on extreme fire-side.

(White bar = 100μm)

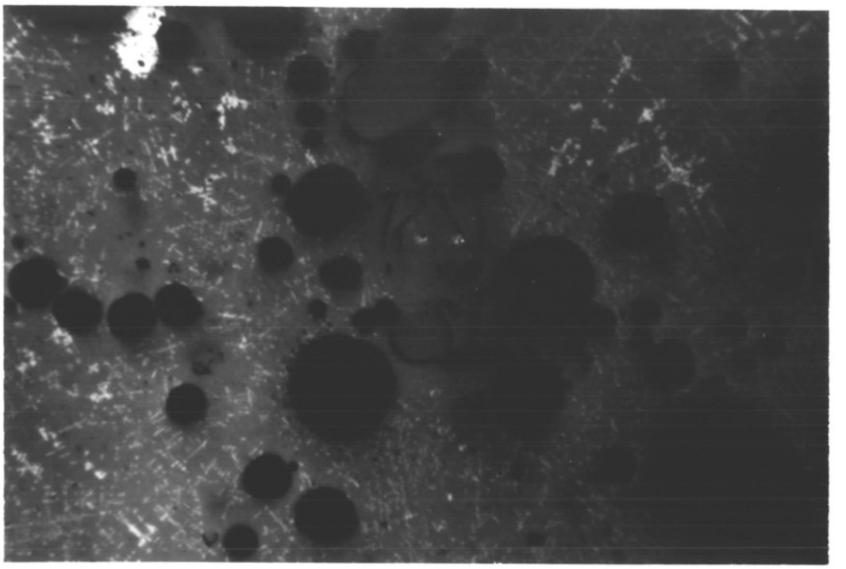

PLATE 31

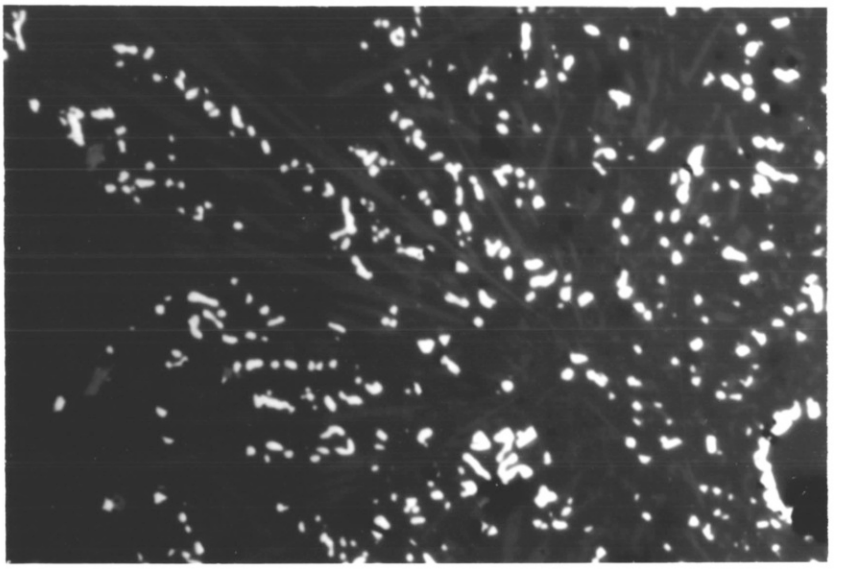

PLATE 32

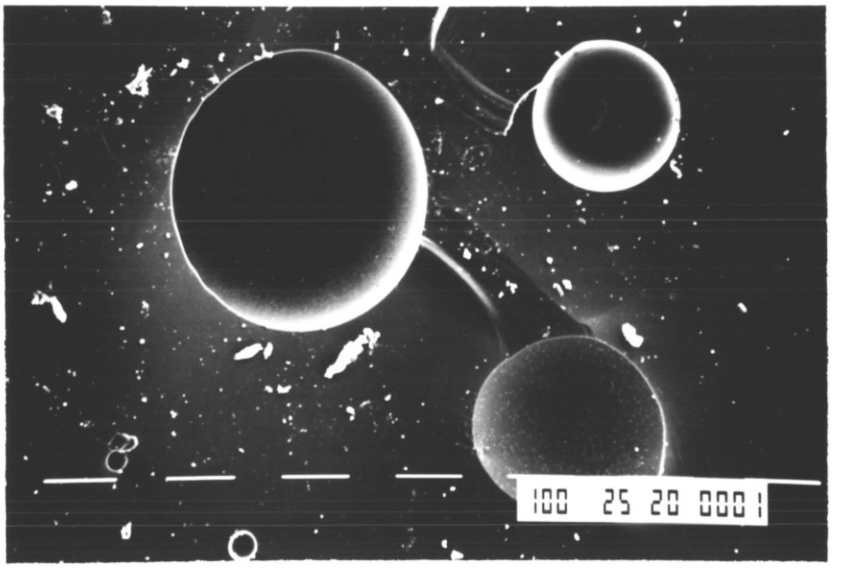

PLATE 33

PLATE 34 - Tube-wall deposit from Station 2 : Ill-defined hematite (bright) in the form of deformed spheres with solid surface skin and porous centre.

(x400)

PLATE 35 - Swirler deposit from Station 2 : Ill-defined hematite (bright) mostly in the form of deformed spheres with solid surface skin and porous centre.

(x400)

PLATE 36 - Swirler deposit from Station 2 : Pyrrhotite (grey) in the form of deformed spheres with little porosity.

(x400)

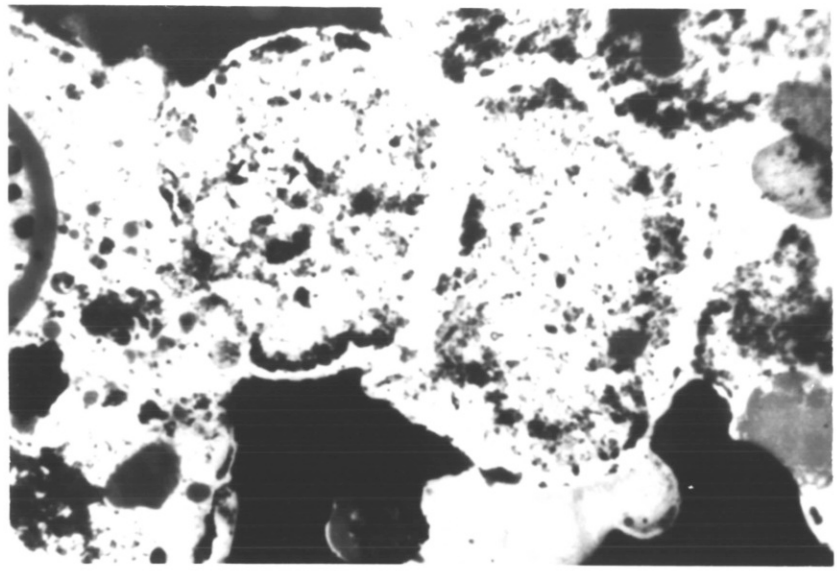

PLATE 34

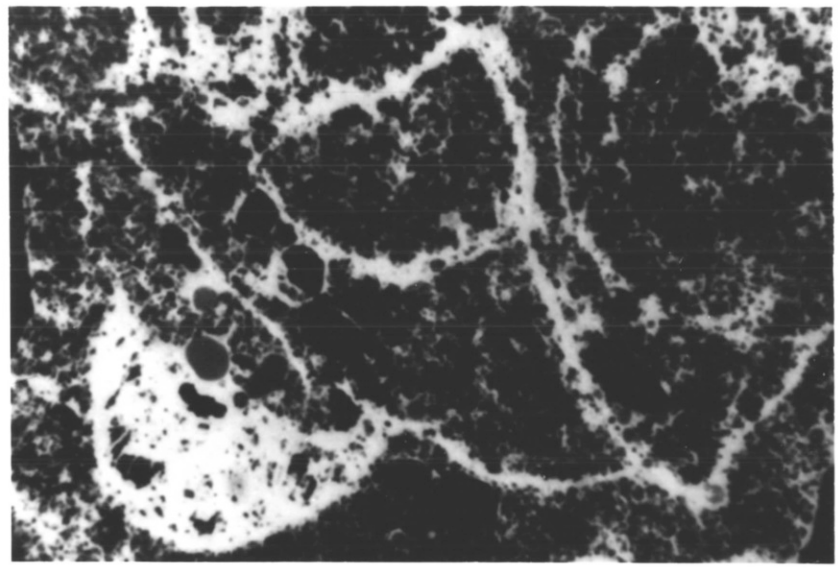

PLATE 35

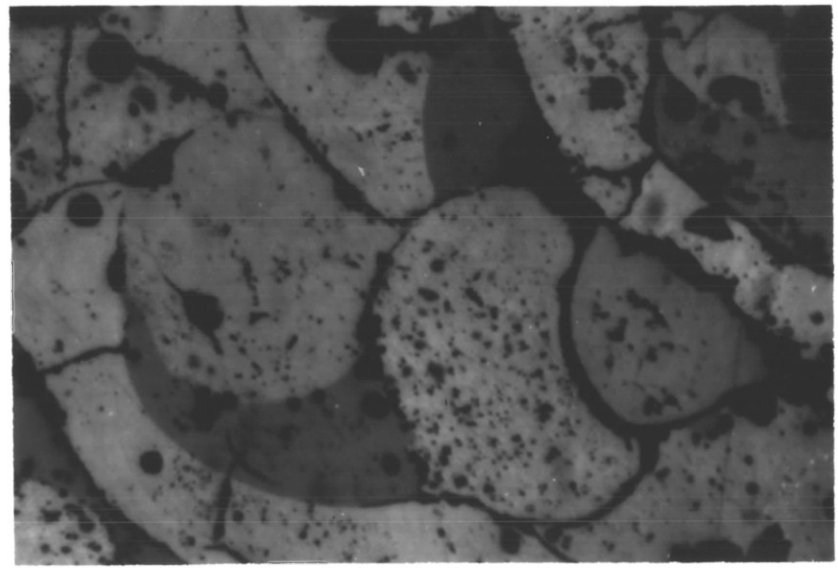

PLATE 36

lower levels in the porous spheres. These values must be compared with the 39.8 wt% SO_3 contained in the laboratory-prepared pyrrhotite used in section 4.2.

As with the Station 1 impeller deposits, several of the Station 2 core-air swirler deposits contained silicate-rich material on the fire-side. In fact, in one case, from the F6 burner, the chemical composition of the fire-side was almost identical to that of the coal ash. Figure 21 shows the changes in chemical composition through the deposit detected using EPMA of areas at 2mm intervals.

The variation in sulphur content is very interesting. Sulphur levels were low near the swirler surface and on the fire-side. Levels were highest at the edge of the iron-rich region nearest the fire-side.

4.3.3 Station 3 (United Kingdom)

The six samples were collected in July 1985 from the 39m level rear wall corner of one boiler. Figure 22 shows a schematic representation of a typical deposit, 2-3cm thick, showing the four regions identified microstructurally. It should be noted that only two samples contained all four of the structures, three consisting wholly of type 1, and one almost wholly of type 3. Table 18 shows the chemical compositions of the regions.

Iron-rich regions formed the tube-side of every deposit, and typically contained 50-65 wt% Fe_2O_3. The major crystalline phase detected was hematite, with traces of quartz, anorthite and mullite. The microstructure consisted of iron-rich spheres deformed on impacting a solid surface. (Plates 37 and 38)

The transition regions formed the boundary between the iron-rich and normal microstructures. The growth of hematite from the melt, and consequent crystallisation of the residual glass to anorthite and hercynite was observed in places (Plate 39).

FIGURE 21 - Chemical composition changes across a core-air swirler deposit from Station 2

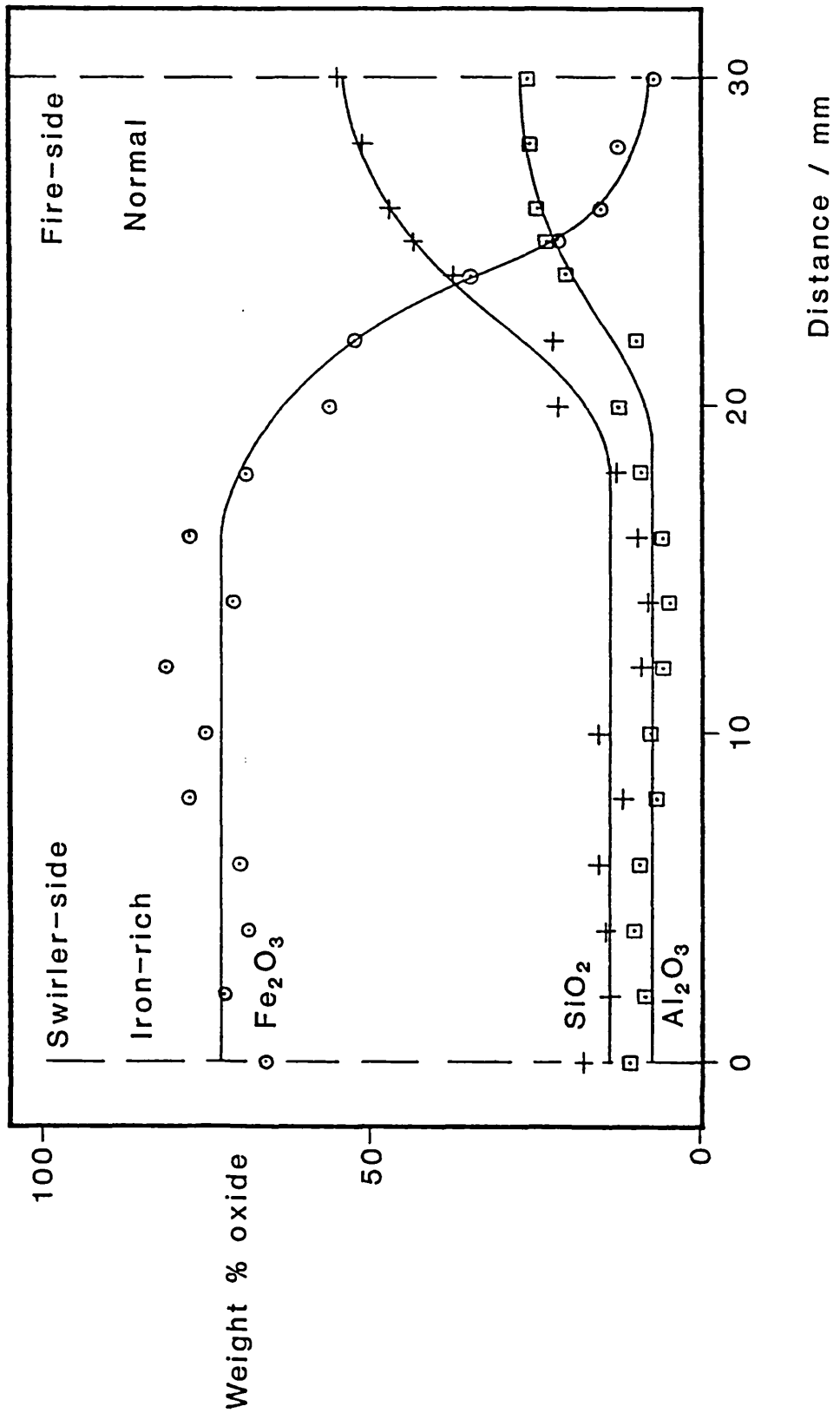

FIGURE 22 – Schematic representation of a typical wall deposit from Station 3

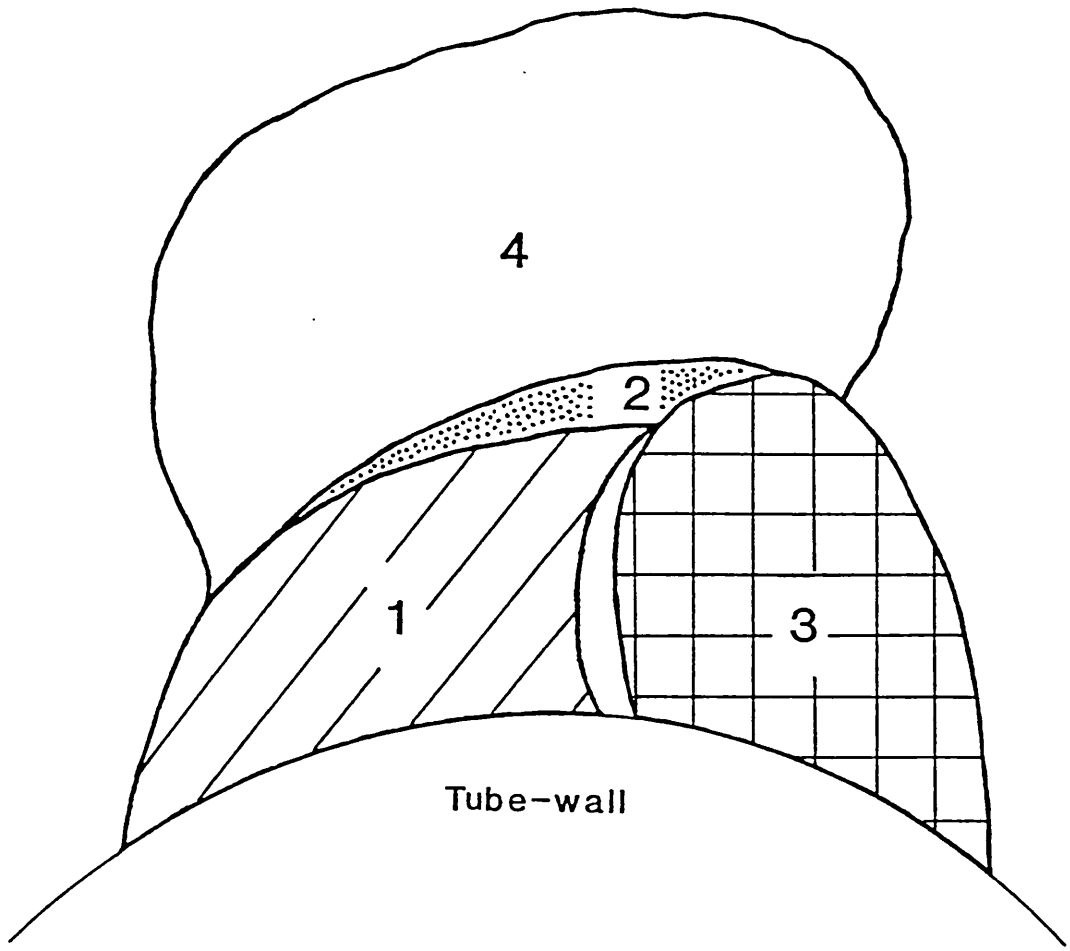

1 – Iron-rich region

2 – Transition region

3 – Black fused region

4 – Brown sintered region

TABLE 18 - Chemical composition of deposits from Station 3

All values in wt%

	Microstructural regions			
	1 (Iron-rich)	2 (Transition)	3 (Black, fused)	4 (Brown sinter)
SiO_2	13.98	37.94	51.01	49.57
Al_2O_3	7.62	16.56	25.17	22.16
Fe_2O_3	63.20	33.64	11.04	16.22
CaO	2.78	2.67	4.34	3.79
MgO	2.07	2.43	2.37	1.80
TiO_2	0.39	0.87	0.82	0.96
Na_2O	2.67	1.52	1.90	1.54
K_2O	0.80	1.62	2.93	2.87
P_2O_5	0.23	0.62	0.33	0.19
SO_3	6.23	1.83	0.16	0.91

PLATE 37 - Iron-rich region in Station 3 deposit : Ill-defined hematite (bright) in the form of deformed spheres with solid surface skin and porous centre.

(x250)

PLATE 38 - Iron-rich region in Station 3 deposit : Large iron-rich spheres, with aluminosilicate fly-ash spheres adhering to surface.

(White bar = 100μm)

PLATE 39 - Transition region in Station 3 deposit : Hematite crystals (bright) in a matrix of glass (dark grey) and anorthite laths (mid-grey).

(x125)

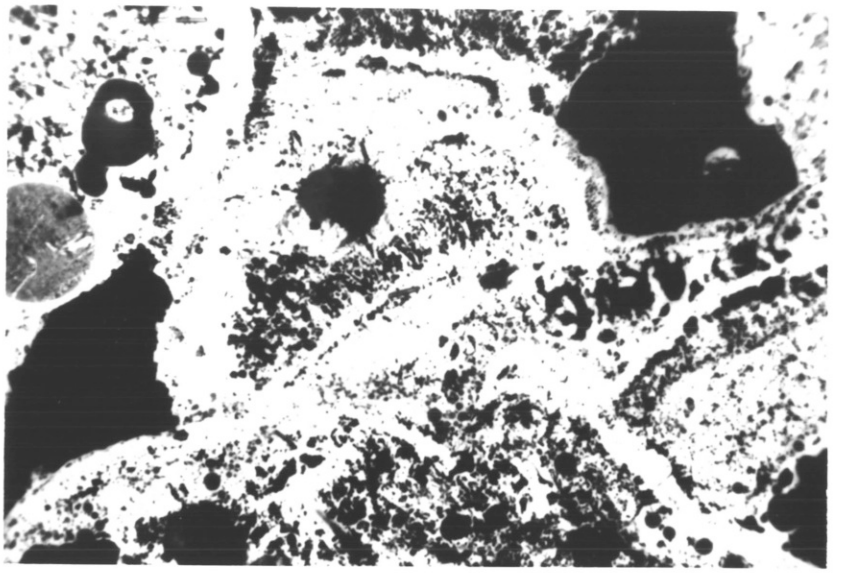

PLATE 37

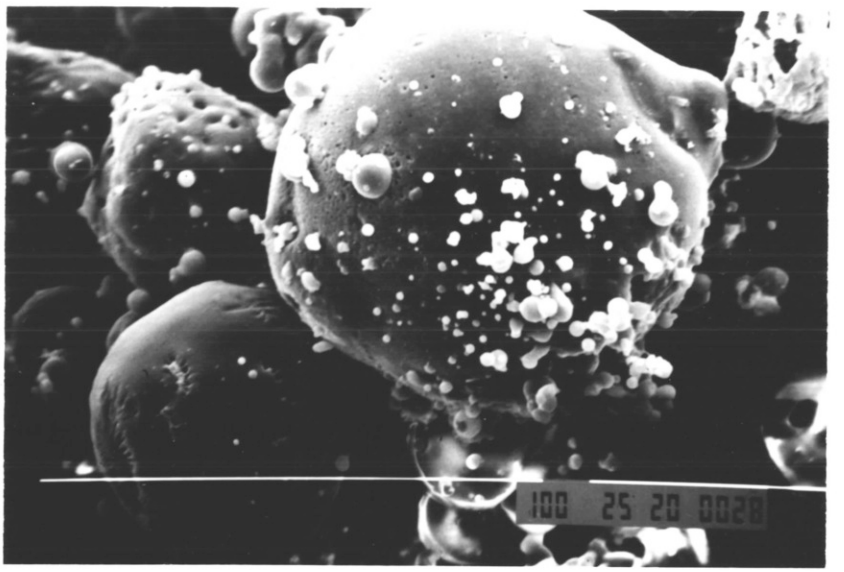

PLATE 38

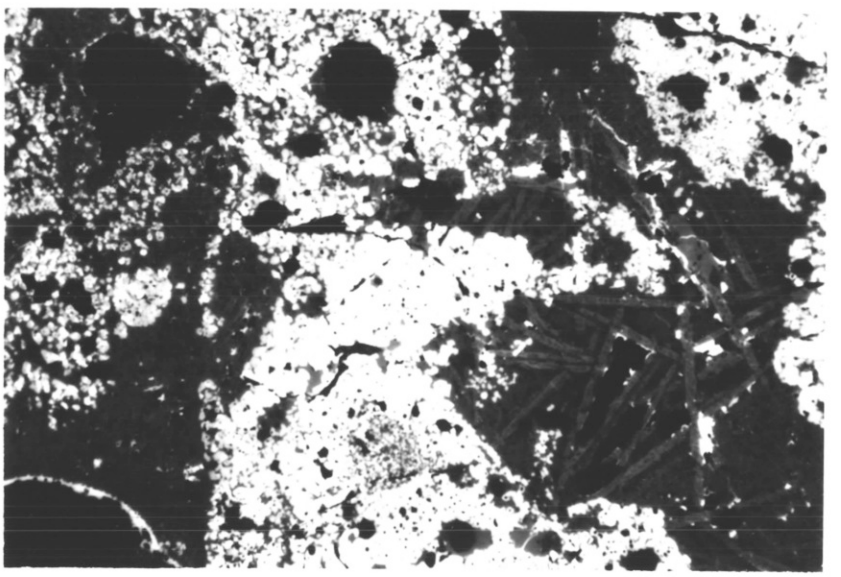

PLATE 39

The fused regions and sinter regions both had chemical compositions similar to the coal ash, but differed in porosity and crystal development. The fused areas were highly crystalline, with rounded porosity (Plates 40 and 41). The major crystalline phases present were anorthite and hercynite, with traces of quartz, mullite, magnetite and hematite. The sintered regions were poorly crystalline and very porous (Plate 42).

Detailed chemical analysis was carried out on one of the samples showing all four microstructures using EPMA of areas at 1mm intervals between tube-side and fire-side. Figure 23 shows the results of this analysis.

4.3.4 Station 4 (South Africa)

The fifteen samples examined were collected from boiler 3 in October 1984. Samples were taken from the front wall level with the bottom burner row (16m) and adjacent to a viewing port, and from the division wall, at the same level near to the front wall.

The front wall deposits (type A) were hard, light brown in colour and up to 15mm thick. The division wall deposits were of two types, the first of which (type B) was very similar to the front wall deposits. The second type (type C) consisted of a very light, friable 'honeycomb' structure, and was reported to be sitting on top of the first.

The chemical compositions of the deposits are shown in Table 19, together with a Station 1 coal ash composition - Station 4 and Station 1 are fed from the same coal field, and might therefore be expected to fire similar coals. Deposit types A and B were highly enriched in Fe_2O_3, while type C was of normal ash composition.

XRD analysis showed hematite to be the major crystalline phase in deposit types A and B, with smaller amounts of magnetite, gypsum, mullite, quartz and anhydrite also present. The major crystalline phases of type C were anorthite and quartz, with traces of mullite and hematite.

PLATE 40 - Fused region in Station 3 deposit :
Anorthite laths (mid-grey) in a matrix of glass
and fine hercynite crystals (bright).

(x250)

PLATE 41 - Fused region in Station 3 deposit :
Highly crystalline fracture and pore surfaces.

(White bar = 100μm)

PLATE 42 - Sintered region in Station 3 deposit :
Slag with poorly developed crystalline structure
and high porosity (black).

(x125)

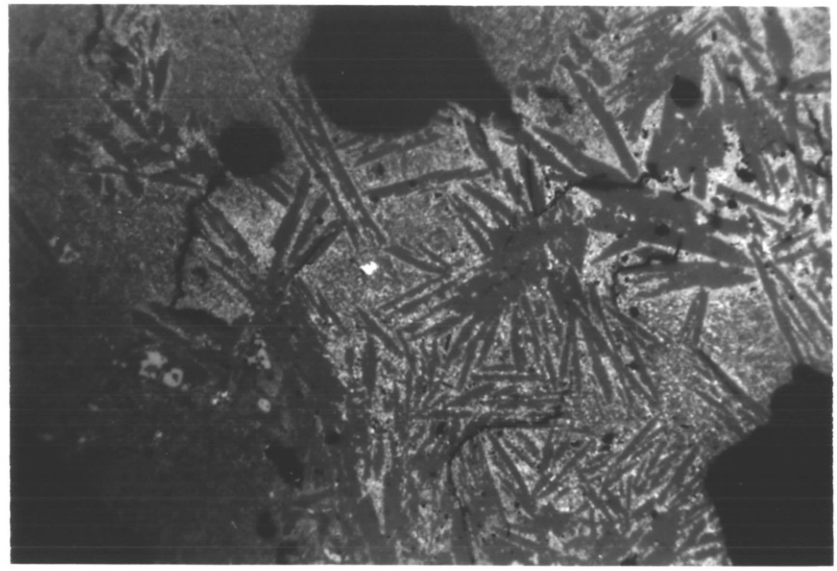

PLATE 40

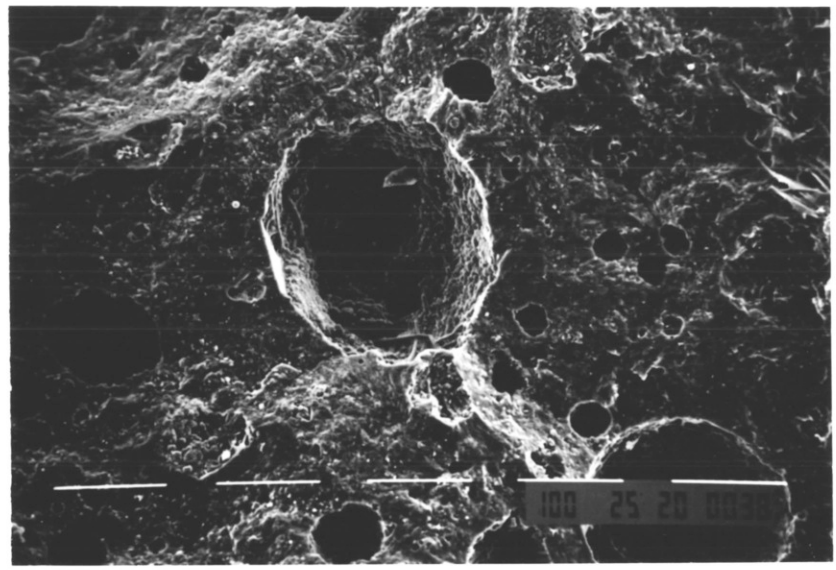

PLATE 41

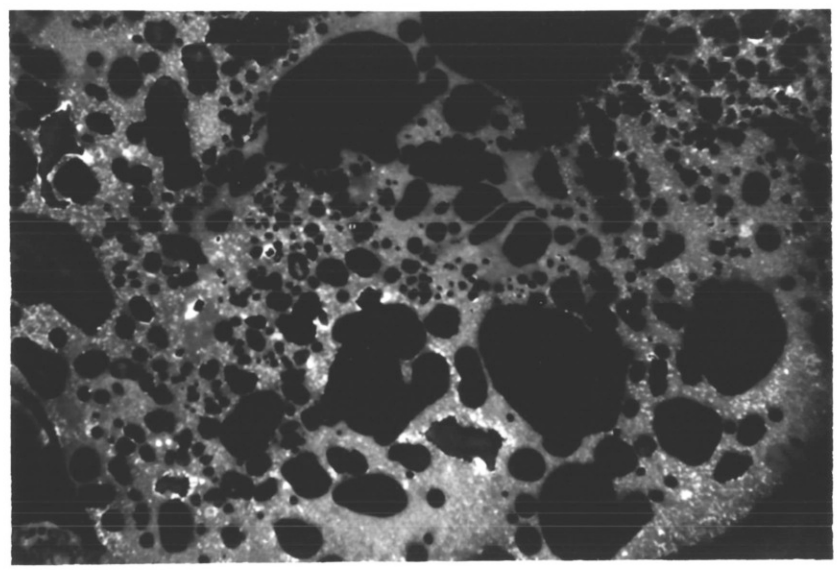

PLATE 42

FIGURE 23 - Chemical composition changes across typical wall deposit from Station 3

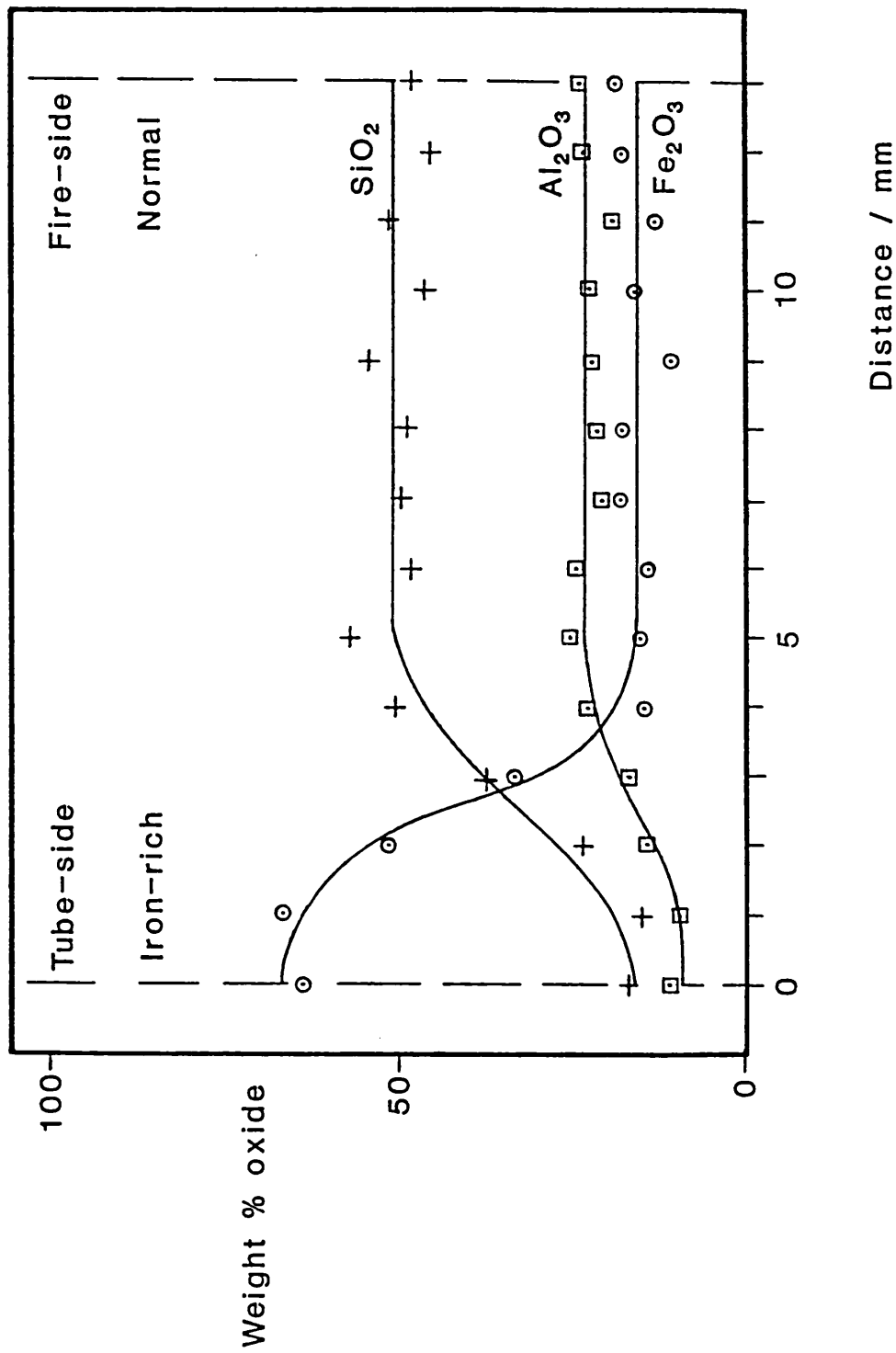

TABLE 19 - Chemical compositions of deposits and probable coal ash from Station 4

All values in wt%

	Deposit type			Station 1
	A	B	C	coal ash*
SiO_2	21.57	25.05	51.56	43.1
Al_2O_3	12.28	14.69	26.17	26.8
Fe_2O_3	55.67	49.51	4.50	4.0
CaO	7.61	7.00	11.22	11.6
MgO	1.01	1.22	2.66	3.2
TiO_2	0.87	1.18	1.72	1.5
Na_2O	0.26	0.37	0.56	0.6
K_2O	0.23	0.32	0.54	1.0
P_2O_5	0.40	0.51	0.85	1.4
SO_3	0.12	0.15	0.18	6.8

* Analysis supplied by Babcock Power Ltd.

The iron-rich microstructures consisted of large porous iron-rich spheres with fly-ash incorporated in between (Plates 43 and 44). The silicate-based 'honeycomb' structure was extremely porous, and only poorly crystalline, with residual quartz and pyritic residue (Plate 45). No transition microstructure was found in these deposits.

4.3.5 Station 5 (United Kingdom)

The deposits were collected in April 1986 from the ash hoppers. No deposit orientation was possible, though in several cases one side of a deposit had clearly been held at higher temperature than the other. The deposits are typical of those routinely analysed when a boiler is on-load. All samples were black and dense.

EPMA revealed little variation in chemical composition, as shown in Table 20 with no sample showing much deviation from the average. Mullite and anorthite were the major crystalline phases detected by XRD analysis, with minor amounts of quartz and hercynite.

The most striking feature of the microstructure was the variation in hercynite morphology, ranging from very fine dendrites to coarse skeletal crystals (Plates 46, 47 and 48). The observation of sintering fly-ash spheres on the external surfaces of the deposits suggests that these deposits formed in the normal way.

4.3.6 Station 6 (United Kingdom)

Two large pieces of slag from a stoker-fired unit were examined: one had been collected during normal operation and one while copper oxychloride was being added to the coal feed, at a dosage rate of 2-5 ppm of the coal. Both samples are believed to have been taken from the side walls of the furnace of the point where the slag overhangs the SiC refractory lining. Both samples were black and dense.

PLATE 43 - Type A deposit from Station 4 :
Large iron-rich spheres with fine aluminosilicate fly-ash spheres.

(White bar = 100μm)

PLATE 44 - Type A deposit from Station 4 :
Ill-defined porous hematite (bright).

(x200)

PLATE 45 - Type C deposit from Station 4 :
Anorthite laths (dark grey) in a matrix of glass and fine hercynite (light grey). Undissolved pyrite residue (bright, round) and quartz (grey, bottom right) are present. Porosity (dark grey-black) is rounded.

(x200)

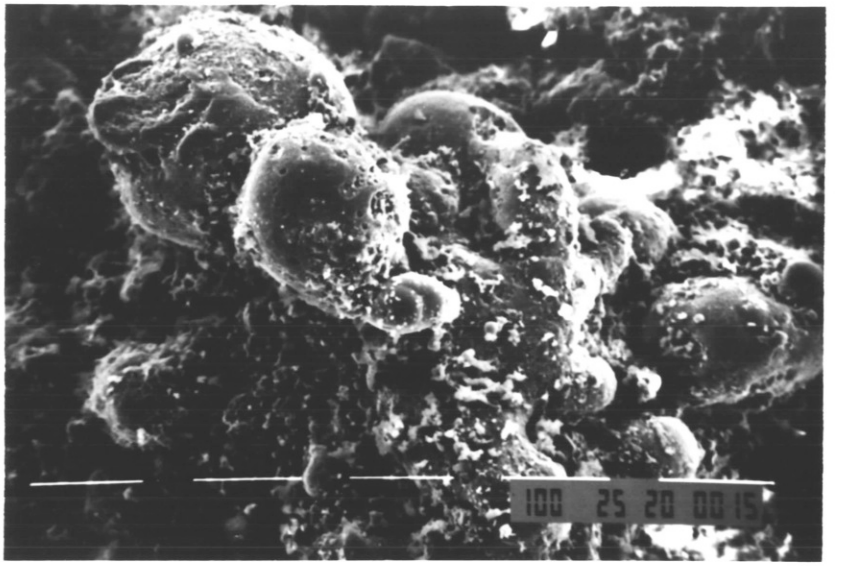

PLATE 43

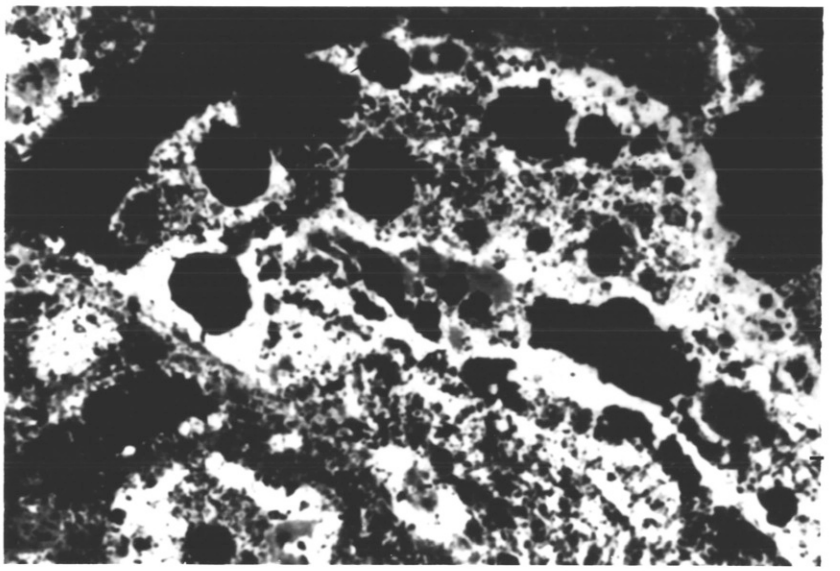

PLATE 44

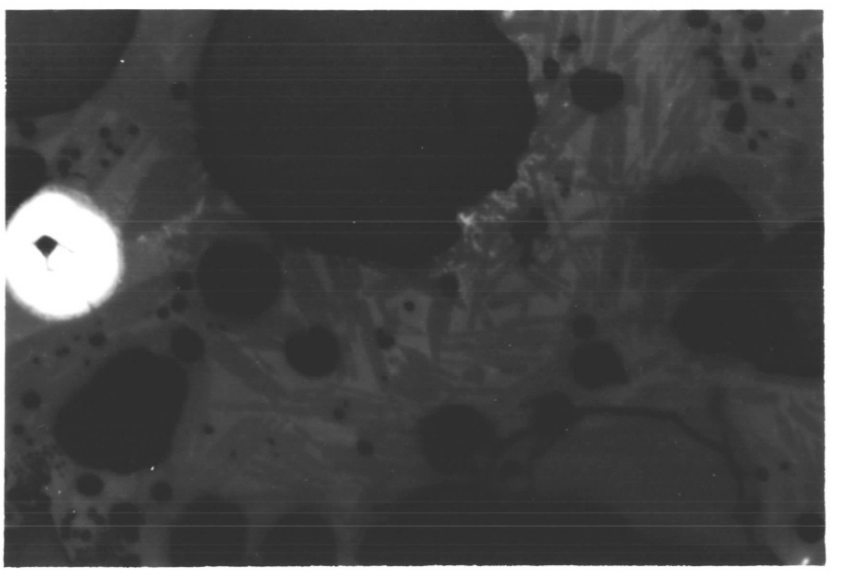

PLATE 45

TABLE 20 - Chemical compositions of Station 5 deposits

All values in wt%.

	Mean composition	Maximum detected	Minimum detected
SiO_2	51.87	55.05	49.33
Al_2O_3	23.67	25.91	22.70
Fe_2O_3	12.24	14.40	8.93
CaO	5.82	6.48	4.64
MgO	1.53	1.86	0.96
TiO_2	1.07	1.19	0.98
Na_2O	0.98	1.17	0.86
K_2O	2.28	2.65	2.01
P_2O_5	0.52	0.80	0.32
SO_3	0.04	0.08	0.01

PLATE 46 - Ash hopper deposit from Station 5 : Mullite needles (mid-grey) and fine hercynite dendrites (light grey) in a glassy matrix (dark grey).

(x400)

PLATE 47 - Ash hopper deposit from Station 5 : Mullite needles (mid-grey) and coarse hercynite dendrites (light grey) in a glassy matrix (dark grey).

(x400)

PLATE 48 - Ash hopper deposit from Station 5 : Mullite needles (mid-grey) and very coarse hercynite dendrites (light grey) in a glassy matrix (dark grey).

(x400)

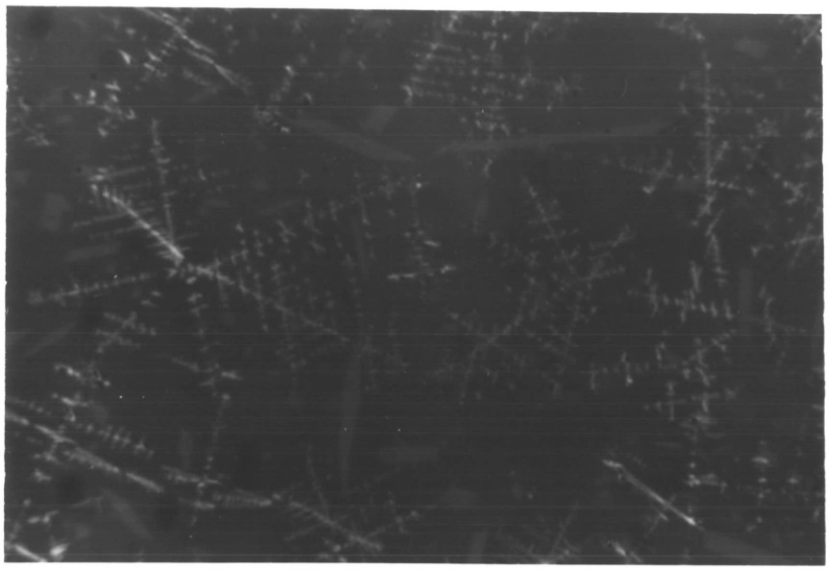

PLATE 46

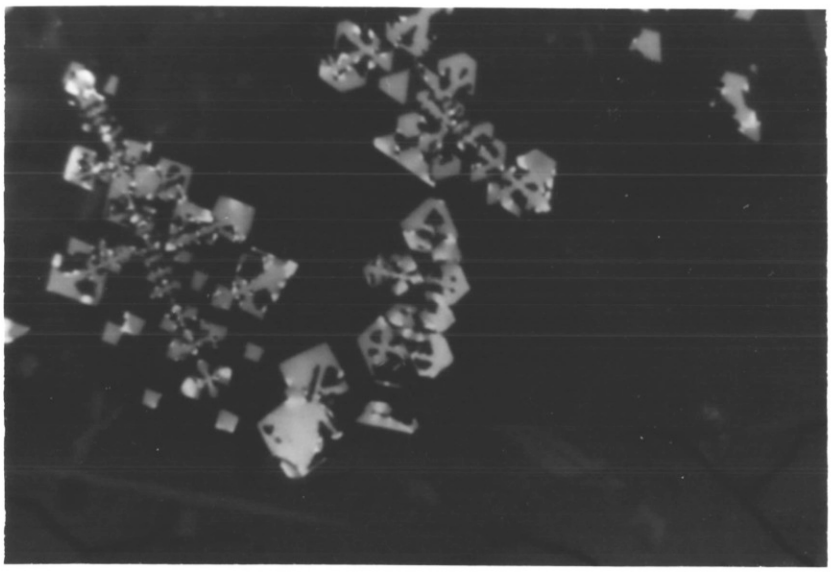

PLATE 47

PLATE 48

Table 21 shows that the chemical composition of the undosed slag was similar to the coal ash composition. The major crystalline phase was anorthite, with minor amounts of hematite and a hercynite-like spinel. The microstructure of the deposit varied across its thickness. The extreme fire-side was dense but poorly crystalline (Plate 49), suggesting that it had been held at a high temperature. Towards the middle of the sample, the porosity was similarly low but the crystallinity was much more developed, with anorthite laths and two tabular iron-rich phases, one very bright and one somewhat duller, together with fine iron-rich dendrites (Plate 50). The reverse-side of the deposit was coolest - the morphology of the hercynite-like spinel phase was more euhedral and the porosity higher (Plate 51).

The dosed sample was very similar to the undosed slag in terms of chemical composition and crystalline phases present. However, the microstructure showed a large amount of crystallisation of iron-rich phases around the pores especially on the fire-side of the sample. Again two types of iron-rich phase were present, one bright and one dull. In many cases, the pores had subsequently been filled by the flow of silicate material (Plate 52 and 53). In the bulk the iron-rich phases were tabular (Plate 54). Towards the reverse-side of the sample, the morphology became more dendritic (Plate 55) and porosity was much higher.

A major feature of the microstructure of these deposits was the distinct two-tone reflectivity of the iron-rich recrystallised phases. In all the previously described deposits a single-tone hercynite spinel was observed and hematite was not present as a recrystallisation product. Table 22 shows the chemical composition of the iron-rich recrystallisation products in the dosed Station 6 slag. The compositions show the bright phase to be a hematite solid solution, and the darker phases to be spinel solid solutions differing in iron oxide content.

TABLE 21 - Chemical compositions of coal ash and slags from Station 6

All values in wt%

	Coal ash*	Undosed slag	Dosed slag
SiO_2	46.2	50.37	52.58
Al_2O_3	25.8	22.93	22.58
CaO	4.7	7.72	6.34
Fe_2O_3	16.2	13.39	12.99
Na_2O	0.4	0.14	0.17
K_2O	3.0	2.27	2.07
MgO	2.3	2.14	2.05
TiO_2	0.9	0.94	0.88
P_2O_5	0.4	0.07	0.24
SO_3	0.1	0.04	0.12

* Analysis supplied by Babcock Power Ltd.

PLATE 49 - Undosed deposit from Station 6 : Fire-side of deposit containing anorthite laths (dark grey) and tabular hercynite (bright) in a glassy matrix.

(x250)

PLATE 50 - Undosed deposit from Station 6 : Middle of deposit containing tabular two-tone iron-rich phases with background of anorthite laths (dark grey) in a matrix of glass and fine hercynite (mid-grey).

(x250)

PLATE 51 - Undosed deposit from Station 6 : Reverse of deposit containing two-tone iron-rich phases (bright), pores (black) and anorthite laths (light grey) in a glassy matrix.

(x125)

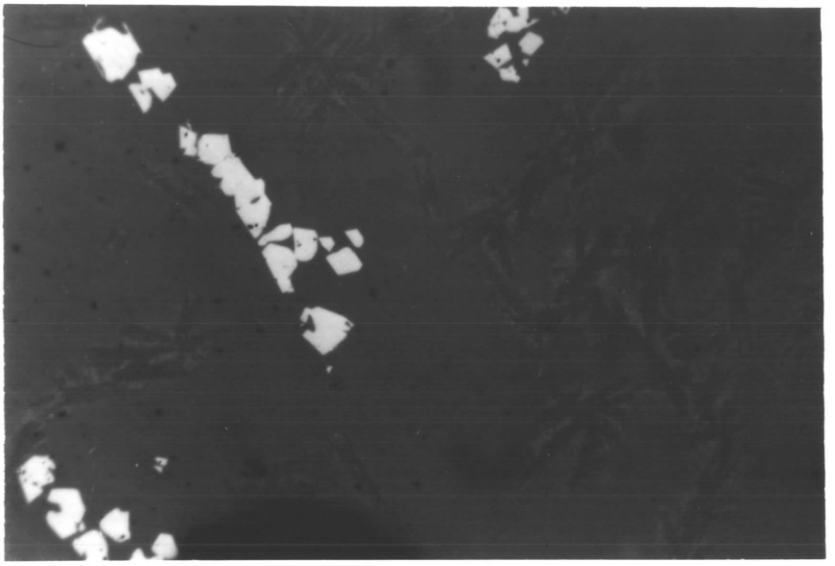

PLATE 49

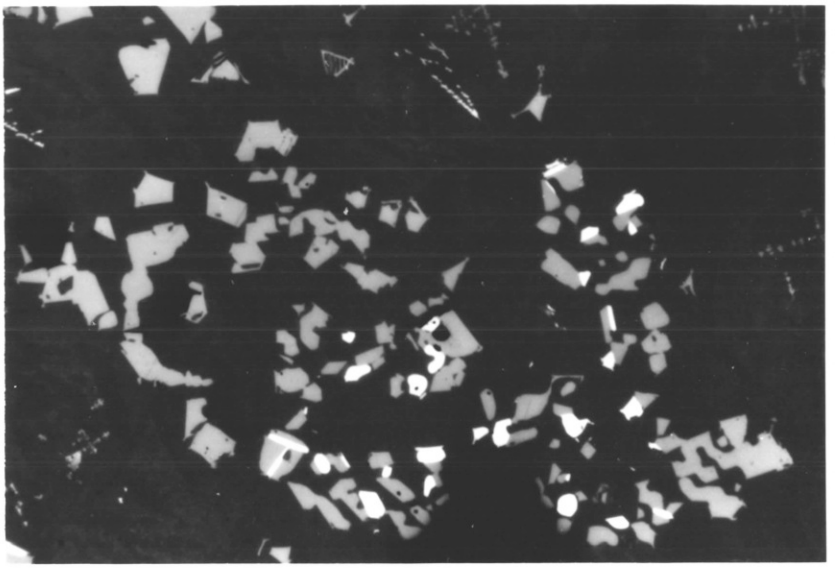

PLATE 50

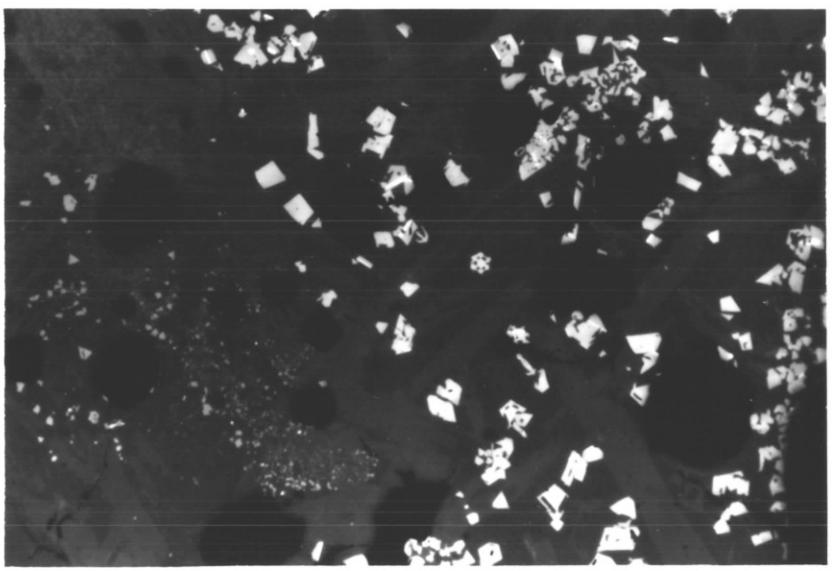

PLATE 51

PLATE 52 - Dosed deposit from Station 6 : Crystallisation of iron-rich phases (bright) around pore which was subsequently filled with aluminosilicate slag (greys).

(x125)

PLATE 53 - Dosed deposit from Station 6 : Detail of Plate 52 showing two-tone nature of crystallisation, with bright hematite and darker spinel.

(x250)

PLATE 54 - Dosed deposit from Station 6 : Bulk of deposit containing tabular two-tone iron-rich phases in a matrix of glass (dark-grey) and anorthite laths (light grey).

(x250)

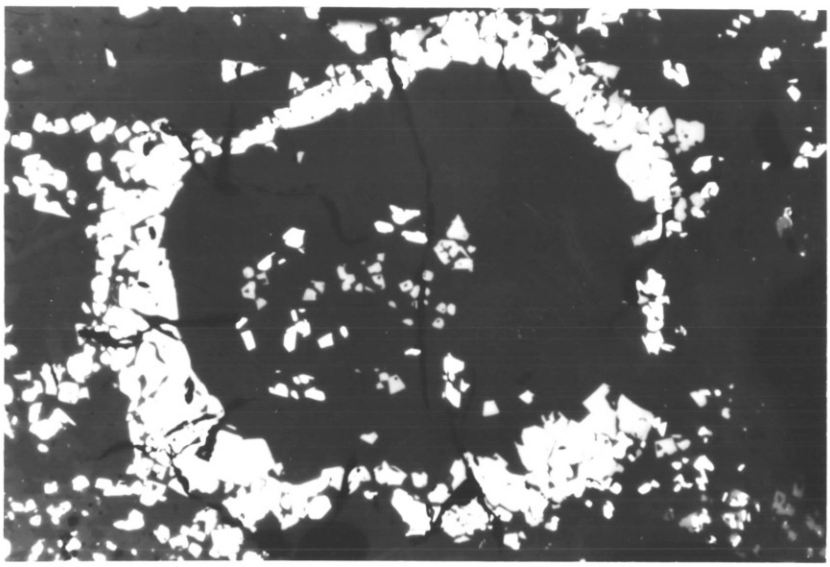

PLATE 52

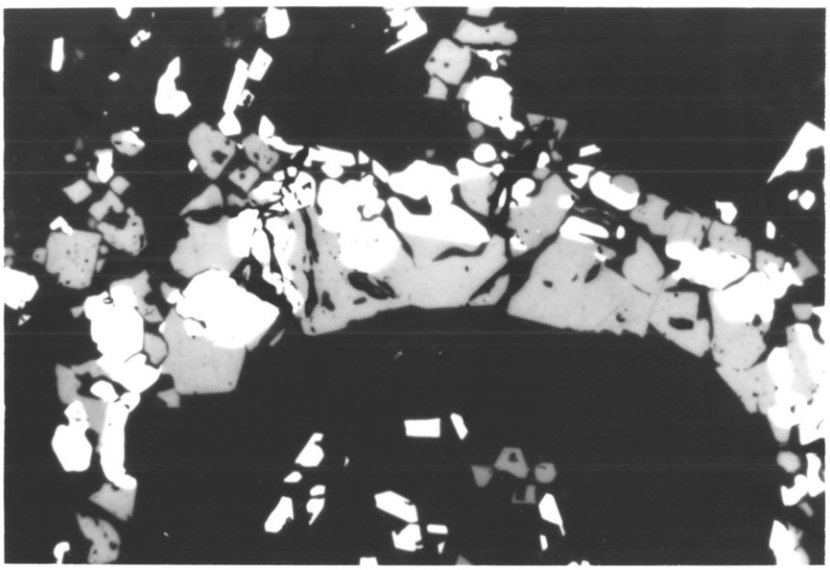

PLATE 53

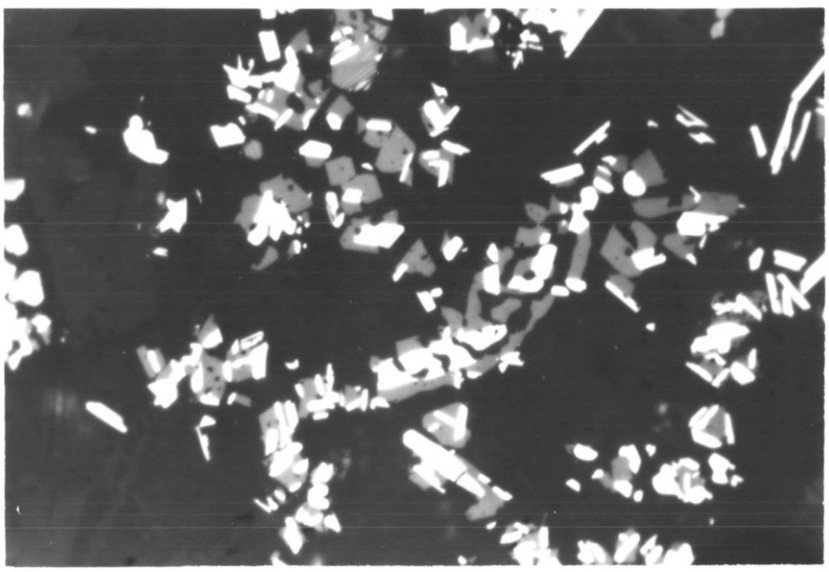

PLATE 54

PLATE 55 - Dosed deposit from Station 6 : Dendritic spinel (bright) and anorthite laths (light grey) in a glassy matrix.

(x250)

PLATE 56 - Heat-treated dosed deposit ($800^{o}C$, air) : Exsolution of hematite (white) from spinel (light grey) at surface of sample.

(x250)

PLATE 57 - Heat-treated dosed deposit ($1100^{o}C$, air) : Coarser exsolution at a higher temperature. Pore is just out of shot on the bottom right-hand corner.

(x250)

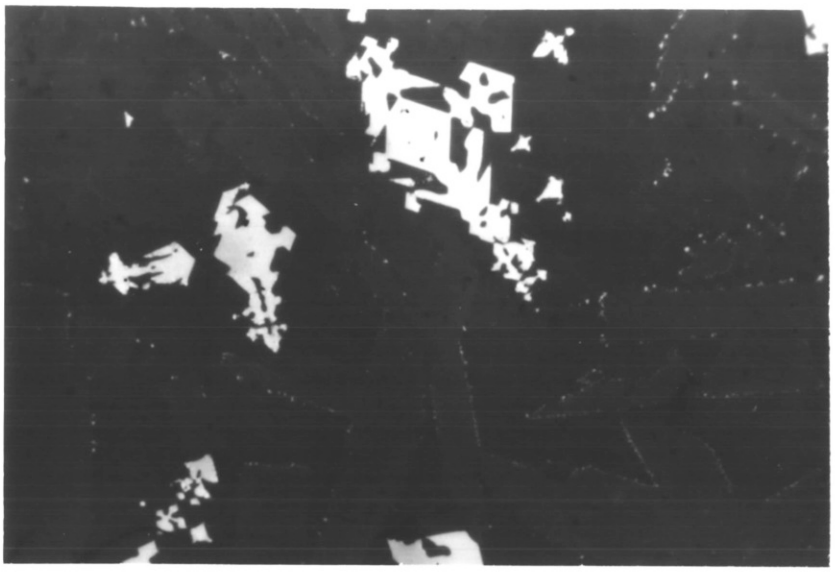

PLATE 55

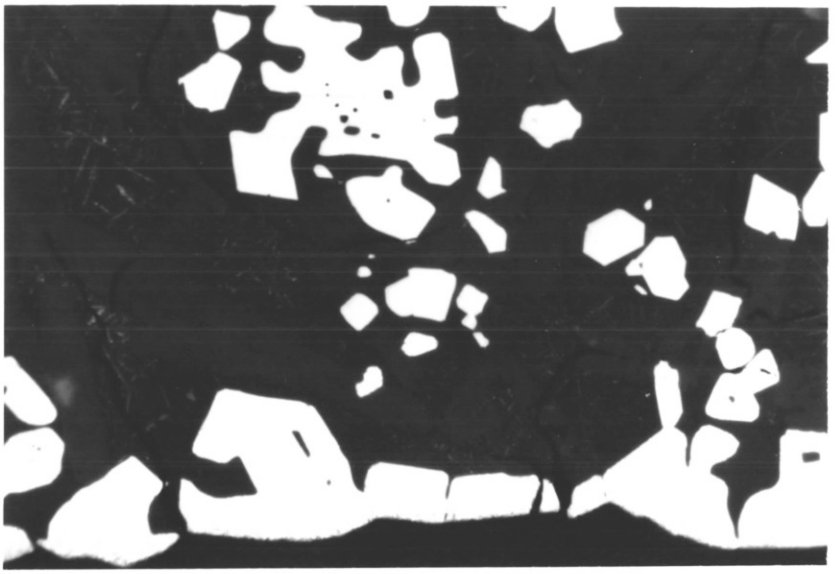

PLATE 56

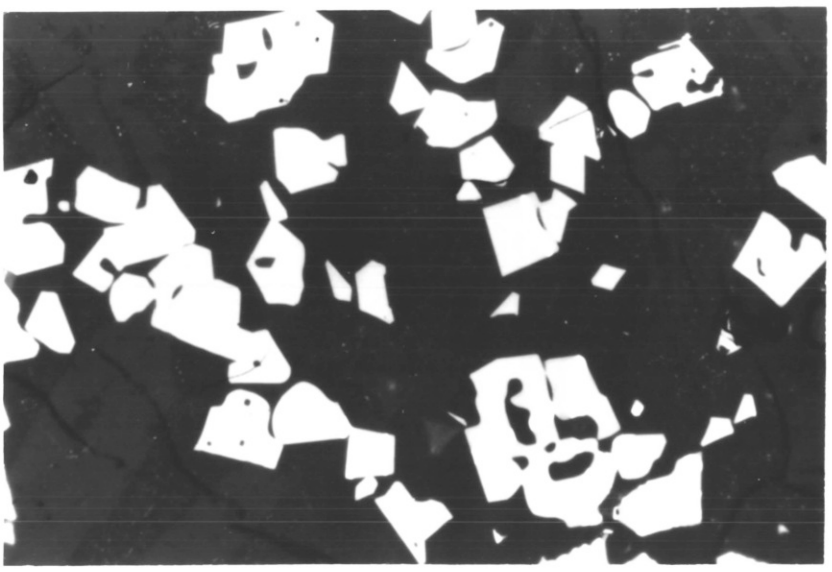

PLATE 57

TABLE 22 - Chemical composition of iron-rich phases in a COC-dosed slag from Station 6

Compositions normalised to $Fe_2O_3 + Al_2O_3 + MgO + TiO_2 = 100$ wt%.

	Dendritic phase as received - single tone	Tabular phases as received bright	Tabular phases as received dark	Dendritic phase heat-treated* bright	Dendritic phase heat-treated* dark
Fe_2O_3	66.73	85.01	61.78	88.85	60.59
Al_2O_3	23.46	5.98	26.10	6.13	24.86
MgO	8.37	1.84	11.87	1.51	14.32
TiO_2	1.44	7.17	0.87	3.50	0.24
Crystalline phase	Spinel SS	hem SS	Spinel SS	hem SS	Spinel SS

* Heat-treatment - 5 hours at 1200°C in air.

In order to investigate these features further small (∿ 1cm cube) samples were cut from the reverse of the dosed sample, taking material which contained only a single spinel phase. These samples were heated in air for 5 hours at temperatures from 600°C to 1300°C. Treatment up to 1200°C induced transitions to give two-tone reflectivity, but only in a thin layer on the external surface of the sample (Plate 56); the separation becoming coarser at higher temperatures (Plate 57). At 1300°C, separation was observed throughout the sample, with the sample flowing during treatment. EPMA showed that the chemical compositions of the separated bright and dull phases were almost identical to those found in the boiler samples (see Table 22).

These observations suggested that the phenomenon occurred as a result of an oxidation process. The Widmanstätten structure of the exsolution of hematite from an iron spinel heat-treated in air has been reported by Carter et al.[113] Therefore, heat-treatment was carried out at 915°C and 1025°C in both argon and oxygen atmospheres. Argon produced very much less surface separation, while separation in the bulk occurred in an oxygen atmosphere, again being coarser at the higher temperature (Plates 58 and 59).

XRD analysis of representative samples was used to compare the effect of atmosphere on samples treated at 1020 ± 10°C. Table 23 shows the measured heights of the strongest peaks of the phases present. The ratio of hematite:hercynite was seen to increase with oxygen partial pressure, thus supporting the hypothesis that exsolution of hematite from a single hercynite spinel is an oxygen diffusion-controlled transformation.

PLATE 58 - Heat-treated dosed deposit ($915^{o}C$, oxygen) : Fine exsolution of hematite (white) from spinel (light grey) in the bulk of the sample.

(x250)

PLATE 59 - Heat-treated dosed deposit ($1025^{o}C$, oxygen) : Coarser exsolution in the bulk at high temperature.

(x250)

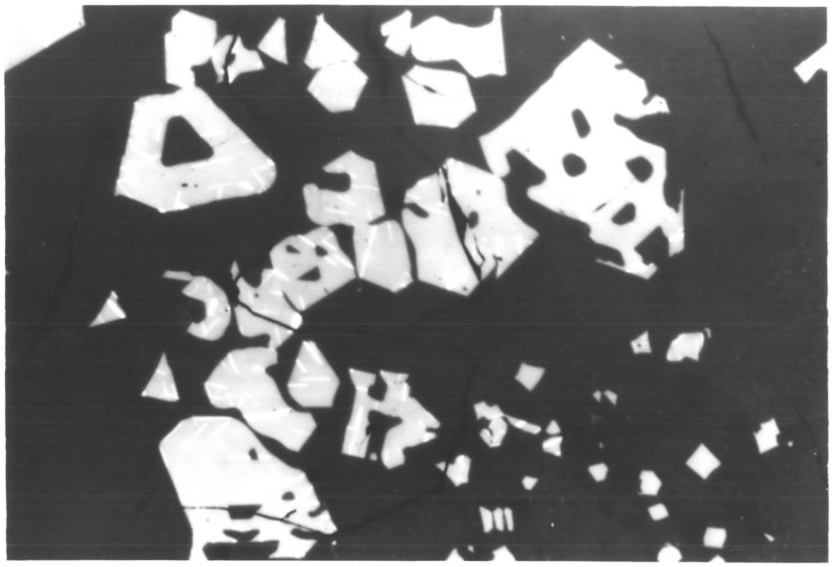

PLATE 58

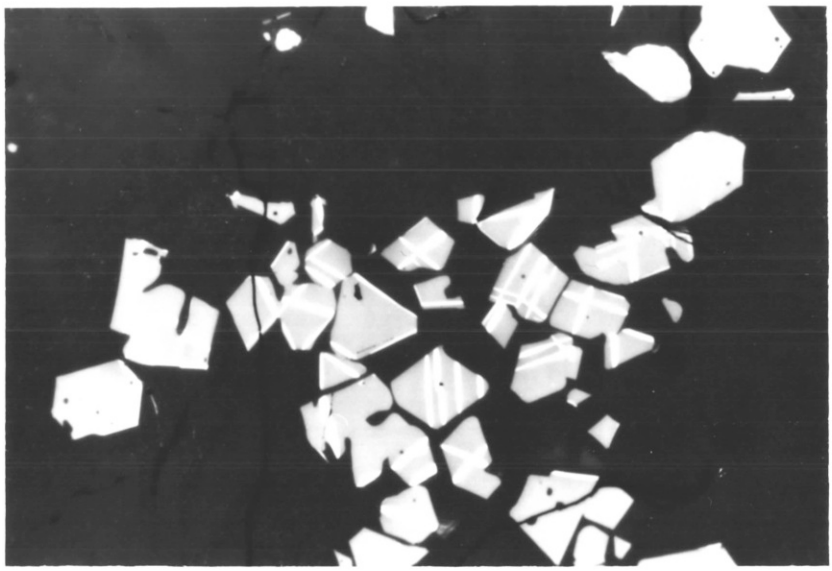

PLATE 59

TABLE 23 - XRD analyses of heat-treated samples from a COC-dosed slag from Station 6

	Intensity of strongest peak in standard pattern (counts S^{-1})			
	Spinel (2.48Å)	Hematite (2.69Å)	Anorthite (3.20Å)	Hem / spinel
Original slag	775	0	715	0
Heat-treated slag				
Argon	885	50	800	0.06
Air	905	115	865	0.13
Oxygen	685	115	890	0.17

All samples heated at 1020 ± 10°C for 5 hours.

CHAPTER 5

Discussion

5.1 Properties of glasses and partially crystalline materials

5.1.1 Crystal growth rates

In considering crystal growth from a melt that is pure with respect to the growing phase, the classical Turnbull and Cohen[42] reaction rate approach introduces two major factors which determine the temperature dependence of growth rate - undercooling and viscosity (see Figure 2). Although the glasses used in the present study are not "pure" in this sense, it is clear that the same basic principles will apply. For any glass the temperature and magnitude of the growth rate maximum will depend on the variation of viscosity with temperature, and hence on composition and crystalline species present. It can further be stated that "impurity" species not required for crystallisation will tend to concentrate in the region immediately in front of the growth front and will directly influence growth rates by affecting the viscosity of this region and hence mass transport across it.

The effect of composition on growth is shown in the crystallisation of both the high and low lime glass series used in the present study. The summary of growth rate results in Table 9 shows that in each series the maximum growth rate observed generally increased as the viscosity at the temperature of maximum rate decreased. For each series the temperature of maximum rate was remarkably constant; 1220-1240°C for the high lime glasses, and 1270-1290°C for the low lime glasses. The results agree well with the work of Kalmanovitch.[114]

From Table 9, two exceptions to the general trends are immediately obvious. In the case of the high lime iron-containing glass, HL/F5, a substantial amount of iron oxide solid solution was found. Thus, not only was the crystallising phase different from the other HL glasses, but the impurity rejection process was fundamentally altered. Direct comparison with the other HL compositions is thus invalidated. In the case of the soda-containing low lime glass, LL/N, irregularity is caused by a flaw in the Urbain method for calculating the viscosity. In determining the effect of the modifiers the Urbain formula assumes that the effect of 1mol% of Na_2O is equivalent to that of 1mol% of K_2O.[70] Thus, at any given temperature the viscosities of LL/K2 and LL/N are calculated as exactly the same. Extensive literature exists concerning the viscosity of R_2O - SiO_2 glasses, and detailed studies have shown that the molar effect of Na_2O on viscosity is much greater than that of K_2O,[115] probably due to the smaller ionic size. The effects are only of the same magnitude if additions are considered in terms of R^+ ions per unit volume, rather than mol%, since the former is a direct measure of the number of non-bridging oxygen atoms present per unit volume.

In order to account for the fact that anorthite grows much faster than gehlenite, even though the viscosities of the LL glasses are much higher than those of the HL glasses, a consideration of activation energy is useful.

For the sake of example, take the two base compositions, HL and LL. Arrhenius plots of ln (growth rate) against inverse temperature give the activation energies for growth as 302kJ mol^{-1} and 280kJ mol^{-1}, respectively. Similar plots using the viscosity data calculated by the Urbain method give the activation energies for viscous flow as 190kJ mol^{-1} and 260kJ mol^{-1}, respectively.

Thus, in the case of the LL composition the activation energy for crystal growth is much the same as that for viscous flow. Growth will proceed almost exactly as theory predicts.[108] This can be correlated to the position of the LL composition on the ternary equilibrium phase diagram[116] - it lies very close to the anorthite composition and, hence, the melt is relatively pure with respect to the crystallising phase.

The case of the HL composition is very different. The activation energy for crystal growth is some 50% higher than that for viscous flow. Once again this can be correlated to the phase diagram - the HL composition lies a long way from that of gehlenite. Hence the melt is very 'impure', and diffusion distances are very much longer. This must account for the slower crystal growth rates.

A similar argument can be used to explain why the whole ash compositions crystallising to give anorthite (1 and 2) give lower maximum growth rates than might be expected for the magnitude of the calculated viscosities as compared to the LL series of glasses.

The amount of 'impurity' can be considered by comparing the SiO_2 : CaO ratios for the glasses with that of anorthite. On a molar basis SiO_2 : CaO for anorthite is 2; for composition 1 it is 3.47, and for the LL series of glasses it is 2.35. Thus, the LL glasses are closer to the anorthite composition than glass of composition 1 and so during the crystallisation process Ca^{2+} ions will need to diffuse over shorter distances. Hence, crystal growth will be more rapid.

Similarly composition 3 (molar Al_2O_3 : SiO_2 = 0.3) crystallising to give mullite is well removed from the growing phase (molar Al_2O_3 : SiO_2 = 1.5) on the phase diagram. Growth is some three orders of magnitude slower than for anorthite, although the viscosity is only greater by a factor of two. A simple relationship between the viscosity and crystal growth rate is bound to break down when considering growth

from an "impure" melt.

A further observation pertinent to the microstructure of slag deposits is that for all the compositions studied there was negligible growth below 850°C. Thus, any molten fly-ash particle that is rapidly quenched from almost flame temperature (∿ 1500°C) to tube-wall temperature (∿ 400°C) will remain in a vitreous state. This is consistent with the porous glassy layer observed by Jones et al[50] closest to the tube-side in a large deposit. The only crystalline phase detected in this layer was undissolved quartz. As the thickness of the deposit increased, the surface temperature would have risen, due to the insulating effect of the slag layer beneath, into the temperature region where crystal growth can occur.

5.1.2 Physical and mechanical properties

In this study the effects of composition, porosity, and crystallinity on the physical and mechanical properties of model slag materials have been determined.

5.1.2.1 Thermal conductivity

The thermal conductivity of a glass is governed by the degree of continuity of the network structure. Thus, LL glass, containing a lower proportion of CaO and higher proportions of SiO_2 and Al_2O_3 than HL, would be expected to have a higher conductivity than HL. Experimental work confirmed this to be so. The values obtained agree reasonably well with those predicted by the additive relationships quoted in the literature. For example, using the formula of Ammar et al[117] for the LL glass a thermal conductivity of 1.34 $Wm^{-1}\ K^{-1}$ at 30°C is obtained, while that of Ratcliffe[98] gives 1.13 $Wm^{-1}\ K^{-1}$ at 100°C. The experimental value was 1.34-1.50 $Wm^{-1}\ K^{-1}$ at ∿150°C. Discrepancies are undoubtedly due to the fact that the composition of LL glass lies well away from the commercially important glasses which the quoted authors considered.

Crystallising LL samples lowered the thermal conductivity by ∿20%, while HL samples retained a conductivity similar to the glass. Porosity had a more profound effect on the conductivity of HL glass, reducing it to 50% of the dense value for 20% porosity and to 20% of the dense value for 50% porosity. Experimentally determined values lay approximately halfway between the upper and lower bounds of the Maxwell-Eucken equation. The porosity - conductivity curve was smooth and continuous - there was no critical porosity value above which conductivity became very much lower, as is seen in some composite materials.[100]

5.1.2.2 Mechanical properties

Compressive strength and elastic modulus were found to be greatly affected by both crystallinity and porosity. Composition HL was used for these determinations.

The maximum compressive strength of HL glass, 510 MN m^{-2}, was reduced by the inclusion of porosity. Data fitted the exponential Ryshkewitch formula[101] with the factor n lying between 2 and 4. The crystallisation of porous samples had little effect at 10 vol% crystallinity - the effect of porosity was dominant. However, there was a marked increase in strength at 40 vol% crystallinity - crystalline samples were 50% stronger than the glassy samples of corresponding porosity. The most likely explanation of this increase is that the small crystallites were able to blunt or deflect the advancing crack, so increasing the work of fracture. The range of compressive strengths obtained agrees closely with the values found by Tangsathitkulchai and Austin[96] in their study of the sintering of coal ash.

The elastic modulus of all samples was found to increase with strain. This is a consequence of the change in atomic packing density as the materials were compressed. For sake of comparison the modulus at zero strain has been used.

Modulus values obtained by the test procedure adopted are undoubtedly specimen size dependent. Standard Pyrex samples slightly smaller in diameter than the dense HL glass samples had lower moduli - 2.45 GNm^{-2} against 2.67 GNm^{-2} - in spite of the fact that the Pyrex structure is substantially less modified. Pyrex would be expected to be stiffer than HL glass. It is also apparent that the modulus values obtained are very much lower than quoted Young's moduli figures - for Pyrex, E = 68 GNm^{-2}.[89] The modulus measured in the present study must be a complicated function of the elastic constants of the material tested. However, if conditions, especially specimen size, are not varied this modulus can still be used to assess the microstructural dependence of elastic properties in general.

The inclusion of porosity into glassy samples reduced the modulus to a somewhat greater extent than predicted by Mackenzie.[102] Slight crystallinity in the porous samples did not affect the modulus noticeably again porosity must be dominant. However 40 vol% crystallinity increased modulus values by ~25%. This is an additive phenomena whereby the addition of relatively stiff particles into a matrix will increase the modulus of the composite.

5.1.2.3 Thermal expansion

The thermal expansion of a glass is also generally determined by the continuity of the network structure - increased continuity leads to decreased expansivity, since a more continuous structure requires more energy to expand it. Measured glass expansion coefficients over the range 100-700°C were seen to increase with decreasing molar acid : base ratio, the latter being taken as a simple measure of network continuity. The absolute values obtained were somewhat higher than those predicted by available additive formulae. For example, using the formula proposed by English and Turner[118] for the LL glass gives an expansivity of

$3.9 \times 10^{-6}\ ^{o}C^{-1}$ over the range 25 - 90°C, while that of Lakatos et al[119] gives $2.4 \times 10^{-6}\ ^{o}C^{-1}$ over the range 20-300°C. The value measured in this study was $4.8 \times 10^{-6}\ ^{o}C^{-1}$. Again the unconventional composition of LL may be responsible for the difference. For example, in considering the addition of lime to a silicate, it is likely that changing from 0 to 5 wt% CaO will have a larger effect on expansivity than changing from 15 to 20 wt% CaO. Simple additive formula seldom take such changes into account.

The glass transition and softening temperatures, Tg and Mg, are related to the viscosity and hence composition, but generally in an opposite way to expansivity. Higher network continuity leads to high characteristic temperatures. In this study, Tg and Mg showed little correlation to the simple molar acid : base ratio, surely reflecting the more complicated compositional dependence of viscosity. Absolute values obtained were in good agreement with those predicted by Lakatos et al.[119] For example, for composition LL, Tg is calculated to be 870°C, and when measured was found to be 845°C, while Mg is calculated as 915°C and measured as 880°C. Again the 'saturation' effect of large amounts of modifier most likely accounts for the difference.

Porosity had no effect on the expansion behaviour of HL glass over the range of porosity examined, and clearly did not interfere with the expansion of the solid phase.

Crystallisation increased thermal expansivity, from $7.4 \times 10^{-6}\ ^{o}C^{-1}$ to $8.3 \times 10^{-6}\ ^{o}C^{-1}$ in the case of HL, and from $4.8 \times 10^{-6}\ ^{o}C^{-1}$ to $6.4 \times 10^{-6}\ ^{o}C^{-1}$ for LL. This effect is due to adding a higher expansivity material, i.e. the crystalline phase, to the glass.

5.1.3 Thermal shock parameters

It is clear from the preceding section that the microstructure determines the physical and mechanical properties of slag-like materials. In order to assess the overall effect on thermal shock behaviour, the HL composition data can be used, since this is most complete.

In their quantitative microstructural study of a large slag deposit, Jones et al[50] found that slag microstructure varied across the deposit, and identified four regions within the slag layer. These four regions can be taken as describing typical deposits likely to be found as wall deposits in boilers.

For each region, it is possible to assign an approximate value of the crystallinity and porosity. For this argument these values have been somewhat idealised in order to allow better estimation of the physical and mechanical properties of each region. For example the only crystallinity values considered were 0, 10 and 40 vol% since these correspond with the values investigated in the present study.

Table 24 shows the properties of each of the regions. All the properties are expressed as a microstructually dependent factor multiplied by the value of the property for dense HL glass. Further, the values of the thermal shock parameters R and R' are calculated, again in comparison to the dense HL glass, i.e. R/R_o and R'/R'_o, where the subscript o refers to the dense glass. The absolute value of R_o has little meaning because of the use of compressive strength and a size-dependent modulus, rather than tensile strength and Young's modulus. The ratios, however, compare the effect of microstructural changes on the ability of a slag to withstand thermal shock.

Reducing R and R' will reduce the severity of shock which can be withstood without damage. Thus, from Table 24, it can be seen that the inside and outside regions (1 and 4) of the slag are most susceptible to thermal shock fracture, while the central regions (2 and 3) are less so.

TABLE 24 - Relative properties and thermal shock parameters of four characteristic regions in slag deposits of HL composition

Region*	% Crystallinity*	% Porosity*	Modulus	Strength	Expansivity	Conductivity	$\frac{R}{R_o}$	$\frac{R'}{R'_o}$
1	0	30	$.58M_o$	$.4\sigma_o$	α_o	$.39k_o$	.69	.27
2	10	5	$.79M_o$	$.9\sigma_o$	α_o	$.85k_o$	1.14	.97
3	40	10	$.88M_o$	$1.2\sigma_o$	$1.12\alpha_o$	$.67k_o$	1.22	.82
4	10	30	$.58M_o$	$.4\sigma_o$	α_o	$.39k_o$	.69	.27

Subscript o refers to dense glass property value

*Note - The slag regions chosen are those identified by Jones et al[50]. Region 1 is closest to the tube, while Region 4 forms the fire-side of the deposit. Section 2.4.2. gives a detailed explanation of how these regions arise.

This is a direct result of high porosity and low crystallinity. It is this combination of properties which is desirable in a slag if it is to be easily removed.

Further, in considering the overall action of a sootblower jet, the mechanical scouring action of the jet cannot be ignored. The fracture strength of the deposit is therefore similarly important, and again the inner and outer regions are most susceptible to removal.

In extending these arguments to other glass compositions, the effect of porosity can be taken as general, with the same factors applying to any slag. Similarly the effects of crystallinity on mechanical properties are likely to be common. However, it is apparent by simply comparing HL and LL that the changes in thermal conductivity and expansivity caused by crystallisation need to be separately assessed for each composition. Comparison of similar microstructures of different compositions will further require the determination of the magnitude of the dense glass properties for each composition.

5.2 The thermal decomposition of iron sulphides

5.2.1 Decomposition of pyrite in a tube furnace

The present study has shown that the decomposition of pyrite in pellet form yields pyrrhotite, magnetite and hematite. The relative proportion of each phase is dependent on both the temperature and atmosphere.

In general terms it can be stated that pyrite is almost completely absent above 700°C under the conditions of the experiments : 15 minutes at temperature in a flowing gas atmosphere. Between 500°C and 1000°C the major products are pyrrhotite and hematite, the former dominating in an atmosphere of low oxygen partial pressure, the latter with high oxygen partial pressure. Above 1000°C, the two oxides dominate, the formation of magnetite being favoured by a low oxygen partial pressure.

The observation that flow occurs above 1000°C strongly suggests that pyrite initially decomposes to give pyrrhotite, which is at least partially molten at such temperatures, and that the oxides detected are the product of a subsequent oxidation. At temperatures less than 1000°C the exact reaction path is unclear.

5.2.2 Decomposition of pyrite and pyrrhotite in a drop-tube furnace

Drop-tube experiments were carried out in an atmosphere of 2% oxygen in nitrogen using both finely ground pyrite and pyrrhotite as starting materials. The experimental results were identical for both starting materials; this is taken to indicate that the decomposition of pyrite to pyrrhotite occurs very rapidly in the temperature range used in the top furnace (950°C to 1350°C).

Figure 24 shows the equilibrium phase diagram for the Fe-S system in the region of interest.[83] It shows that no liquids form below 988°C irrespective of the Fe:S ratio. This explains the lack of any evidence of melting having taken place in the pyrite residue in the experiments with the top furnace at 950°C. However at 1000°C or above a liquid phase is formed over a wide range of composition : hence the spherical nature of the iron-rich particles, and their adherence to the steel substrate. The adhering nature of the deposit implies that the particles impacted the substrate as pyrrhotite with the majority of oxidation occurring subsequently in situ.

When the top furnace was at 1100°C or above, spheres still formed but there was little or no tendency for them to adhere; magnetite was the major phase detected. From the pyrite decomposition experiments, it is clear that in this case oxidation must have occurred rapidly in the top furnace, since little or no magnetite forms at the temperatures at which the substrate was held (700-800°C). The maximum temperature at which the pyrrhotite can survive will be very sensitive to atmosphere.

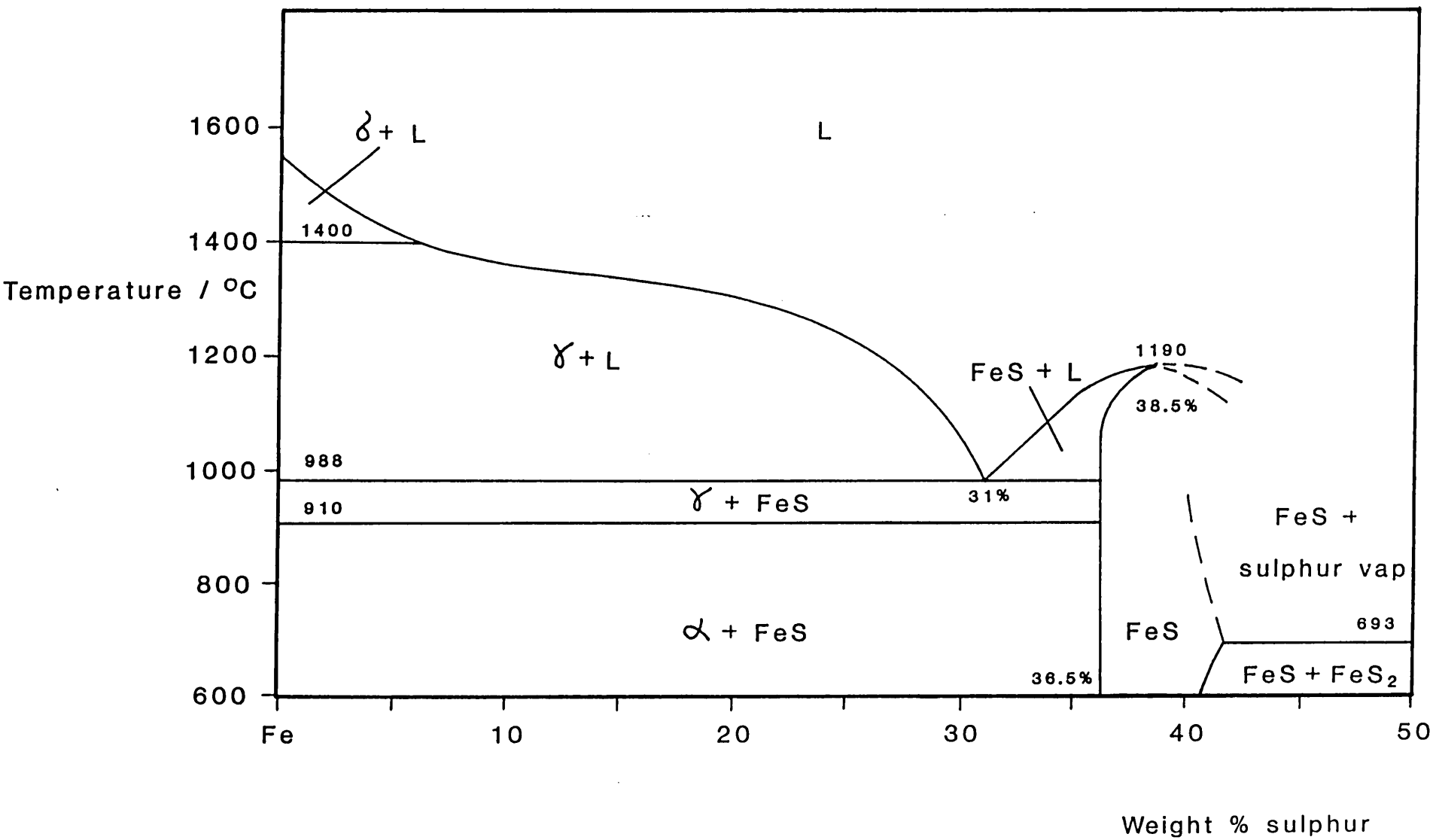

FIGURE 24 - Fe-S phase diagram (83)

It is quite conceivable that this temperature might be greater than 1100°C in a fuel-rich environment.

Under the conditions in which the sulphide residues were found to adhere, lignitic boiler fly-ash showed no tendency to do so. This is because the viscosity of aluminosilicate material at 1000-1100°C is so high that in effect the ash is solid. Thus, providing that the conditions are correct, there exists a mechanism by which iron-rich particles will adhere to a surface while aluminosilicate material will not. The full implications and consequences of this mechanism will be discussed in the following section.

5.3 The microstructural examination of boiler deposits

5.3.1 Deposits from the burner and quarl regions of p.f. boilers

The examination of deposits from Stations 1 and 2 has shown there to be three distinct types of build-up in the burner and quarl regions, varying in both chemical composition and microstructure.

5.3.1.1 Deposit Type 1

The first type of deposit was found as the burner 'eyebrows' and on the quarl surfaces close to these features. The chemical compositions of these deposits were found to be close to those of the parent coal ashes. Microstructures and crystalline phases observed were consistent with the generally accepted model of slag formation - ash particles having been taken up to flame temperature were deposited onto the quarl surfaces. Viscous flow sintering consolidated the spheres to give a relatively dense deposit. Recrystallisation produced phases predicted by the relevant equilibrium phase diagrams, i.e. anorthite, with lesser amounts of mullite, cristobalite and hercynite. Residual quartz and iron oxide particles were retained where time, temperature and atmosphere did not allow complete dissolution.

In the case of the extreme fire-side of several deposits a thin, almost entirely glassy region was observed. This results from molten slag being rapidly quenched when the burner was taken off-load, hence allowing little or no crystallisation to occur.

At Station 2 slagging was seen to occur also on the tube-wall. The slag examined was very similar to that on the refractory surfaces.

5.3.1.2 Deposit Type 2

The second type of deposit was found on the quarl surfaces away from the mouth of the burner, i.e. in cooler regions. Again these deposits had chemical compositions similar to the parent coal ashes, but had characteristic 'coal-like' structures which were highly porous. The mineralogy of these deposits was similar to Type 1, and directly implies that molten fly-ash, having been through the flame, was deposited, and gave the predicted recrystallisation products.

5.3.1.3 Mechanism of formation of deposit Types 1 and 2, and preventative measures

In order to account for the formation of these types of deposits it is necessary to consider the aerodynamic flow of gases and ash in the burner region. Figure 25 shows the recirculation zones which occur in the burner region.[120] These zones have the effect of stabilising the flame, i.e. ensuring that ignition and mixing are effective. It can be seen that material from the flame may be recirculated onto the quarl surfaces, and this would explain the observed build-up. The high gas velocities in this region mean that recirculation streams must contain the whole ash, with no mineral segregation by aerodynamic classification. Hence, deposits have chemical compositions close to the parent coal ash.

FIGURE 25 – Recirculation zones in the burner region

P.A. – Primary air and coal

S.A. – Secondary air

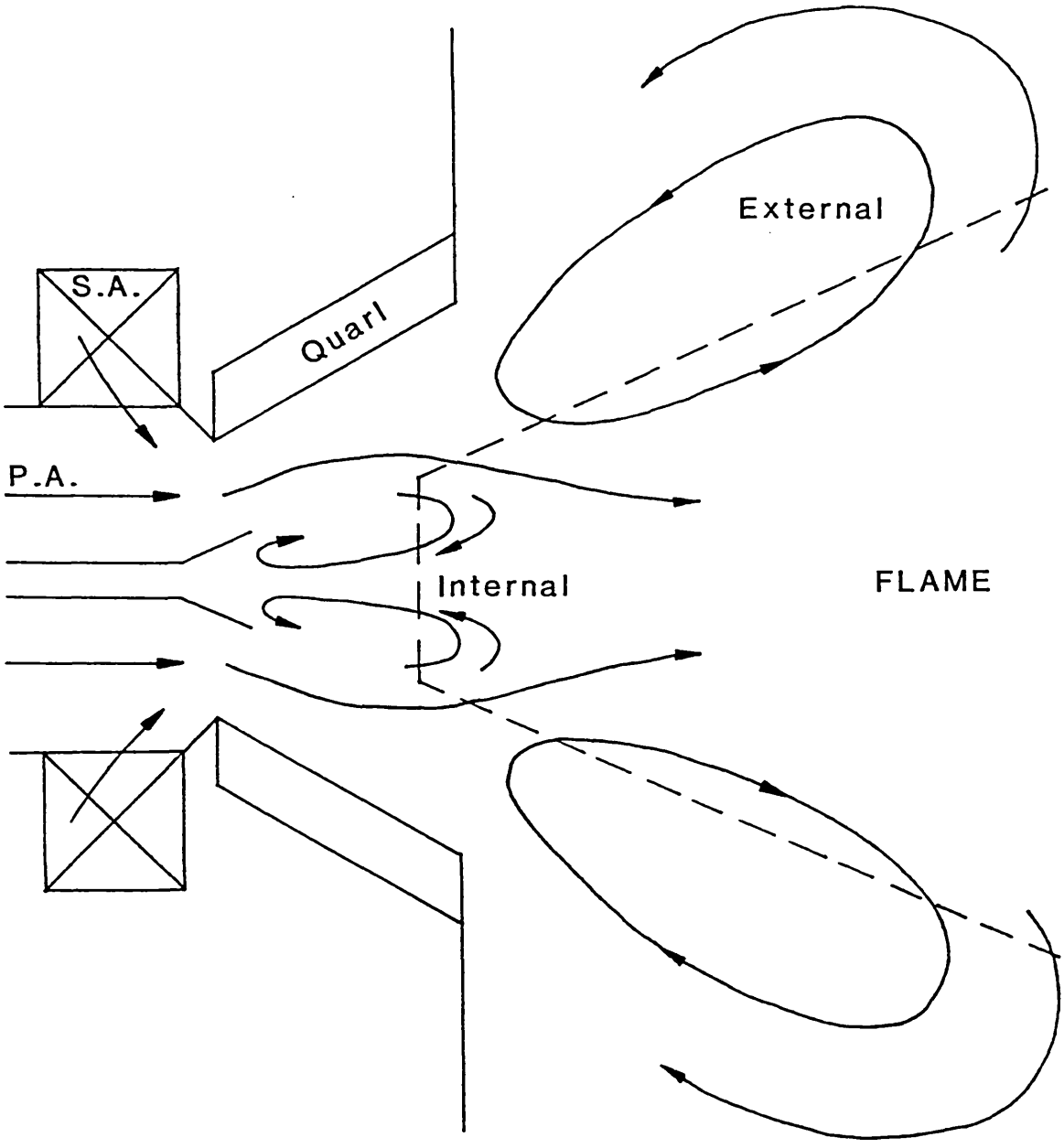

The quarl refractory is normally an aluminosilicate with 60% Al_2O_3, which is used as large prefabricated sections and as a mouldable refractory. Computer simulation shows that using this refractory for the quarl means that surface temperatures at the tip of the quarl closest to the flame may reach 1400°C.[121] Such temperatures are certainly much higher than the surrounding tube-wall surfaces. This explains the marked preference for deposition to initiate on the quarl surface and generally extend into the boiler volume without adhering to the tube-walls.

The differences in the type of microstructure observed along the quarl surfaces are clearly a function of the temperature and atmosphere on those surfaces. Temperatures are highest closest to the boiler volume and sintering is well advanced. However, further back towards the secondary air inlets, the temperatures are lower, and the atmosphere progressively more oxidising as earlier stages of combustion are encountered. Thus, small fly-ash spheres at the surface of a deposit are quickly incorporated into that surface by virtue of their highly curved surfaces. However, the bulk structures having less curved surfaces are much slower to sinter. Quarl surface temperatures have been measured as low as 360°C.[120] In addition the open surfaces are subject to oxidation, the primary effect of which is to reduce the fluxing effect of the iron present, so retarding the sintering process even further.

The causes and mechanism of the deposition on the refractory surfaces are, therefore, quite clear. High surface temperatures result in hot-spots where recirculating molten fly-ash particles can easily adhere.

In order to prevent such deposits forming, extensive trials were conducted at Station 1 involving three major design changes. Firstly the refractory material was changed - the low thermal conductivity of a 60% Al_2O_3 material ($K = 0.2\ Wm^{-1}\ K^{-1}$) was replaced by a higher conductivity SiC ($K = 15\ Wm^{-1}\ K^{-1}$) in an attempt to reduce surface temperatures.

Computer simulation indicated that such a change would reduce the maximum quarl temperature from 1400°C to 1100°C.[121] Secondly, the area of refractory surface on the furnace wall was reduced to a minimum by positioning the fire-side of the refractory behind the first tube on the wall. This had the effect of substantially reducing the area available for deposit build-up. Thirdly, the angle of the quarls was changed so that as far as possible the burner volume was filled with relatively cool gases and coal just coming into the boiler rather than hot gases and molten ash recirculating from the flame.

Preliminary trials were very successful and have resulted in large scale refit alterations to the quarls at Station 1.[122]

5.3.1.4 Deposit Type 3

The third type of deposit found in the burner region contained large amounts of iron oxide. At Station 1, such deposits were found on the venturi throat and the reverse-side of the impeller. At Station 2 they were found on the core-air swirlers.

The throat deposits and the impeller and swirler deposits closest to the metal surfaces were similar in chemical composition and microstructure. Deposits contained between 60 and 90wt% Fe_2O_3 mostly in the form of ill-defined porous hematite. The shape of the hematite implies that molten iron-rich particles impacted onto the metal surface, deforming as they did so. In some cases, high sulphur levels were associated with these structures. In particular, the swirler deposits from Station 2 contained sulphur reporting as up to ∿42wt% SO_3, and had pyrrhotite as the major crystalline phase.

The fire-side of the impeller deposit from Station 1 showed a very different microstructure. Well-defined growth of hematite crystals in a glassy silicate phase was observed. Detailed EPMA showed there to be

an increase of aluminosilicate material on the fire-side, with a corresponding decrease in iron content. Station 2 swirler deposits showed similar changes - in one case the composition of the fire-side of the deposit was very similar to that of the parent coal ash.

5.3.1.5 Mechanism of formation of deposit Type 3

From a consideration of Figure 25 and the positions from which deposits of this type were collected, it is apparent that ash from the inner recirculation zone is responsible for the formation of these deposits. In order to produce such a highly iron-enriched structure, a process of mineral segregation must have occurred.

Borio and Marciso[80] have stated that segregation within the boiler volume can occur as a result of the relatively high density of iron sulphides. When molten, such sulphides are less prone to follow normal gas paths due to their lower aerodynamic drag. However, within the flow patterns of the inner recirculation zone, such action would tend to deplete the stream of iron-rich phases rather than enrich it.

It has to be assumed that the ash entrained in the recirculation zone is representative of the parent coal, and that gas velocities are such as to carry all mineral matter with the stream. The iron-enrichment of deposits of Type 3 must therefore be the result of the deposition process.

It is important at this stage to consider the conditions within the inner recirculation zone. The atmosphere within the zone is likely to be reducing, as most of the available oxygen is used in the ignition process. At the very least it is possible to state that there will be fuel-rich regions within the recirculation zone. Temperatures have been directly measured, and were found to be in the range 600°C to 1200°C.[120]

The present study of the decomposition and oxidation of iron sulphides has shown that under such conditions pyrite will readily decompose with pyrrhotite as the major product, and that this product will be molten above ∿1000°C. In addition, under such conditions aluminosilicate material is effectively solid due to its very high viscosity.

In considering the basic mechanism of deposition, it is clear that an ash particle impacting a deposit will only adhere to that deposit if either the deposit is 'tacky,' the particle itself is 'tacky', or if both are so. A solid particle impinging on a solid surface will just rebound back into the gas stream. Therefore, enrichment of a deposit in a certain chemical constituent will occur if ash particles containing that constituent are able to adhere, while the majority of others are not. This is most certainly the case within the inner recirculation zone.

In this zone, the pyrrhotite which results from the decomposition of discrete pyrite particles will be molten, and able to adhere. Once deposited it will freeze almost instantaneously, so that once again a solid surface is presented to the ash stream. Figure 26 summarises the mechanism proposed. In situ oxidation[82] can then occur over a period of time to give the hematite found in the mineralogical analyses. Impeller temperatures, measured at between 400°C and 700°C,[120] are consistent with hematite formation. The low temperature and low oxygen partial pressure account for the observed presence of residual sulphur in these deposits, with conditions which are likely to promote only slow oxidation.

A major feature of the microstructure of these deposits is the porous nature of the observed hematite as spheres typically having a radius of 50μm. The oxidised form consists of a dense skin ∿10μm thick containing a porous central mass. By calculating the volume change associated with the oxidation of pyrrhotite to hematite, it can be shown that the porosity

FIGURE 26 - Mechanism for the preferential deposition of pyrrhotite

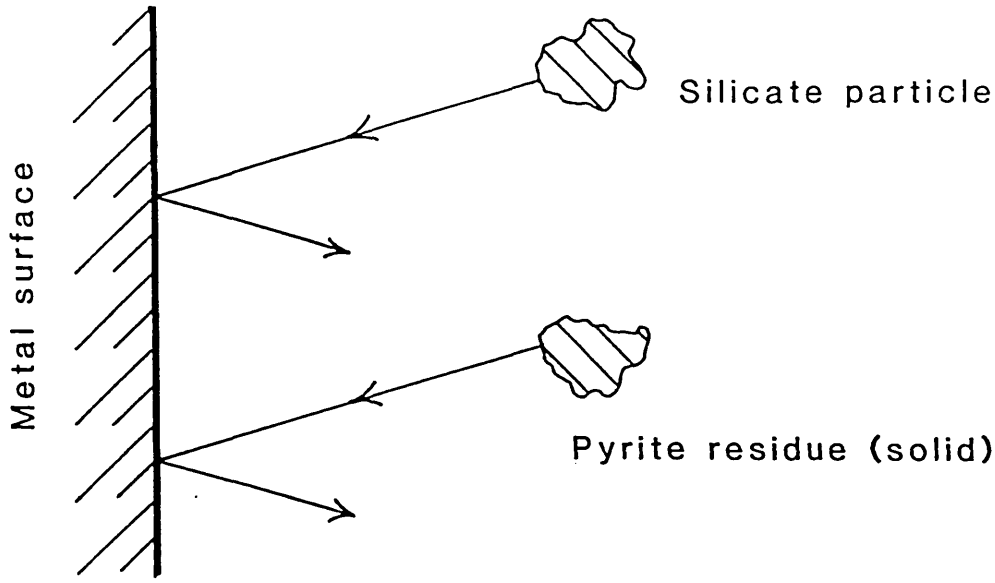

FIGURE 26a - At temperatures below 1000°C both silicate particles and pyrite residues rebound from a solid surface

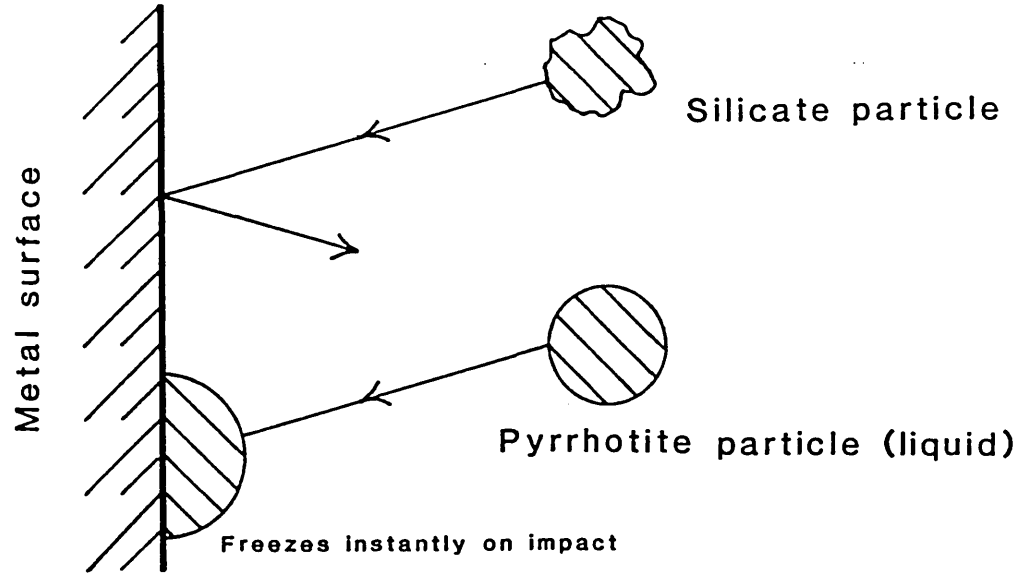

FIGURE 26b - Above 1000°C silicate particles remain effectively solid and rebound, while pyrite residues in the form of pyrrhotite are molten and can adhere on impact

of the central region should be ∿40%. This is consistent with the observed microstructure. Figure 27 shows the detailed calculation.

The proposed model can be taken further by considering the continued development of a deposit. As the thickness of the deposit increases the surface temperature will rise due to the insulating effect of the material already deposited. Thus, on reaching the surface the molten pyrrhotite may not be instantly frozen, and as a result the surface may remain 'tacky'. Under these conditions it would be possible for aluminosilicate material to adhere. Hence, the model predicts an increase in aluminosilicate content towards the fire-side of such a deposit, as observed in the impeller deposit from Station 1. The microstructure also suggests that a molten phase had endured, from which well-defined hematite crystals grew. Figure 28 summarises the extension of the original model.

In the extreme it would be expected that the deposit surface temperature would change sufficiently to allow the whole ash to adhere. This was seen with one of the swirler deposits from Station 2. The sulphur levels in this deposit were low close to the swirler indicating well advanced oxidation, rising to a maximum at the iron-rich/normal composition boundary. Pyrrhotite in this region had least time to oxidize. Low sulphur levels on the fire-side reflect the relatively small amount of iron in the whole ash.

The fact that such deposits do not occur in every burner tends to suggest that when the burners are operating properly the inner recirculation zone sits some way off of the impeller. It may well be that only operational misjudgements allow the impeller to be impinged upon and deposition to occur.

FIGURE 27 - Calculation of porosity of of iron-rich sphere on oxidation from pyrrhotite to hematite

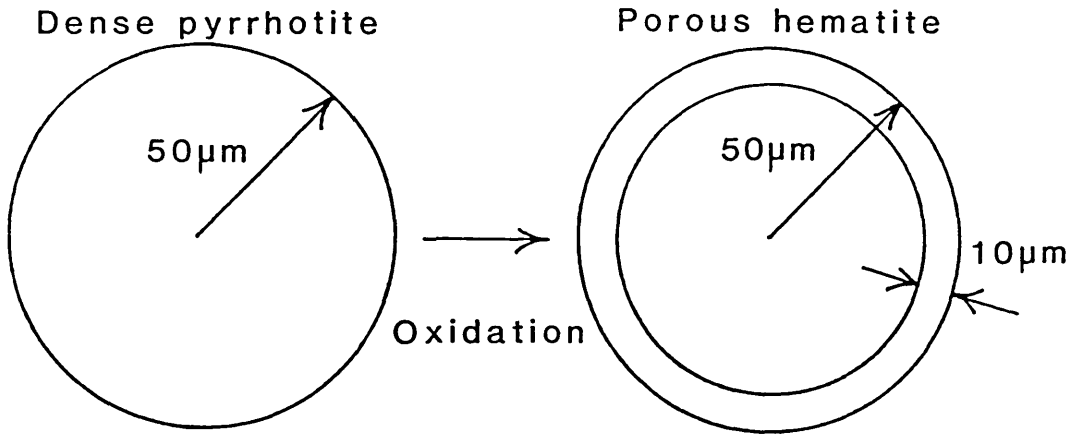

Mass of pyrrhotite = ρV = 4.6V grams

1 mole FeS $\longrightarrow$ ½mole Fe_2O_3

1g FeS $\longrightarrow$ 0.908g Fe_2O_3

$\therefore$ Mass of hematite = 0.908 x 4.6V grams

Volume of hematite = $\frac{0.908 \times 4.6V}{5.24}$ cm^3 = 0.797V cm^3

= $4.17 \times 10^{-7} cm^3$ for r=50μm

For hematite structure,

Volume of skin = (Volume of sphere r=50μm) - (Volume of sphere r=40μm)

= $5.24 \times 10^{-7} - 2.68 \times 10^{-7} cm^3$

= $2.56 \times 10^{-7} cm^3$

Volume of hematite in central porous region

= $4.17 \times 10^{-7} - 2.56 \times 10^{-7} cm^3$ = $1.61 \times 10^{-7} cm^3$

Porosity of central region = $\frac{2.68 - 1.61}{2.68} \times 100\%$ = 39.9%

FIGURE 28 - The inclusion of aluminosilicate material on the fire-side of an iron-rich deposit

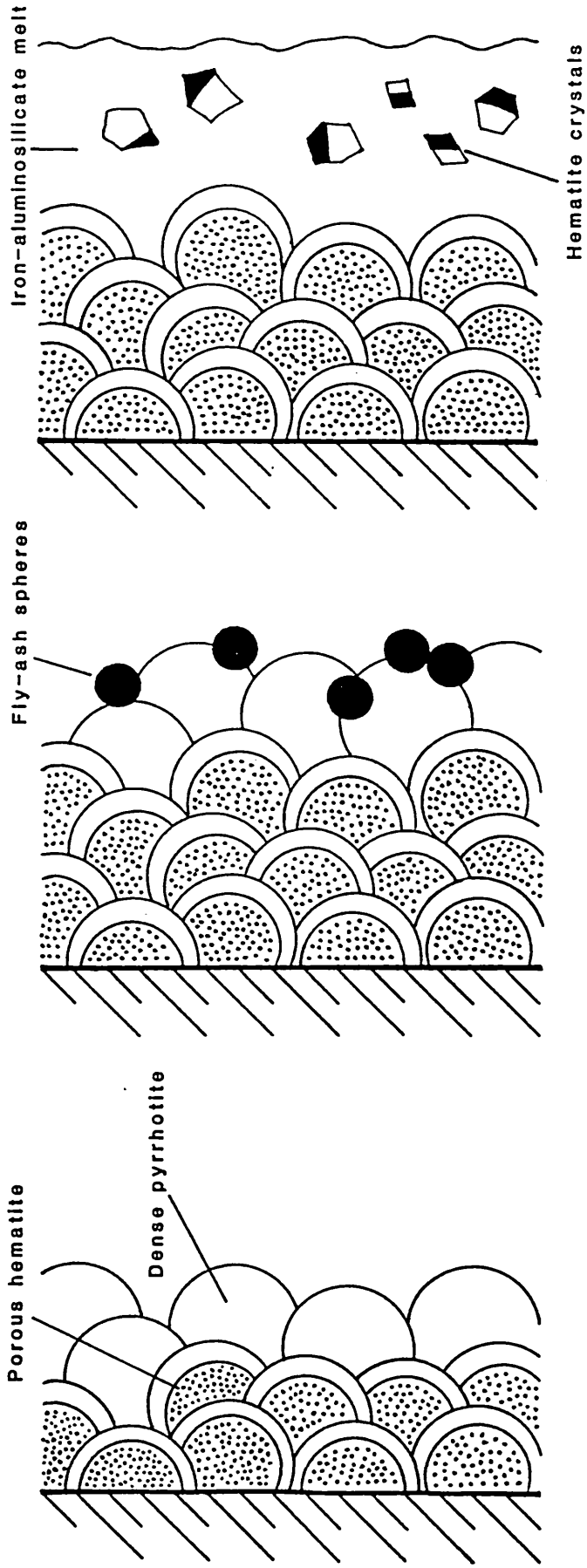

Pyrrhotite deposited and frozen. As deposit grows, surface Aluminosilicate material is

In situ oxidation yields porous temperature rises. Pyrrhotite is fluxed by iron oxide.

hematite not immediately solidified. Low melting point liquid

Surface remains "tacky". is formed. Hematite crystals

Aluminosilicate material is are able to grow from melt.

able to adhere.

5.3.2. Deposits from the tube-walls of p.f. boilers

The large slag deposit taken from the tube-wall near a burner at Station 2 is typical of normal wall deposits found when a boiler is slagging severely. The chemical composition was close to that of the parent coal ash and the crystalline phases were those predicted by equilibrium phase diagrams. Microstructure varied across the thickness of the deposit in accordance with the notion of increased surface temperature with increased deposit build-up. Such features were also found in the ash hopper samples collected from Station 5. When the temperatures within the boiler are close to those of ash fusion the whole ash adheres to surfaces on which it impinges. Such conditions are to be avoided if boiler availability is to remain high.

Further tube-wall deposits from Station 2 and those from Station 3 and 4 were very different to this in nature. It should be made clear that these stations were running under what would generally be termed 'non-slagging' conditions. Deposit build-up was neither rapid nor uniform. However, the detailed structures of the deposits which did form are very interesting.

In each case the initial deposit laid down was similar to the iron-rich deposits described previously. Iron oxide levels were determined as between 50 and 65 wt% Fe_2O_3, with hematite as the major crystalline phase. The microstructure clearly indicated the deposition and subsequent oxidation of pyrrhotite.

In most cases this initial deposit was covered by further material of a much more aluminosilicate-rich nature. Following the arguments put forward in the previous section, this is to be expected as a result of increasing surface temperatures during deposit growth.

In extending the deposition model from one operating in the inner recirculation zone to a general furnace mechanism it has to be assumed that the oxidation of pyrrhotite is slow compared with the time it takes for the particles to reach the wall. The occurrence of minor amounts of magnetite are a consequence of the high temperatures that the particles experience, compared to those in the inner recirculation zone. The high velocity of particles emerging from the flame and the consequently severe particle-wall collisions may well enable particles with thin magnetite skins to adhere so long as the central core remains fluid.

The microstructure of the aluminosilicate-rich regions of deposits from Station 3 and 4 was very different - the former consisted of an almost continuously changing structure in which a large proportion of liquid was present, while the latter showed little tendency to form transition structures.

This is interpreted as a consequence of the continuity of change in viscosity with both temperature and composition in aluminosilicates, there being no sharp transition between the molten and the solid state. Rather, there is a continuous change in viscosity.

At one extreme a deposit may be 'tacky' but still comparitively viscous and hence slow to sinter especially if the atmosphere is oxidising, as is the case for Station 4. Published literature concerning station operation[123] suggests that excess air levels are unusually high. Initial bond formation between particles is weak and bonds are easily broken by the scouring action of ash and gas. Deposit build-up is slow even after transition to normal compositions.

Alternatively the aluminosilicate in the deposit can be much less viscous. In particular a fluid phase will result if temperatures are high and the atmosphere reducing. The deposits from Station 3 are such a case. Being taken from a corner of the boiler, one side of each

deposit is naturally hotter. This explains the occurrence of both sintered and fused material.

In considering the formation of iron-rich deposits in Station 4, an interesting note can be added regarding the burners. Steinmüller burners are designed on very different principles to those of Babcock Power. Turbulence is created aerodynamically by giving the secondary air stream a very large amount of axial swirl. No impeller is generally required. In the first instance it may be seen that the centrifugal forces acting on the coal stream as a result of this increased swirl might account for the mineral segregation observed. It is generally accepted that the high density coal fractions contain high pyrite levels.[124, 125] However such a mechanism would require coal from the central primary stream to penetrate the very fast moving secondary stream. This is considered to be most unlikely.[126]

5.3.3 Deposits from a stoker-fired boiler using copper oxychloride (COC) additive

These deposits were found to be remarkably similar to wall deposits from p.f. boilers. The major crystalline phase present in both the dosed and undosed slags was anorthite. This would be predicted from the chemical composition of the parent coal. Both microstructure and the degree of crystallinity were found to vary across the thickness of the deposits. The deposition, sintering and recrystallisation processes operate exactly as in a p.f. boiler, even though the fly-ash is much coarser.

The major difference between the dosed and undosed samples was in the overall degree of crystallinity, the former being more crystalline than the latter. One particularly striking feature of the microstructure of the dosed samples was the occurrence of iron-rich phases at pore surfaces. This reinforces the generally accepted mechanism of COC action

as one of nucleating iron-rich crystallisation around pores. This crystallisation retards sintering leading to porous friable deposits which are easy to remove.(52)

The exact nature of the iron-rich phases has been clarified by this study. Oxidation of recrystallised hercynite spinel leads to the exsolution of a hematite solid solution, when the solubility limit is exceeded. Thus, two iron-rich phases are often observed. The chemical compositions of the solid solutions detected are consistent with those found naturally.(127)

CHAPTER 6

Conclusions and suggestions for further work

6.1 Conclusions

Detailed microstructural examination of boiler deposits from a number of utilities has shown that a wide variety of structures is formed in boilers burning coal.

Slags with chemical composition close to that of the parent coal ash occur on the tube-wall and refractory surfaces, and have been shown to be the product of deposition, sintering and recrystallisation of the whole fly-ash in both p.f. and stoker-fired boilers. The precise microstructure of the deposits has been shown to be determined by local temperature and atmosphere conditions. Some slags may be formed as a direct consequence of design features, and changes to these features have been seen to result in reduced deposition.

The physical and mechanical properties which determine the thermal shock behaviour of aluminosilicate slags have been found to be markedly affected by the chemical composition and the amount of porosity and crystallinity present. Consideration of thermal shock parameters has shown that slags with a high porosity and low crystallinity are those most likely to be removed by the action of sootblowers.

Iron-rich deposits occur on the impeller and core-air swirler surfaces of the burners in p.f. boilers. Detailed study of the decomposition of iron sulphides has shown that these deposits are the result of the preferential deposition of iron-rich particles from the inner recirculation zone of the flame. Rapid decomposition of discrete pyrite particles to pyrrhotite in an oxygen-lean atmosphere at around 1000-1100^{o}C gives spherical, molten particles. At such temperatures, aluminosilicate material is effectively solid, hence at deposition only

iron sulphide particles adhere. In situ oxidation of pyrrhotite has been shown to yield porous hematite structures.

The increase in surface temperature with deposit thickness has been shown to lead to the inclusion of aluminosilicate material in the deposit as a consequence of the iron sulphide freezing more slowly when it adheres. The fire-side regions of some deposits have been found to have normal ash compositions and microstructures consistent with these. Under "non-slagging" conditions this model has been shown to account for the initiation of deposition of aluminosilicate material on tube-walls.

6.2 Suggestions for further work

When designing a boiler, it is desirable to reduce the physical dimensions of the furnace as far as possible, in order to reduce capital cost. However, in doing so gas temperatures rise and slagging becomes more likely. Definition of the optimum furnace geometry with respect to the coal ash fired is as yet unclear. A detailed study of the physical and microstructural properties of deposits in relation to geometry, at both pilot-scale and full-scale, would aid furnace design considerably.

In addition, knowledge of fouling deposits would be very much extended by detailed microstructural examination. Although not considered in the present study fouling deposits are troublesome in many utilities and a fundamental study of their properties using the sophisticated electron microprobe analysis which is available today would yield valuable information on the mode of formation. This in turn could lead to ways of reducing the problem.

APPENDIX

The design of a boiler is governed by the amount of steam to be produced, the application for which the steam is to be used, and the fuel to be fired. This appendix contains schematic diagrams and basic operational information for the six utilities from which deposits were collected for consideration in the present study.

Keys to diagrams:

Station 1 to 5 - Electricity-generating utilities

1 Final superheaters
2 Platten superheaters
3 Primary superheaters
4 Reheaters
5 Economisers
◄— Burner rows

Station 6 - Process steam utility

1 Coal feed spreader
2 Travelling grate
3 Boiling-tube banks
4 Economisers

STATION 1 — 6 x 660 MW units

Babcock Power Ltd.

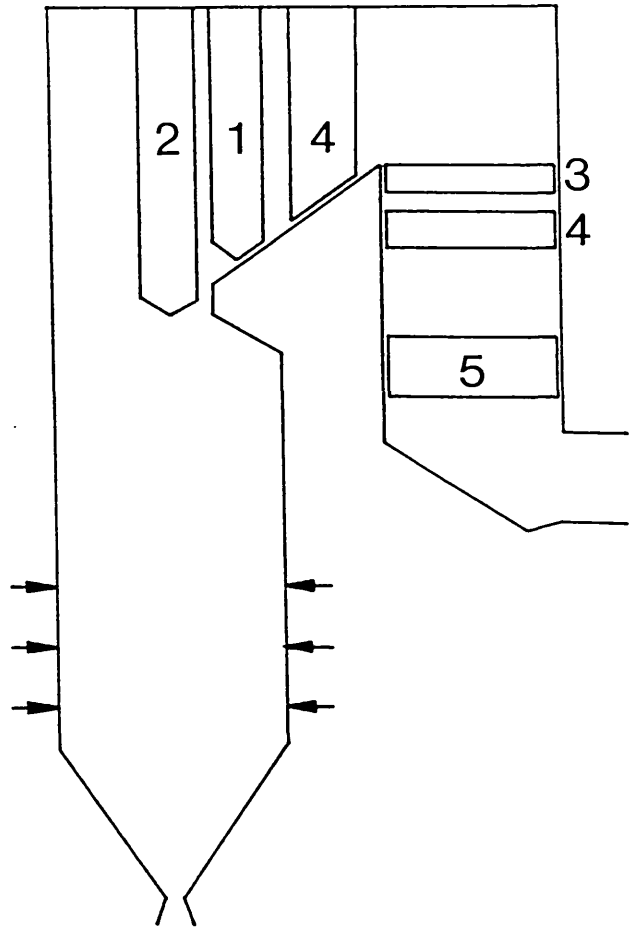

Type of boiler	Membrane wall (vertical tubes) Radiant, reheat, natural circulation
Method of operation	Balanced draught
Superheater outlet pressure	175.6 kg/cm^2
Steam temperature	540^{o}C
Steam flow	508.2 kg/s
Firing equipment	48 circular p.f. burners (3 rows of 8, back and front)
Coal consumption	75.1 kg/s
Design coal GCV	20600 kJ/kg
Pulverising equipment	6 large 'E'-type ball mills.

STATION 2 — 3 x 660 MW units

Babcock Power Ltd.

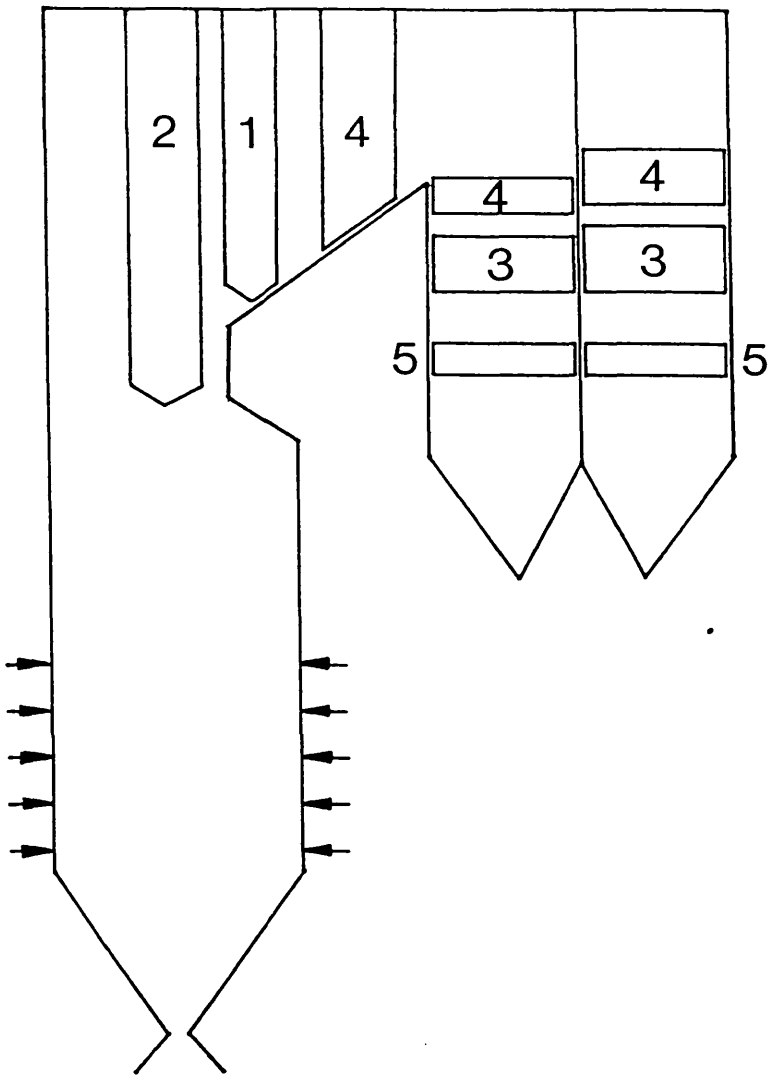

Type of boiler	Membrane wall (vertical tubes) Radiant, reheat, natural circulation
Method of operation	Balanced draught
Superheater outlet pressure	169.8 kg/cm^2
Steam temperature	568^{o}C
Steam flow	563 kg/s
Firing equipment	60 circular p.f. burners (5 rows of 6, back and front)
Coal consumption	70.1 kg/s
Design coal GCV	24400 kJ/kg
Pulverising equipment	10 large 'E'-type ball mills

STATION 3 — 4 x 500 MW units

Babcock Power Ltd.

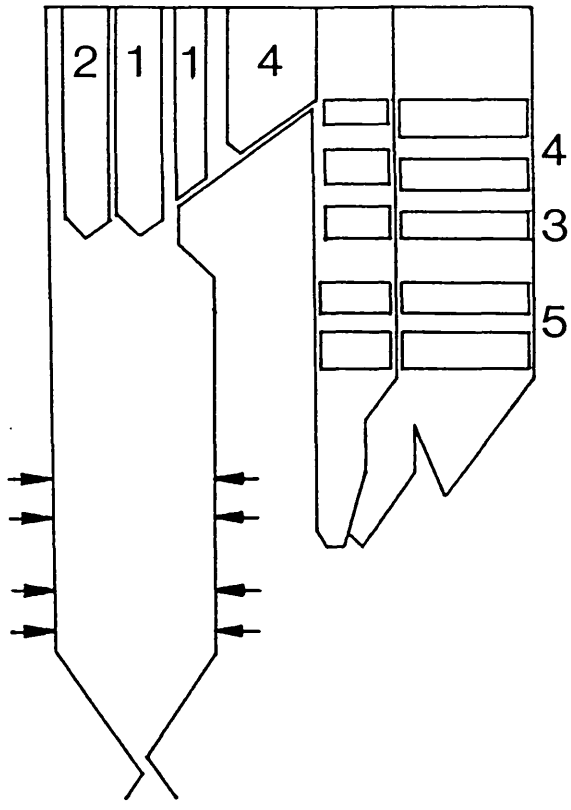

Type of boiler	Membrane wall (vertical tubes) Radiant, reheat natural circulation
Method of operation	Balanced draught
Superheater outlet pressure	169 kg/cm^2
Steam temperature	568°C
Steam flow	433 kg/s
Firing equipment	48 circular p.f. burners (4 rows of 6, back and front)
Coal consumption	58 kg/s
Pulverising equipment	8 large 'E'-type ball mills

STATION 4 — 500 MW units

Steinmüller

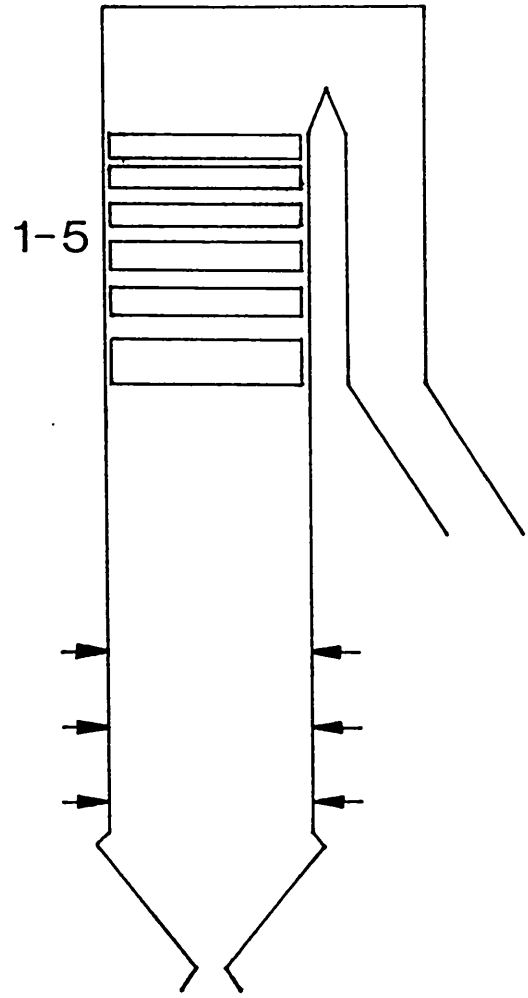

Type of boiler	One-pass, tower Spiral tube arrangement
Steam temperature	515°C
Steam flow	440 kg/s
Firing equipment	36 circular p.f. burners (3 rows of 6, back and front)
Design coal GCV	22200 kJ/kg.

STATION 5 — 2 x 500 MW units

Foster-Wheeler/John Brown Boilers Ltd.

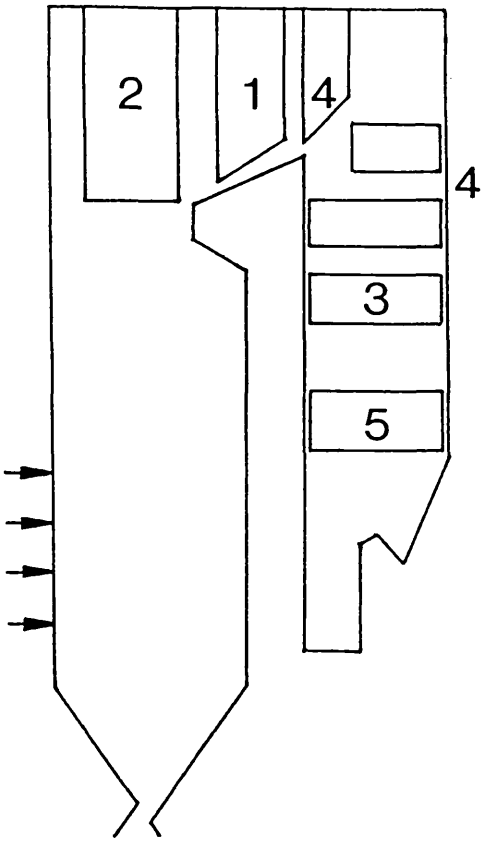

Type of boiler	Membrane wall, radiant
Superheater outlet pressure	172,3 kg/cm^2
Steam temperature	571°C
Steam flow	430 kg/s
Firing equipment	28 circular p.f. burners (3 rows of 8, 1 of 4)
Milling equipment	7 verticle spindle mills

STATION 6 Unit produces process steam for a chemical plant

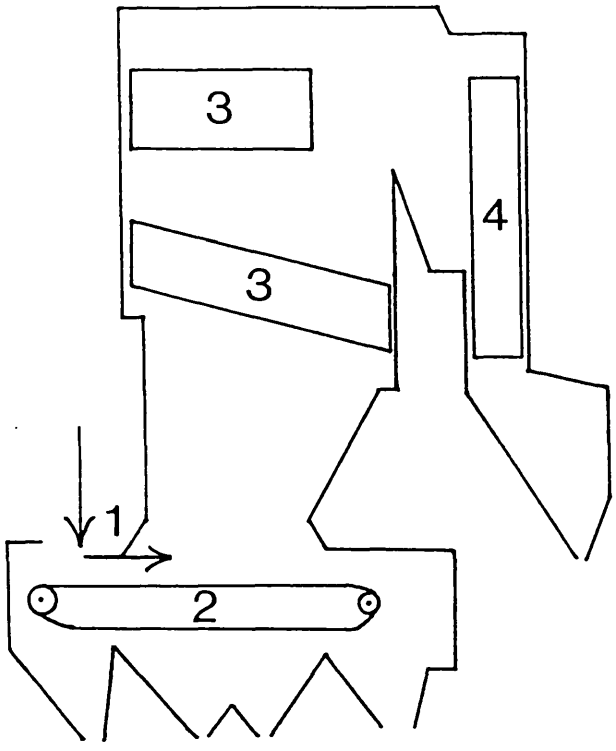

Type of boiler	Mass-burn stoker Travelling grate
Steam outlet pressure	63 kg/cm^2
Steam temperature	450°C
Steam flow	21 kg/s
Coal consumption	2.8 kg/s

Steam production is on a much smaller scale than the electrical utilities. This is reflected in the steam properties.

The boiler walls consist of tubes embedded in 60% Al_2O_3 refractory. The 1.5m closest to the grate consists of prefabricated SiC sections.

REFERENCES

1. Babcock and Wilcox Limited, New York, "Steam - Its generation and use" 38th Edition 1972, various chapters.

2. Babcock Power Limited, London - Product Engineering literature.

3. K. Muraishi, Energy dev. in Japan 5 (1982) 163-206.

4. W. Francis, "Coal - Its formation and composition". Edward Arnold Limited, London 1954.

5. A. Lowe, "Pulverised-coal firing - The effects of mineral matter", Conference held at University of Newcastle, Australia 1979, pW4 20-25.

6. L.J. Edgcombe and A.B. Manning, J. Inst. Fuel 25 (1952) 166-170.

7. R.G. Jenkins and P.L. Walker Jr., "Analytical methods for coal and coal products : Volume II" Ed. C. Karr Jr., Academic Press 1978, pp265-292.

8. British Standard BS 1016, Pt.14, 1963.

9. H.J. Gluskoter, "Ash deposits and corrosion due to impurities in combustion gases". Ed. R.W. Bryers, Hemisphere 1978, p.3-20.

10. R.N. Miller, R.F. Yarzab and P.H. Given, Fuel 58 (1979) 4-10.

11. R.B. Finkelman and H.J. Gluskoter, "Fouling and slagging from combustion gases". Ed. R.W. Bryers, Engineering Foundation, New York 1983, p.299-318.

12. J.D. Watt, "The physical and chemical behaviour of mineral matter in coal under the conditions met in combustion plant : Part I", 1969 B.C.U.R.A. Literature Survey.

13. Babcock Power Ltd., London, private communication.

14. J.D. Watt, "The physical and chemical behaviour of mineral matter in coal under the conditions met in combustion plant : Part II", 1969 B.C.U.R.A. Literature Survey.

15. D.N. Toor, "Thermal analysis of minerals", Abacus Press, 1976.

16. G.W. Brindley, "Progress in ceramic science: Vol. 3", Ed. J.E. Burke, Macmillan, 1963, p1-55.

17. G.W. Brindley and M. Nakahira, J. Am. Ceram. Soc. 42 (1959) 311-324.

18. M.M. Taboadela and V.A. Ferrandis, "D.T.A. investigation of clays", Ed. R.C. Mackenzie, Min. Soc. London 1957, Chapter VI.

19. T.L. Webb and H. Heystek, "D.T.A. investigation of clays", Ed. R.C. Mackenzie, Min. Soc. London 1957, Chapter XIII.

20. G.M. Schwab and J. Philinis, J. Am. Chem. Soc. 69 (1947) 2588-2596.

21. R.W. Bryers, Trans. A.S.M.E. J. Eng. Power 98 (1976) 517-527.

22. E. Raask, J. Inst. Energy 57 (1984) 231-239.

23. J.R. Arthur, D.H. Bangham, R.H. Baulk and G. Whittingham, Nature 166 (1950) 358-359.

24. J.V. O'Gorman and P.L. Walker, Fuel 52 (1973) 71-79.

25. R.S. Mitchell and H.J. Gluskoter, Fuel 55 (1976) 90-96.

26. J.C. Nankervis and R.B. Furlong, Fuel 59 (1980) 425-430.

27. R.C. Flagan and S.K. Friedlander, "Recent developments on aerosol science", Ed. D.T. Shaw, Wiley 1978, Chapter 2.

28. F.S. Sinnatt, J. Soc. Chem. Ind. 1928, 151T-155T.

29. R.J. Lauf, Ceram. Bull. 61 (1982) 487-490.

30. C.D. Stinespring, M. Zulkoski and M.H. Mazza, "Ash deposits and corrosion due to impurities in combustion gases" Ed. R.W. Bryers, Hemisphere 1978, p233-241.

31. E. Raask, J. Inst. Energy 57 (1984) 231-239.

32. R.F. Littlejohn, J. Inst. Fuel 39 (1966) 59-67.

33. F.H. Hubbard, R.J. McGill, R.K. Dhir and M.S. Ellis, Min. Mag., 48 (1984) 251-256.

34. A.R. Ramsden, Fuel 48 (1969) 121-137.

35. E. Raask, J. Inst. Fuel 41 (1968) 339-344.

36. S. Pollmann and W. Albrecht, "Fouling and slagging from combustion gases" Ed. R.W. Bryers, Engineering Foundation, New York 1983, p85-99.

37. E. Raask, "Mechanisms of corrosion by fuel impurities", Ed. H.R. Johnson and D.J. Littler, Butterworth, London 1963, p145-157.

38. E. Raask, J. Thermal Anal. 16 (1979) 91-102.

39. R.E. Conn and L.G. Austin, Fuel 63 (1984) 1664-1670.

40. M.E. Fine, "Phase transformations in condensed systems", McMillan, London 1964, 130pp.

41. K.A. Jackson, D.R. Uhlmann and J.D. Hunt, J. Crystal Growth 1 (1967) 1-36.

42. D. Turnbull and M.H. Cohen, J. Chem. Phys. 29 (1958) 1049-1054.

43. A.J. Milne, J. Soc. Glass Tech. 36 (1952) 275-286T.

44. J.D. Watt, J. Inst. Fuel 42 (1969) 131-134.

45. E.J. DeGuire and S.H. Risbud, J. Mat. Sci. 19 (1984) 1760-1766.

46. N.A.A. Procter and G.H. Taylor, J. Royal Micro. Soc. 85 (1966) 283-290.

47. M. Hupa and B.E. Eriksson, Kemia-Kemi 11 (1979) 607-612.

48. R.R. Fessler, A.J. Skidmore, H.R. Hazard and J.P. Dimmer, Trans. A.S.M.E. J. Eng. Power 102 (1980) 692-697.

49. W.R. Livingston, private communication.

50. M.P. Jones, W.R. Livingston, G. Warren and J. Williamson, Trans. I.M.M. 94 (1985) C30-C34.

51. R.J. Kirkpatrick, Am. Min. 60 (1975) 798-814.

52. W.R. Livingston, A. Sanyal and J. Williamson, "Effectivensss of fuel additives" Institute of Energy, London 1983, Session 2, 21pp.

53. L.T. Kiss, B. Lloyd and E. Raask, J. Inst. Fuel 45 (1972) 213-223.

54. H.E. Crossley, J. Inst. Fuel 25 (1952) 221-225.

55. P.H. Crumley, A.W. Fletcher, and D.S. Wilson, J. Inst. Fuel 28 (1955) 117-120.

56. D.K. Rindt, M.L. Jones and H.H. Schobert, "Fouling and slagging from combustion gases" Ed. R.W. Bryers, Engineering Foundation, New York 1983, p17-35.

57. W.T. Reid, "Chemistry of coal utilisation - second supplementary volume" Ed. M.A. Elliot, Wiley 1981, Chapter 21.

58. British Standard BS 1016, Pt. 15, 1970.

59. E.P. Barrett, "Chemistry of coal utilisation - Vol. I", Ed. E. Lowry, Wiley 1945, Chapter 15.

60. P. Nicholls and W.A. Selvig, U.S. Bur. Mines Bull. 364, 71-79.

61. B.K. Dutta, B. Rai and K.R. Chakravorty, J. Sci. Industr. Res. 19B (1960) 206-212 and 21b (1962) 42-48.

62. E.C. Winegartner and B.T. Rhodes, Trans. A.S.M.E. J. Eng. Power 97 (1975) 395-406.

63. F.E. Huggins, D.A. Kosmack and G.P. Huffmann, Fuel 60 (1981) 577-584.

64. G.P. Huffmann, F.E. Huggins, and G.R. Dunmyre, Fuel 60 (1981) 585-597.

65. W.L. Sage and J.B. McIlroy, Trans. A.S.M.E. J. Eng. Power 82 (1960) 145-155.

66. E.C. Winegartner Ed. "Coal fouling and slagging parameters" A.S.M.E. Special Publication 1974, 34pp.

67. J.T. Shaw, B.C.U.R.A. Monthly Bull. 23 (1959) 169-190.

68. P. Nicholls and W.T. Reid, Trans. A.S.M.E. 56 (1940) 141-153.

69. J.D. Watt and F. Fereday, J. Inst. Fuel 49 (1969) 99-103.

70. G. Urbain, F. Cambier, M. Deletter and M.R. Anseau, Trans. J. Brit. Ceram. Soc. 80 (1981) 139-141.

71. W.T. Reid and P. Cohen, Trans. A.S.M.E. 66 (1944) 83-97.

72. A. Sanyal, D.C. Hough, G.W. Stewart, J.H. Gruniger and K.D. Annen, Eng. Foundation Conf. "Slagging and fouling due to impurities in combustion gases" Colorado, July 1984.

73. I.W. Cumming and A. Sanyal, "Fouling and slagging from combustion gases " Ed. R.W. Bryers, Eng. Foundation, New York, 1983. p.329-341.

74. D.H. Barnhart and P.C. Williams, Trans. A.S.M.E. 78 (1956) 1229-1236.

75. I.W. Cumming, W.I. Joyce and J.H. Kyle, Eng. Foundation Conf. "Slagging and fouling due to impurities in combustion gases" Colorado, July 1984.

76. A. Sanyal and J. Williamson, J. Inst. Energy 54 (1981) 158-162.

77. J.H. Welch, J. Sci. Instum. 31 (1954) 458-462.

78. D.P. Kalmanovitch, A. Sanyal and J. Williamson, J. Inst. Energy 59 (1986) 20-23.

79. H.R. Hazard, R.E. Barratt and J.P. Dimmer, Combustion 51 (1980) 32-37.

80. R.W. Borio and R.R. Narciso, Trans. A.S.M.E. J. Eng. Power 101 (1979) 500-505.

81. R.W. Bryers and T.E. Taylor, Trans. A.S.M.E. J. Eng. Power 98 (1976) 528-539.

82. W.D. Halstead and E. Raask, J. Inst. Fuel 42 (1969) 344-349.

83. J. Chipman, J. Metals Handbook, Am. Soc. Metals, 1948, p1215.

84. M.F. Abbott and L.G. Austin, Fuel 64 (1985) 832-838.

85. M.F. Abbott, W.P. Kinneman, and L.G. Austin, Eng. Foundation Conf. "Slagging and fouling due to impurities in combustion gases" Colorado, July 1984.

86. H. Henke, J.R. Thomas and D.P.H. Hasselman, J. Am. Ceram. Soc. 67 (1984) 393-398.

87. S.W. Freiman, "Glass: Science and technology. Volume 5 : Elasticity and strength in glasses" Ed. D.R. Uhlmann and N.J. Kriedl, Academic Press 1980, p65-68.

88. R.W. Davidge, "Mechanical behaviour of ceramics" Cambridge University Press 1980, Chapter 8.

89. R. Morrell, "Handbook of properties of technical and engineering ceramics - Part I", H.M.S.O. London 1985, various chapters.

90. D.P.H. Hasselman, Bull. Am. Ceram. Soc. 49 (1970) 1033-1037.

91. D.P.H. Hasselman, J. Am. Ceram. Soc. 52 (1969) 600-604.

92. J. Boow and P.R.C. Goard, J. Inst. Fuel 42 (1969) 412-419.

93. M.F.R. Mulcahy, J. Boow, and P.R.C. Goard, J. Inst. Fuel 39 (1966) 385-398.

94. G.D. Fetters, R. Viskanta and F.P. Incropera, A.S.M.E. Paper No. 82-WA/HT-30.

95. D.W. Anderson, R. Viskanta and F.P. Incropera, Eng. Foundation Conf. "Slagging and fouling due to impurities in combustion gases", Colorado, July 1984.

96. M. Tangsathitkulchai and L.G. Austin, Fuel 64 (1985) 86-92.

97. T. Lakatos, L-G. Johansson and B. Simmingsköld, Glastechnik Tidskrift, 28 (1973) 67-73.

98. E.H. Ratcliffe, Glass Tech. 4 (1963) 113-128.

99. M.L. Williams and G.E. Scott, Glass Tech. 11 (1970) 76-79.

100. W.D. Kingery, H.K. Bowen, and D.R. Uhlmann, "Introduction to ceramics" Wiley 1976, various chapters.

101. E. Ryshkewitch, J. Am. Ceram. Soc. 36 (1953) 65-68.

102. J.K. Mackenzie, Proc. Phys. Soc. London B63 (1950) 2-11.

103. P.W. McMillan, "Glass-ceramics" Academic Press, 1979, Chapter 5.

104. S.W. Freiman and L.L. Hench, J. Am. Ceram. Soc. 55 (1972) 86-90.

105. N. Soga and O.L. Anderson, Proc. VII Int. Congress on glass, Brussels 1965, Paper 37.

106. J. Williamson, A.J. Tipple and P.S. Rogers, J. Iron and Steel Inst. 206 (1968) 898-903.

107. J. Francl and W.D. Kingery, J. Am. Ceram. Soc. 37 (1954) 80-84.

108. H.R. Rawson, "Properties and applications of glass" Elsevier 1980 Various chapters.

109. Joint Committee for Powder Diffraction Studies, Card Number 6-0710.

110. Ibid, Card Number 25-412.

111 A.K. Moza and L.G. Austin, Fuel 61 (1982) 161-166.

112. J.H. Lienhard, "A heat transfer textbook", Prentice-Hall Inc. 1981, p.500.

113. R.E. Carter, W.L. Roth and C.A. Julien, J. Am. Ceram. Soc. 42 (1959) 533-536.

114. D.P. Kalmanovitch, Ph.D. thesis "Reactions in coal ash melts" University of London 1983.

115. O.V. Mazurin, M.V. Streltsina, and T.P. Shvaiko-Shvaikovskaya, "Handbook of glass data - Part A" Elsevier 1983.

116. E.M. Levins, C.R. Robbins and H.F. McMurdie, "Phase diagrams for ceramists" Am. Ceram. Soc. 1964, Figure 630.

117. M.M. Ammar, S.A. Gharib, M.H. Halawa, H.A. El-Batal and K. El-Badry, J. Am. Ceram. Soc. 66 (1983) C76-C77.

118. S. English and W.E.S. Turner, J. Am. Ceram. Soc. 12 (1929) 760-764.

119. T. Lakatos, L-G.Johansson and B. Simmingsköld, Glasteknisk Tidskrift 28 (1973) 67-73.

120. J. Smart, Babcock Power Ltd., Private Communication.

121. Computer Simulation by Babcock Power Ltd., Private Communication.

122. J. Wheeler, Babcock Power Ltd., Private Communication.

123. H. Marcus, Energy Developments 3 (1979) 22-28.

124. S.J. Groves, Unpublished data.

125. R.W. Bryers, Trans. A.S.M.E. J. Eng. Power 101 (1979) 506-515.

126. J.L. King, Babcock Power Limited, Private Communication.

127. W.A. Deer, R.A. Howie and J. Zussman, "An Introduction to the rock-forming minerals" Longman 1977.